Performance-based quantification of natural draught wet cooling tower fill fouling

by

Carl Christoff Kohrs

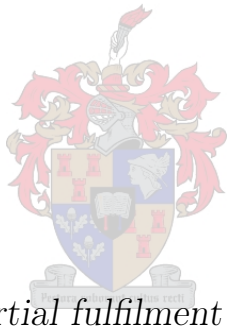

Thesis presented in partial fulfilment of the requirements for the degree of Master of Engineering (Mechanical) in the Faculty of Engineering at Stellenbosch University

Supervisor: Dr. M. Owen

December 2020

Declaration

By submitting this thesis electronically, I declare that the entirety of the work contained therein is my own, original work, that I am the sole author thereof (save to the extent explicitly otherwise stated), that reproduction and publication thereof by Stellenbosch University will not infringe any third party rights and that I have not previously in its entirety or in part submitted it for obtaining any qualification.

Date: 2020/08/30

Abstract

Natural draught wet cooling tower (NDWCT) fill fouling is a widely documented but poorly quantified phenomenon in the power generation industry. Specifically, there are no known methods enabling fair comparison of the fouling behaviour of competing fill designs. Using Monte Carlo methods, it is demonstrated that the thermal (Merkel number) and hydraulic (pressure loss factor) effects of fill fouling may be quantified separately, which introduces generally small errors in NDWCT performance prediction calculations. Fill fouling is subsequently characterised by individual time-dependent thermal and hydraulic fouling factors applied to the fill performance characteristic equations used in NDWCT performance prediction calculations. Fouling factors may be calculated, as in this study, using fill performance measured during long-duration fill testing, or may be estimated using predictive methods. It is demonstrated how the combination of predicted fouling factors and power plant parameters like heat rate correction and fuel cost may be used to perform fill lifecycle cost calculations, enabling fair fill comparisons.

To provide confidence in the measured performance of NDCWT fills, a general method of fill performance measurement uncertainty analysis is developed. Earlier work has calculated the uncertainty of fill performance parameters at a single test operating point in a fill performance test. The current study expands significantly on this method, calculating the uncertainty at all test operating points and propagating these uncertainties first to the uncertainty of the fill thermal and hydraulic performance characteristic equations (known as regression uncertainty) and ultimately to the predicted NDWCT performance uncertainty. It is determined that the inclusion of correlated uncertainties is vital for the regression uncertainty calculations, but that they may be neglected at the NDWCT performance uncertainty calculation stage with relatively small errors. The developed uncertainty analysis method provides rigorous justification for performance-related commercial decisions based on fill performance testing.

The developed fouling factor and uncertainty analysis methods are applied to the weekly performance measurements of four fill samples tested for a period of approximately 40 weeks at a fill fouling test facility located at a coal-fired power station in South Africa. This facility exposes the fill samples to operating conditions closely resembling true fill operation, including the use of actual power plant cooling water. While there are limitations to the testing data due to the relatively short duration and the low-fouling nature of the installed fill samples, as well as testing problems resulting in largely unusable thermal testing data, the use of the developed methods are thoroughly demonstrated.

Opsomming

Natuurlike trek nat koeltoring (NTNKT) pakkingsaangroei is ‘n wydverspreide, maar swak gekwantifiseerde verskynsel in die kragopwekkingsindustrie. Daar is geen bekende metodes om die aangroei van kompeterende pakkings-ontwerpe regverdig te vergelyk nie. Dit word gedemonstreer, deur middel van Monte Carlo-metodes, dat die termiese (Merkel nommer) en hidrouliese (drukverliesfaktor) effekte van pakkingsaangroei apart gekwantifiseer kan word, wat oor die algemeen tot klein foute in die NTNKT verrigtingsvoorspellingsberekeninge lei. Pakkingsaangroei word gevolglik gekarakteriseer as individuele, tydafhanklike termiese en hidrouliese aangroei-faktore wat op die karakteristieke pakkingsverrigtingsvergelykings in die NTNKT verrigtingsvoorspellingsberekeninge toegepas word. Aangroei-faktore word, soos in hierdie studie, vanuit die gemete data van langtermyn pakkingstoetse bereken, of word beraam deur voorspellingsmetodes. Daar word gedemonstreer hoe die kombinasie van voorspelde pakkingsaangroeifaktore en kragstasie-parameters soos die warmtetempo korreksie en brandstofkoste gebruik kan word om die lewenssikluskoste van pakkings te bereken, wat die regverdige vergelyking van pakkingsontwerpe moontlik maak.

Om vertroue in die gemete verrigting van NTNKT pakkings te verbeter, word ‘n algemene metode vir die onsekerheidsanalise van pakkingsverrigtingsmetings ontwikkel. Vantevore is die onsekerheid van ‘n enkele toetspunt gedurende ‘n pakkingsverrigtingstoets bereken. Die huidige studie brei geweldig uit hierop deur die onsekerheid van alle toetspunte te bereken en daarna hierdie onsekerheid te propageer, eerstens na die onsekerheid van die pakkingsverrigtingsvergelykings (bekend as regressie-onsekerheid) en daarna na die verrigtingsonsekerheid van die NTNKT. Daar word bepaal dat dit noodsaaklik is om gekorreleerde onsekerheid in die berekening van die regressie-onsekerheid in te sluit, maar dat dit weggelaat mag word, met relatiewe klein foute, by die NTNKT verrigtingsonsekerheid-vlak. Die ontwikkelde onsekerheidsanalisemetode voorsien streng regverdiging van enige verrigtings-verwante kommersiële besluite wat op pakkingsverrigtingstoetse gebaseer is.

Die ontwikkelde pakkingsaangroeifaktor- en onsekerheidsanalisemetodes word toegepas op die weeklikse verrigtingstoetse van vier pakking-monsters wat oor nagenoeg 40 weke by ‘n pakkingsaangroeitoetsaanleg by ‘n steenkool-kragstasie in Suid-Afrika getoets is. Hierdie aanleg stel pakking-monsters bloot aan toestande naby aan dié in praktyk, insluitend die gebruik van kragstasie verkoelingswater. Alhoewel daar beperkings is op die toetsdata as gevolg van die relatiewe kort toetstydperk en lae neiging tot aangroei van die getoetsde pakkings, asook probleme wat die termiese toetsdata grootliks onbruikbaar maak, word die ontwikkelde metodes ten volle gedemonstreer.

Acknowledgements

To my supervisor, Dr. Michael Owen, thank you for your guidance, support, technical inputs and attention to detail.

To Francois du Preez and Ockert Augustyn, thank you for your valuable inputs in shaping the questions that formed this study. Beyond this, thank you for your foresights that made this study possible.

To Johan, Hanno, Bennie and Lucky and the rest of the team from TF Design, thank you for creating the physical platform to base this study on and going far beyond expectations in assisting me.

To Nicolaas Hallatt, thank you for all the discussions and for bringing certainty to uncertainty.

To Dirk Human, thanks for climbing this mountain with me, for being a friend and a helpful ear whenever I needed it.

My thanks to Regen Waters Laboratory for valuable efficiency and innovation in chemical analysis.

To my parents, Helmut and Maryna, thank you for all your love and support.

My humble thanks to my Heavenly Father, who guided this study beyond human wisdom.

Met liefde opgedra aan Anja en Niel

Contents

List of Figures

List of Tables

Nomenclature

Abbreviations

CDF	Cumulative density function
COC	Cycles of concentration
DC	Direct current
ECDF	Empirical cumulative density function
I/O	Input/output
NDWCT	Natural draught wet cooling tower
PID	Proportional, integral, derivative (control)
PLC	Programmable logic controller
PVC	Polyvinyl chloride
RH	Relative humidity
RTD	Resistance temperature detector
SSC	Steam surface condenser

Symbols

A	Area	$[\mathrm{m}^2]$
a	Coefficient	$[-]$
a_{fi}	Fill surface area per unit volume	$[\mathrm{m}^{-1}]$
b	Systematic uncertainty	$[-]$
C	Coefficient, confidence level, cost	$[-, -, \mathrm{R}]$
C_h	Hourly cost	$[\mathrm{R/hr}]$
C_t	Analysis period cost	$[\mathrm{R}]$
CV	Calorific value	$[\mathrm{kJ/kg}]$
c	Concentration	$[-]$
c_p	Specific heat capacity at constant pressure	$[\mathrm{kJ/kgK}]$
D	Diffusion coefficient	$[\mathrm{m}^2/\mathrm{s}]$
d	Diameter	$[\mathrm{m}]$
F	Function	$[-]$
f_k	Hydraulic fouling factor	$[-]$
f_m	Thermal fouling factor	$[-]$
f_L	Load factor	$[-]$

G	Mass flux	$[\mathrm{kg/m^2s}]$
g	Gravitation acceleration	$[\mathrm{m/s^2}]$
H	Height	$[\mathrm{m}]$
HR	Heat rate	$[\mathrm{kJ/kWh}]$
h	Heat transfer coefficient	$[\mathrm{W/m^2K}]$
h_d	Mass transfer coefficient	$[\mathrm{kg/m^2s}]$
i	Enthalpy	$[\mathrm{kJ/kg}]$
G	Mass flux	$[\mathrm{kg/m^2s}]$
K	Pressure loss factor	$[-]$
K_G	Crystal growth coefficient	$[-]$
K_t	Transport coefficient	$[-]$
L	Length	$[\mathrm{m}]$
M	Mass, molecular mass	$[\mathrm{kg, g/mol}]$
m	Mass flow rate	$[\mathrm{kg/s}]$
N	Sample size	$[-]$
n	Number	$[-]$
P	Power, probability, performance parameter	$[\mathrm{MW}, -, \mathrm{various}]$
p	Pressure	$[\mathrm{Pa}]$
Q	Heat transfer rate	$[\mathrm{MW}]$
R	Result, gas constant	$[\mathrm{various, J/kgK}]$
Ry	Characteristic flow parameter	$[\mathrm{m^{-1}}]$
r	Radius, range	$[\mathrm{m}, \mathrm{various}]$
s_X	Sample standard deviation	$[\mathrm{various}]$
s	Random standard uncertainty	$[\mathrm{various}]$
T	Temperature	$[^\circ\mathrm{C}, \mathrm{K}]$
t	Time, multiplier	$[\mathrm{s}, -]$
V	Volume flow rate, molecular volume	$[\mathrm{m^3/hr, m^3/mol}]$
v	Velocity, degrees of freedom	$[\mathrm{m/s}, -]$
W	Width	$[\mathrm{m}]$
w	Vapour fraction	$[\mathrm{kg/kg\ dry\ air}]$
X	Measured value/input	$[\mathrm{various}]$
Y	Measured output	$[\mathrm{various}]$

z	Elevation	[m]

Greek letters

α	Kinetic energy coefficient	[−]
β	Systematic error	[−]
Δ	Difference, change	[−]
δ	Total error	[various]
ϵ	Separability error	[°C or K]
ε	Random error	[various]
η	Efficiency	[−]
θ	Sensitivity index	[various]
μ	Dynamic viscosity, population mean	[N/m, various]
ξ	Temperature lapse rate	[K/m]
ρ	Density	[kg/m^3]
σ	Surface tension	[kg/ms]
ϕ	Crystal growth/removal rate	[kg/s]

Subscripts

a	Dry air, ambient
B	Base
b	Bulk, systematic uncertainty
byp	Bypass
c	Sensible (heat transfer), crystal
cal	Calibration
curr	Instrument
ct	Tower inlet
ctc	Contraction
cte	Expansion
D	Deposition
d	Droplet, discharge
db	Dry-bulb
de	Drift eliminators
digi	Digital
e	Equilibrium

fd	Friction and drag
fi	Fill
fr	Frontal
fs	Fill support
I/O	Input/output
i	Inlet
instr	Instrument
m	Latent (heat transfer), mean, mixture
meas	Measured
nzl	Nozzle
o	Outlet
pnz	Pre-nozzle
R	Removal, result
rz	Rain zone
s	Saturated
sig	Signal
sp	Spray zone
ss	Suspended solids
ts	Tower support
v	Vapour
w	Water
wb	Wet-bulb
wd	Water distribution
z	Zone

Dimensionless groups

Fr_D	Densimetric Froude number, $\rho v^2/(\Delta\rho dg)$
Le_f	Lewis factor, $h/(c_p h_d)$
Me	Merkel number, $h_d a_{fi} L_{fi}/G_w$
Sc	Schmidt number, $\mu/(\rho D)$

Chapter 1: Introduction

1.1 Natural draught wet cooling towers in Rankine cycle power plants

Natural draught wet cooling towers (NDWCTs) are used worldwide to provide process cooling, including to both nuclear and conventional steam-turbine power plants, where they provide the cooling required to condense turbine exhaust steam.

Figure 1.1 shows the primary (Rankine) and secondary (cooling) cycles of a conventional indirect wet-cooled steam-turbine power plant. The primary cycle utilises a boiler feedwater pump (or pumps) which feeds water to a boiler at high pressure. Heat is added to the water in the boiler, turning it into superheated steam. This steam flows to the turbine, which produces mechanical power (rotation) by extracting enthalpy from the steam. The mechanical power is converted to electrical power by a generator connected to the turbine. Steam exits the turbine to the shell side of a shell- and tube heat exchanger called the steam surface condenser (SSC). Here the steam is condensed to water, which flows back to the boiler feedwater pump, completing the cycle.

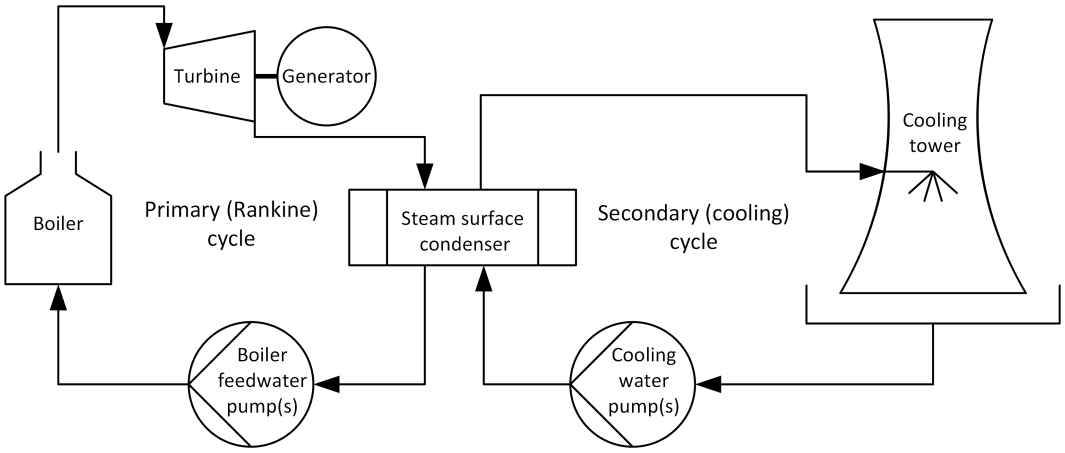

Figure 1.1: Conventional power plant primary and secondary cycles

The water in the secondary cycle, known as cooling water, is isolated from the water/steam of the primary cycle. The secondary cycle utilises a cooling water pump (or pumps) which supplies cooling water to the tube side of the SSC. The cooling water inside the tubes is heated by the condensing steam outside the tubes, exits the SSC and flows to the NDWCT through large pipes. The hot cooling water is cooled in the NDWCT while losing a portion of its mass

flow to evaporation. The cold cooling water exiting the NDWCT returns to the cooling water pump, completing the cycle.

The shell side of the SSC operates under vacuum due to the high rate of condensation taking place. Since a phase change from steam to water takes place in the SSC shell side, the operating temperature and pressure are coupled, meaning that the SSC shell side pressure has a direct influence on the primary cycle efficiency (Cengel and Boles, 2006). There is also a maximum allowable condenser pressure, determined by the turbine manufacturer (McCloskey *et al.*, 2011), and to avoid exceeding this limit, it may be necessary to reduce the steam mass flow through the turbine, and thus the power produced by the turbine, under certain conditions. This results in a "load loss": the unwanted reduction in electricity generation capacity of the power plant.

The condensation rate, and consequently the operating pressure, in the SSC is dependent on its cooling capacity, which in turn is a function (amongst other influencing factors) of the tube-side cooling water inlet temperature as supplied from the NDWCT. The cooling capacity of the NDWCT serving the power plant therefore has a direct impact on the power plant's revenue generating capacity (avoidance of load losses) and fuel cost (primary cycle efficiency).

1.2 NDWCT operation

A NDWCT (see Figure 1.2) consists of a cylindrical or hyperboloid shell constructed from steel or concrete with cooling water from the SSC (or other process) entering the shell into a system of elevated pipes. The cooling water exits the pipes through sprayers spaced over the shell cross-section, with the space occupied by sprayed water known as the spray zone. The sprayed cooling water falls onto the porous medium, known as fill, and moves downward through the fill due to gravity, exiting at the bottom. Below the fill, the cooling water falls as a dense rain into the pond, with the space between the fill and the pond known as the rain zone. From the pond, the cooling water is collected and returned to the SSC via the cooling water pump(s).

Sensible heat transfer and enthalpy transfer from the cooling water to air in the shell takes place in the spray zone, fill and rain zone. The heated and moistened air inside the shell has a lower density than the atmospheric air surrounding the shell, with the resulting buoyancy causing an upward airflow inside the shell. As the moistened air leaves the top of the shell, fresh atmospheric air is drawn into the bottom of the shell, creating a "natural draught". While heat transfer generally takes place from the cooling water to the air, as in Kröger (2004), there are certain conditions where the air is cooled by the water, with the draught being generated by the lower density of moistened air only (Kloppers and Kröger, 2004).

Atmospheric air enters the NDWCT through the inlet at the bottom of the shell, being partially restricted by the shell supports. The air flows horizontally

through the rain zone and turns to flow upward through the fill and spray zone, losing pressure due to both the elevation change and flow restrictions. The air-flow entrains some droplets as it moves upwards through the spray zone. The drift eliminators, installed above the sprayers, remove virtually all entrained droplets from the air-flow, reducing the NDWCT's water consumption, while causing an increased air-flow restriction. Air continues to flow upwards, ultimately existing at the top of the shell. The air-flow rate through the shell is determined by the balance of the upward draught and losses caused by the zones and components in the NDWCT.

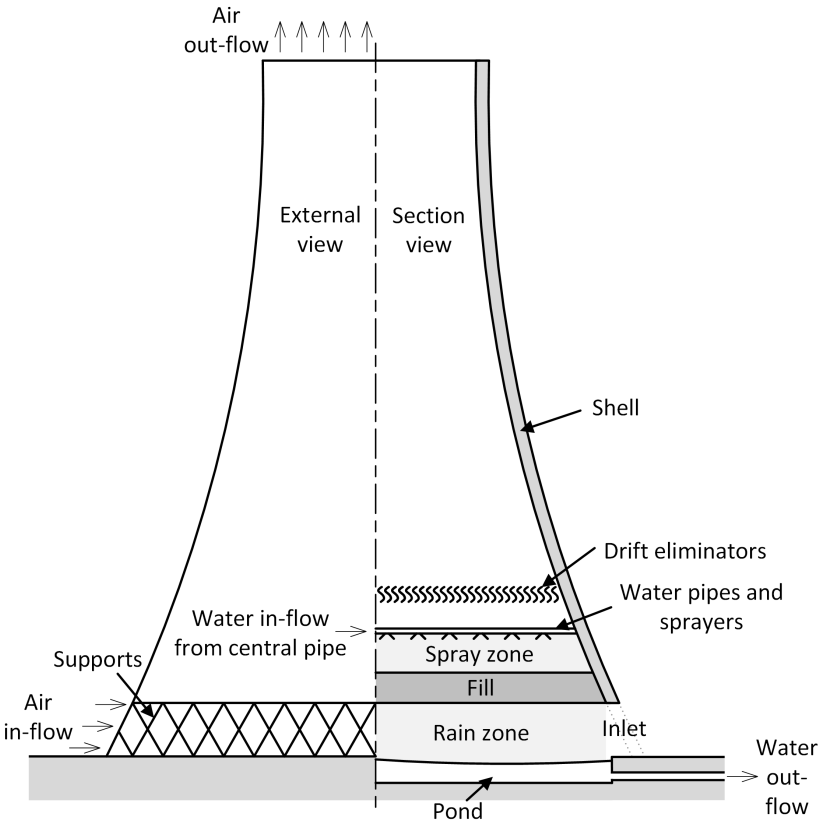

Figure 1.2: NDWCT layout and internal components (adapted from Kröger (2004))

1.3 NDWCT fill

The cooling capacity of NDWCTs is improved by the installation of fill, which increases the surface area and contact time between the air and cooling water. Fills are constructed from wood, metal, asbestos or various plastics in the form of slats, sheets or lattices, which aim to spread the cooling water in a thin layer across a large surface area, break the flow into small droplets or some combination of these methods. The measure of a fill's performance is a

combination of its thermal (heat and mass transfer) and hydraulic (air-pressure loss) performance (Monjoie *et al.*, 1993).

1.3.1 NDWCT fill fouling

NDWCTs, and especially the fills, are subject to fouling. NDWCTs operate in ambient air which may contain dust, atmospheric pollutants and biological matter such as grasses, seeds or spores. The cooling water used in NDWCTs may contain biological, chemical and mineral contaminants, either from its source state or due to contaminant exposure during operation. NDWCTs utilise evaporation for part of their cooling capacity, which concentrates any dissolved solids in the cooling water (Kröger, 2004).

Fill fouling terminology differs slightly between sources and is therefore defined for this study as all unwanted build-up of organic and inorganic contaminants on the fill surface. This includes scale (see Section 3.1), which is categorised separately by some sources, such as Aull (2013) and Monjoie (2009). The definition does not include the initial period of some fills' operation, known as ageing, during which small amounts of deposit may form on the fill surface, with fill performance generally increasing during this period (Zaorski and Miller, 2017).

Fill fouling formation, growth and its performance effects are dependent on factors such as fill design, cooling water quality, temperature and cooling water flow rates, among possible others, and can range from negligible to extreme, based on these factors (this is discussed in detail in Chapter 3). Fouling leads to fill mass gain, while reducing both the thermal and hydraulic performance of fills (Monjoie *et al.*, 1993). Consequently, fill fouling results in reduced cooling tower capacity, increased SCC pressures, reduced primary cycle efficiency and increased fuel costs at conventional steam-turbine power plants. As reported in Augustyn (2019), extreme cases of fouling may lead to load losses and even the structural collapse of fills.

1.3.2 NDWCT fill types

Numerous fill designs are available, or have previously been available, from various suppliers. In general, each design falls into one of a number of fill types and due to the differences in the performance and fouling behaviour of these types, a brief discussion of each fill type is provided.

1.3.2.1 Splash fill

Splash fill designs (see Figure 1.3) aim to break the cooling water flow into numerous small droplets to increase the surface area in contact with the air. This is done by creating more and smaller droplets through a combination of three mechanisms according to Michaels (2015): droplets create splashes when they fall onto the top of the fill slats or into small troughs or pools formed by the fill, falling droplets impacting the edges of the fill are cut and droplets

dripping from the fill slats.

Splash fills are manufactured from metal or plastics and take various forms. Different layers of fill are typically spaced vertically at 200 mm to 600 mm intervals, suspended in position with steel wires, up to an installed height of 5 m to 8 m (Kröger, 2004). The advantage of splash fills is that they are highly resistant to fouling (Monjoie, 2009; Dahm *et al.*, 2015) while the main disadvantage is low thermal performance per fill volume, requiring fill heights much greater than other fill types and the consequent construction of larger cooling towers for the same thermal performance (Puckorius, 2013). Additionally, due to their mechanism of operation, splash fills cause greater entrainment of droplets in the upward air-flow than other fill types, resulting in higher rates of water loss to the environment (Kröger, 2004).

1.3.2.2 Asbestos cement fill

Asbestos cement fill consists of vertically installed parallel flat or corrugated asbestos cement sheets installed in several layers (see Figure 1.4) up to a height of 1.8 m to 2.5 m (as seen in Kröger (2004)). The design aims to spread the cooling water flow in a thin layer over the fill surface to maximise the surface area of cooling water in contact with the air-flow.

Figure 1.3: Splash fill (Augustyn, 2017)

Figure 1.4: Asbestos cement fill installed in a NDWCT, viewed from below (Ruszkowski, 2016)

According to Kröger (2004), advantages of this type of fill include low pressure drop for the thermal performance, while disadvantages include possible uneven cooling water distribution, which reduces heat transfer effectiveness, and an increased fouling tendency compared to splash fills due to lower water velocities. Bosman (1985) considers asbestos cement fill to have superior long-term structural integrity compared to modern plastic fills.

Due to the health risks associated with asbestos, the South African government has banned the manufacture and installation of new asbestos components (Republic of South Africa. Department of environmental affairs and tourism,

2008), as has many other countries (Bosman, 1985). While asbestos cement was once widely used, it is due to these health risks and regulations that asbestos cement is no longer specified in new installations and, where installed, is being gradually replaced with fills of other materials (Ruszkowski, 2016).

1.3.2.3 Film fill

Film fill designs were first developed in the 1970s and 1980s to provide increased thermal performance compared to splash fills and asbestos cement fills (Mortensen and Conley, 1994; Zaorski and Miller, 2017). Film fill consists of thin corrugated or flat plastic sheets that are formed and bonded together to create flow paths, known as cores or flutes, for the cooling water and air. Like asbestos cement fill, film fill makes use of a thin layer of water forming over the fill surface to increase the contact area between the water and air, but the plastic construction allows the design of complex flute routes to further increase mixing of the flows and residence time.

Three sub-types of film fills exist, categorised by their flute routing: vertical fluted (shown in Figure 1.5), vertical offset and cross-corrugated. These have, respectively, the lowest, intermediate and highest of thermal performance, pressure drop and fouling potential (Puckorius, 2013). While the installed fill height is expected to vary depending on the sub-type and specific design of film fill selected, Whittemore and Massey (1992) indicates cases requiring only 0.9 m to 1.2 m.

Advantages of film fills include good thermal performance due to their large surface area to volume ratio (Puckorius, 2013) as well as strength, durability and low weight (Kröger, 2004). According to Puckorius (2013), the main disadvantage of film fills are their propensity to fouling .

1.3.2.4 Trickle fill

Trickle fills (see Figure 1.6) are a relatively new type of fill (Kröger, 2004), which are contructed as metal mesh or plastic injection moulding to create a "wire-frame" of thin members along which cooling water droplets can run, exposing the droplets to the air-flow. According to Dahm *et al.* (2015), the thermal performance of some of these fills are comparable with some vertical fluted and vertical offset film fills.

Advantages of this fill type are that they can be assembled at the installation location, resulting in reduced transport costs, and that some designs allow cleaning using high-pressure water (Dahm *et al.*, 2015), whereas most other fill types are difficult or impossible to clean after installation. The disadvantage of this type is that some designs have a similar propensity to fouling as film fills (Zaorski and Miller, 2017). Installed heights may vary widely due to the large performance range of different design of this fill type, as seen in Dahm *et al.* (2015).

Some modern fill designs, known as modular splash fills, externally resemble

trickle fills, however, like splash fills, they rely on droplet formation to increase the contact area between the cooling water and air-flow. This is done by creating downward-facing points or edges in the fill where droplets form and fall from, which allows these fills to maintain a similar resistance to fouling as traditional splash fills (Dahm *et al.*, 2015).

Figure 1.5: Vertical fluted film fill (Augustyn, 2018)

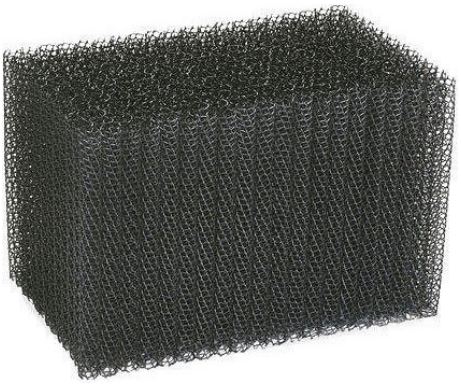

Figure 1.6: Trickle fill (Augustyn, 2017)

1.4 Study background

Eskom, South Africa's state-owned power utility, operates 61 NDWCTs in its fleet of 15 coal-fired power stations. Of these NDWCTs, 36 contain asbestos cement fill, 16 splash fill and 9 trickle fill. Due to the health risks associated with asbestos, Eskom has decided to remove all asbestos from its operating plants, including asbestos cement fills in its NDWCTs, by 2033. Furthermore, a number of Eskom power stations have experienced severe fill fouling, which has led to reduced NDWCT cooling capacity and consequently to primary cycle efficiency losses and load losses. Due to these reasons, Eskom has to replace large amounts of NDWCT fill in the near future, with the total cost estimated to be several billion South African Rand.

Due to the large capital investment and the risks of making incorrect fill selections, Eskom has decided to investigate methods to reduce the uncertainties in selecting replacement fill designs. This requires analysis of the performance of four cooling tower fill characteristics (similar to the fill characteristics in Troncin (2012)): thermal and hydraulic performance, fouling performance, fire resistance and structural integrity.

While supplier performance guarantees have historically been relied on to ensure performance in operation, they are not seen by Eskom as adequate for fill replacement contracts for the following reasons:

(i) Performance tests of NDWCTs are affected by both atmospheric conditions and power plant performance and off-design operation during testing makes enforcement of penalties based on these tests difficult.

(ii) Fill fouling performance is heavily dependent on cooling water chemistry and this may change with time as raw water sources and treatment methods are changed. This also makes it difficult to determine how a fill will perform, in terms of fouling, at a specific location.

(iii) Guarantee periods usually last only a few years at best, while some of the fill deficiencies may only be revealed after many years of operation.

While all of the issues mentioned above cannot be countered fully, Eskom has nonetheless decided to perform in-house testing of NDWCT fills as part of the commercial comparison of fills. Before this is done, better understanding of the testing methods and interpretation of testing data on the four performance characteristics was sought to ensure fair commercial comparison between competing fill designs. This study considers the fouling performance of NDWCT fills and utilises a fill fouling test facility installed in late 2018 at an Eskom coal-fired power station.

1.5 Motivation

This study is motivated by Eskom's need, as a state-owned company, to adequately justify its commercial decisions. In the case of NDWCT fill replacement, the selection of a specific replacement fill carries the risk of primary cycle efficiency reduction and load losses due to NDWCT performance degradation caused by fill fouling. A method or methods to quantify the impact of this risk would allow Eskom, or other power utilities, to better justify fill selection decisions.

The testing performed during this study presents an opportunity to investigate fill fouling in conditions closely approximating actual operation, using actual cooling water at a power station, as well as detailed thermal and hydraulic testing of the fills while operating for months or even years. As such, this study is partially motivated by the availability and capabilities of the fill fouling test facility.

1.6 Objectives

The objectives of this study are to:

(i) Determine how to best quantify the fouling of NDWCT fills and how to use this quantification to compare different fills for commercial consideration.

(ii) Critically analyse the Eskom fill fouling test facility design and results.

(iii) Apply the developed methods to the fouling test results of a minimum

of four fill designs and draw conclusions.

1.7 Limitations

The limitations relevant to this study are:

(i) The fill fouling test facility was procured by Eskom, with the design and some of the manufacturing having been completed by the start of this study. The test facility was operated and maintained by the manufacturing contractor for the duration of this study, in line with the contractual stipulations. The candidate had no authority to change the design, perform repairs or make modifications.

(ii) The fill fouling test facility was designed for long-term continuous testing and does not allow for frequent shut-downs, calibration and verification of measurements.

(iii) The testing data utilised in this study consists of less than a year of continuous testing. Fill fouling testing done at an operational NDWCT by Whittemore and Massey (1992) took 35 to 50 months to show approximately steady-state conditions for fill mass gain. Any conclusions drawn from the Eskom fill fouling test facility about the long-term fouling performance of the tested fills in this study may therefore not be viewed as accurate. The methods developed to quantify the effects of fill fouling are, however, applicable generally at the Eskom fill fouling test facility or another fill fouling test facility where sufficient testing data is available.

1.8 Thesis outline

1.8.1 Chapter 1

Chapter 1 presents an introduction to NDWCT operation, as well as the background, motivation, objectives and limitations of this study.

1.8.2 Chapter 2

Chapter 2 provides the cooling tower performance prediction theory, starting with derivation of the Merkel method of heat- and mass-transfer quantification and showing how this is applied in a one-dimensional NDWCT model. The calculation of NDWCT performance using power plant heat rate correction is also introduced. Appendix D shows a sample calculation of NDWCT performance prediction, including heat rate correction.

1.8.3 Chapter 3

Chapter 3 contains a summary of the available literature of NDWCT fill fouling: the different types of fouling are defined, along with discussions on how each type forms, grows and is controlled. Literature on fill fouling quantifi-

cation methods, including the effects of fouling on fill performance is also provided.

1.8.4 Chapter 4

Chapter 4 presents the details of the Eskom fill fouling test facility, as well as the methods to utilise fill performance test data to calculate fill performance inputs to NDWCT performance prediction calculations. Appendix C shows a sample calculation of fill performance results at a single test operating point, as well as the use the results of all test operating points in a fill performance test to obtain the fill performance characteristic equations.

1.8.5 Chapter 5

Chapter 5 presents experimental uncertainty calculation theory and develops a general approach to fill performance measurement experimental uncertainty calculation and its propagation to NDWCT performance prediction uncertainty. The uncertainty considerations for the Eskom fill fouling test facility are discussed. Appendix E shows an example calculation of fill performance uncertainties for the fill in Appendix C and the propagation of these uncertainties to the NDWCT in Appendix D.

1.8.6 Chapter 6

Chapter 6 provides the statistical motivation for separation of the thermal and hydraulic effects of fouling. A method applying this separation is proposed for quantification of fill fouling as individual thermal and hydraulic fill fouling factors, which scale the thermal and hydraulic performance characteristic equation of the fill's initial measured performance. Appendix F shows a comparison of NDWCT performance calculated using the traditional fill performance characteristic equations and NDWCT performance calculated using fill fouling factors, as well as an example NDWCT lifecycle calculation using fill fouling factors.

1.8.7 Chapter 7

Chapter 7 presents the results obtained from the fill fouling test facility, including the measured fill performance (with uncertainties), as well as measured mass gains and visual inspections of fill fouling deposits.

1.8.8 Chapter 8

Chapter 8 contains concluding remarks, recommendations for testing and future work.

Chapter 2: NDWCT performance prediction

NDWCT performance prediction calculations form an integral part of the fill fouling quantification methods presented in this study. Kröger (2004) presents a one-dimensional NDWCT performance prediction model based on the Merkel method. The following sections present the Merkel method, before illustrating how Kröger (2004) employs this method in NDWCT performance prediction calculations. Power plant heat rate correction calculations are also introduced.

2.1 The Merkel method

The Merkel method was originally developed by Merkel (1926), and quantifies wet cooling heat and mass transfer in terms of the non-dimensional Merkel number. It is derived here for a NDWCT fill, as presented by Kloppers (2003), with L_{fi} denoting the fill height. A Merkel number is, however, defined for each of the three heat and mass transfer zones in a NDWCT (see Figure 1.2), as well as for the entire NDWCT. For zones other than the fill, or the entire NDWCT, L_{fi} denotes the air travel distance.

Figure 2.1 shows the control volume at the interface between cooling water (from now only called water) and air in a counterflow wet cooling tower with evaporation of water taking place. The differential elevation change is denoted by dz, while m denotes mass flow rate, i denotes enthalpy, w denotes the vapour mass fraction in air and the subscripts w, a and ma denote water, dry air and air-vapour mixture respectively. The mass balance of the control volume in Figure 2.1a is:

$$(m_w + dm_w) + m_a(1 + w) = m_w + m_a(1 + w + dw) \tag{2.1}$$

which simplifies to:

$$dm_w = m_a dw \tag{2.2}$$

The energy balance of the control volume in Figure 2.1b is:

$$(m_w + dm_w)(i_w + di_w) + m_a i_{ma} = m_w i_w + m_a(i_{ma} + di_{ma}) \tag{2.3}$$

Simplifying and neglecting second-order terms yield:

$$m_a di_{ma} - m_w di_w - i_w dm_w = 0 \tag{2.4}$$

The differential change in water enthalpy is expressed as:

$$di_w = c_{pw} dT_w \tag{2.5}$$

where c_{pw} is the specific heat capacity of water and T_w is the water temperature. With c_{pw} varying little in the temperature ranges applicable to wet cooling towers (approximately 0.7 % between 0 °C and 60 °C) and defining the

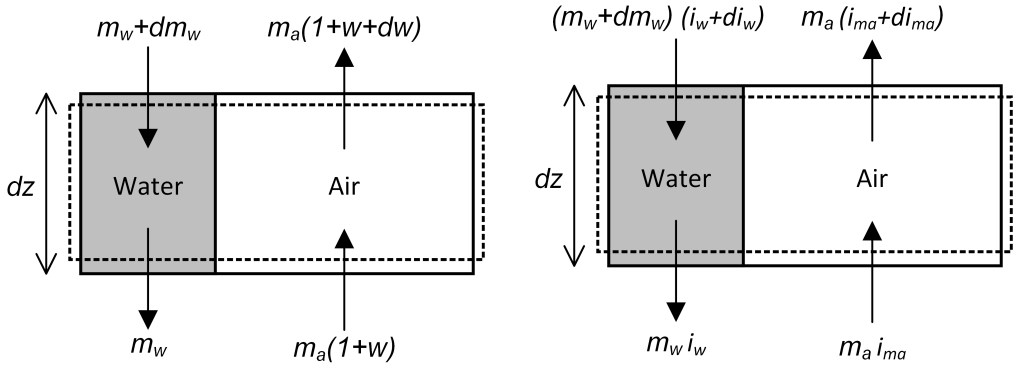

(a) Mass balance (b) Energy balance

Figure 2.1: Control volume of the water-air interface in a counterflow wet cooling tower (Kloppers, 2003)

enthalpy of water at 0 °C as 0 kJ/kg, the enthalpy of water can be expressed as:

$$i_w = c_{pw} T_w \tag{2.6}$$

with T_w in °C.

Substituting Equation 2.5 into Equation 2.4 yields:

$$m_w c_{pw} dT_w = m_a di_{ma} - i_w dm_w \tag{2.7}$$

Substituting Equation 2.2 and 2.6 into Equation 2.7 and rearranging yields:

$$dT_w = \frac{m_a}{m_w} \left(\frac{1}{c_{pw}} di_{ma} - T_w dw \right) \tag{2.8}$$

The heat transfer rate at the water-air interface is expressed as:

$$dQ = dQ_m + dQ_c \tag{2.9}$$

where Q is the total heat transfer rate, Q_m is the enthalpy transfer rate and Q_c is sensible heat transfer rate. Mass transfer is defined as:

$$dm_w = h_d (w_{sw} - w) dA \tag{2.10}$$

where h_d is the mass transfer coefficient, w_{sw} is the vapour fraction of the air saturated with water vapour and dA is the differential surface area of the water-air interface. The enthalpy transfer rate is then:

$$dQ_m = i_v dm_w = i_v h_d (w_{sw} - w) dA \tag{2.11}$$

where i_v is the enthalpy of water vapour at T_w, defined as:

$$i_v = i_{fgw0} + c_{pv} T_w \tag{2.12}$$

where i_{fgw0} is the heat of vaporisation at 0 °C (see Equation A.15) and c_{pv} is the specific heat capacity of water vapour.

Sensible heat transfer is defined as:

$$dQ_c = h(T_w - T_a)dA \tag{2.13}$$

where h is the heat transfer coefficient and T_a the air temperature. The enthalpy of saturated air at T_w is:

$$i_{masw} = c_{pa}T_w + w_{sw}i_v \tag{2.14}$$

where c_{pa} is the specific heat capacity of dry air. The enthalpy of the air-vapour mixture at T_a is expressed as:

$$i_{ma} = c_{pa}T_a + wi_v \tag{2.15}$$

Subtracting Equation 2.15 from Equation 2.14 yields:

$$i_{masw} - i_{ma} = c_{pa}T_w + w_{sw}i_v - c_{pa}T_a - wi_v \tag{2.16}$$

The specific heat capacity of the air-vapour mixture is defined as:

$$c_{pma} = c_{pa} + wc_{pv} \tag{2.17}$$

Equation 2.16 is converted from using the dry air specific heat capacity (c_{pa}) to use the specific heat capacity of the air-vapour mixture (c_{pma}) by assuming that $c_{pa} \approx c_{pma}$. Subsequently rearranging Equation 2.16 yields:

$$T_w - T_a = \frac{(i_{masw} - i_{ma}) - (w_{sw} - w)i_v}{c_{pma}} \tag{2.18}$$

Substituting Equation 2.18 into Equation 2.13 results in:

$$\begin{aligned} dQ_c &= h\left(\frac{(i_{masw} - i_{ma}) - (w_{sw} - w)i_v}{c_{pma}}\right)dA \\ &= h_d\left(\frac{h}{c_{pma}h_d}(i_{masw} - i_{ma}) - \frac{h}{c_{pma}h_d}(w_{sw} - w)i_v\right)dA \end{aligned} \tag{2.19}$$

Substituting Equation 2.11 and Equation 2.19 into Equation 2.9 yields:

$$dQ = h_d\left(\frac{h}{c_{pma}h_d}(i_{masw} - i_{ma}) - \left(1 - \frac{h}{c_{pma}h_d}\right)(w_{sw} - w)i_v\right)dA \tag{2.20}$$

The Lewis factor, an indication of the relative rates of heat and mass transfer, is defined as:

$$Le_f = \frac{h}{c_{pma}h_d} \tag{2.21}$$

Substituting Equation 2.21 into Equation 2.20 yields:

$$dQ = h_d\big[Le_f(i_{masw} - i_{ma}) - (1 - Le_f)(w_{sw} - w)i_v\big]dA \tag{2.22}$$

With:

$$di_{ma} = \frac{dQ}{m_a} \tag{2.23}$$

dividing Equation 2.22 by m_a yields:

$$di_{ma} = \frac{h_d}{m_a}\left[Le_f(i_{masw} - i_{ma}) - (1 - Le_f)(w_{sw} - w)i_v\right]dA \tag{2.24}$$

The differential heat and mass transfer area for a fill is written as:

$$dA = a_{fi}A_{fr}dz \tag{2.25}$$

where a_{fi} is the fill surface area per unit volume and depends on the fill design and A_{fr} is the fill frontal area. Substituting Equation 2.25 into Equation 2.24 gives the general differential equation of enthalpy change with height in a cooling tower fill:

$$\frac{di_{ma}}{dz} = \frac{h_d a_{fi} A_{fr}}{m_a}\left[Le_f(i_{masw} - i_{ma}) - (1 - Le_f)(w_{sw} - w)i_v\right] \tag{2.26}$$

From here, two simplifying assumptions are made: that the value of Le_f is 1 and that evaporative loss is negligible, i.e. $dw = 0$. The first assumption reduces Equation 2.26 to:

$$\frac{di_{ma}}{dz} = \frac{h_d a_{fi} A_{fr}}{m_a}(i_{masw} - i_{ma}) \tag{2.27}$$

The second assumption reduces Equation 2.8 to:

$$\frac{dT_w}{dz} = \frac{m_a}{m_w}\frac{1}{c_{pw}}\frac{di_{ma}}{dz} \tag{2.28}$$

Inserting Equation 2.27 into Equation 2.28 yields:

$$dT_w = \frac{m_a}{m_w}\frac{1}{c_{pw}}\frac{h_d a_{fi} A_{fr}}{m_a}(i_{masw} - i_{ma})dz \tag{2.29}$$

Rearranging and integrating from the bottom to the top of the fill yields:

$$\int_{T_{wo}}^{T_{wi}} \frac{c_{pw}}{i_{masw} - i_{ma}} dT_w = \int_{z_b}^{z_t} \frac{h_d a_{fi} A_{fr}}{m_w} dz \tag{2.30}$$

where T_{wo} and T_{wi} are the outlet (bottom) and inlet (top) water temperatures respectively, and z_b and z_t are the bottom and top fill elevations respectively. The resulting integral is the definition of the Merkel number (Merkel, 1926):

$$Me = \int_{T_{wo}}^{T_{wi}} \frac{c_{pw}}{i_{masw} - i_{ma}} dT_w = \frac{h_d a_{fi} L_{fi}}{G_w} \tag{2.31}$$

where L_{fi} is the fill height $(z_t - z_b)$ and G_w is the fill water mass flux, based on the fill frontal area (A_{fr}). The values of a_{fi} and h_d are difficult or impossible to determine and values on the right-hand side of the expression are never used in calculations (Kloppers, 2003). The Merkel number is only determined using the integral form. This method does not allow the calculation of the outlet air conditions of the zone or the entire NDWCT under consideration. It is therefore assumed that the outlet air is saturated with vapour, which allows calculation of the necessary outlet fluid properties.

2.2 NDWCT performance prediction calculation

NDWCT performance prediction calculations are performed according to the method described in Kröger (2004), which consists of the simultaneous solution of the draught, heat- and mass-transfer and energy equations. The draught equation states that the change in static pressure over the height of the NDWCT due to both elevation change and mechanical energy losses caused by air-flow obstructions is equal to the atmospheric pressure reduction due to elevation change only outside the tower ($\Delta p_{tower} = \Delta p_{elevation}$). The heat- and mass-transfer equation (also known simply as the transfer equation) states that the Merkel number of the entire NDWCT is equal to the sum of the Merkel numbers of the spray, fill and rain zones ($Me_{tower} = Me_{sp} + Me_{fi} + Me_{rz}$). Finally, the energy equation states that the rate of heat loss by the water is equal to the rate of heat gain by the air ($Q_{water} = Q_{air}$). The details of each of these simultaneous equations is discussed separately in the following sections. Where empirical equations are referenced to other sources, these are as referenced by Kröger (2004).

2.2.1 The draught equation

The elements of the draught equation are described in the following sections. Sections 2.2.1.1 to 2.2.1.10 describe the quantification of mechanical energy losses in the air-flow path through the use of pressure loss coefficients. Section 2.2.1.11 describes the pressure reduction, due to elevation change, in the column of vapour-saturated air rising above the fill, while Section 2.2.1.12 describes the pressure difference at the shell outlet elevation between the inside and outside of the NDWCT. Section 2.2.1.13 describes the pressure reduction, due to elevation change, in atmospheric air, which applies from ground level to the fill inside the NDWCT, as well as from ground level to the shell outlet outside the NDWCT. Finally, Section 2.2.1.14 describes the combination of the various equations in Sections 2.2.1.1 to 2.2.1.13 to generate the draught equation. Figure 2.2 shows the main NDWCT dimensions, numbered locations and pressure loss elements used in these calculations. The numbered locations are used as subscripts in the calculations that follow to indicate the location that fluid and flow property symbols refer to. Combined location subscripts (ij) indicate a mean property or parameter based on conditions at i and j.

2.2.1.1 Pressure loss coefficients

Mechanical loss elements in the NDWCT air-flow path are taken into account using pressure loss coefficients (K) of those elements, with the resultant pressure loss being calculated using:

$$\Delta p_j = \frac{K_j \rho_{avj} v_{avj}^2}{2} = \frac{K_j m_{avj}^2}{2 A_j^2 \rho_{avj}} \tag{2.32}$$

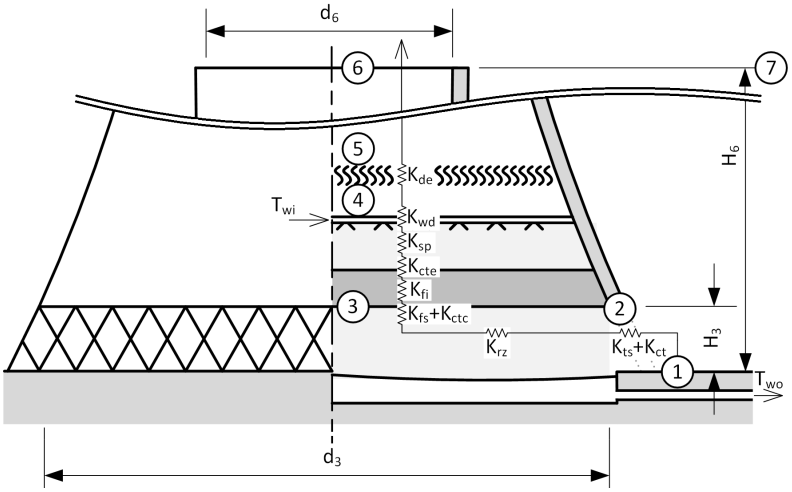

	Element
K_{ts}	Tower support
K_{ct}	Tower inlet
K_{rz}	Rain zone
K_{fs}	Fill support
K_{ctc}	Contraction
K_{fi}	Fill
K_{cte}	Expansion
K_{sp}	Spray zone
K_{wd}	Water distribution
K_{de}	Drift eliminators

	Location
1	Ground level
2	Air inlet
3	Bottom of fill
4	Above spray zone
5	Above drift eliminators
6	Outlet (inside shell)
7	Outlet (outside shell)

Figure 2.2: NDWCT dimensions, numbered locations and pressure loss elements (adapted from Kröger (2004))

where v_{avj} is the velocity, m_{avj} the mass flow and ρ_{avj} the density of the air-vapour mixture (subscript av) at pressure loss element j, while A_j is the frontal area of element j. Kröger (2004) simplifies the display of the draught equation, avoiding the use of the m_{av}, ρ and A of every element, by generating a modified pressure loss coefficient which refers to the fluid and flow conditions at the fill location, known as the pressure loss coefficient "referred to the fill" ($K_{j_{fi}}$), for each pressure loss element (j) using:

$$K_{j_{fi}} = K(\rho_{av15}/\rho_{avj})(A_{fr}/A_j)^2(m_{avj}/m_{av15})^2 \tag{2.33}$$

where location 15 denotes the mean fill location and A_{fr} denotes the fill frontal area.

2.2.1.2 Shell supports loss coefficient

The NDWCT shell is supported by concrete columns, usually arranged in a parallel, x- or v-shape, which cause an obstruction to the air-flow as it enters the shell. The support loss coefficient is expressed as:

$$K_{ts} = C_{dts}L_{ts}d_{ts}n_{ts}/(\pi d_3 H_3) \tag{2.34}$$

where C_{dts} denotes the drag coefficient, which is a function of the support shape and orientation, L_{ts} the length, d_{ts} the diameter and n_{ts} the number of supports. K_{ts} is referred to the fill using Equation 2.33 to yield:

$$K_{tsfi} = [C_{dts}L_{ts}d_{ts}n_{ts}A_{fr}^2/(\pi d_3 H_3)^3](\rho_{av15}/\rho_{av1})(m_{av1}/m_{av15})^2 \tag{2.35}$$

where the inlet area is calculated as $A_2 = \pi d_3 H_3$.

2.2.1.3 Shell inlet loss coefficient

A pressure loss is caused by separation and other disturbances at the shell inlet and the calculation of its pressure loss coefficient is dependent on the type of fill installed in the NDWCT. For film- and fiber sheet fills, the following expression

by Geldenhuys and Kröger (1986) is used:

$$K_{ct} = 0.072\ (d_3/H_3)^2 - 0.34\ (d_3/H_3) + 1.7 \tag{2.36}$$

which is referred to the fill using Equation 2.33:

$$K_{ctfi} = K_{ct}(\rho_{av15}/\rho_{av1}) \times (4A_{fr}/\pi d_3^2)^2 \times (m_{av1}/m_{av15})^2 \tag{2.37}$$

For splash or trickle fills, the loss coefficient is calculated for an inlet with no rain zone using the following equation from De Villiers and Kröger (2001):

$$\begin{aligned} K_{ct(norz)} = {} & 0.011266 \times e^{0.093\times d_3/H_3} K_{fi}^2 - 0.3105 \times e^{0.1085\times d_3/H_3} K_{fi} \\ & - 1.7522 + 4.5614 \times e^{0.131\times d_3/H_3} \\ & + \sinh^{-1}\Big[\{(10970.2 \times e^{-0.2442\times K_{fi}} + 1391.3) \\ & /(d_3/H_3 - 15.7258) + 1205.54 \times e^{-0.23\times K_{fi}} + 109.31\} \\ & \times \{2\ r_i/d_3 - 0.01942/(d_3/H_3 - 27.929) - 0.016866\}\Big] \end{aligned} \tag{2.38}$$

applicable where $7.5 \leq d_3/H_3 \leq 15$, $5 \leq K_{fi} \leq 25$ and $0 \leq r_i/d_3 \leq 0.02$, with r_i denoting the radius of the shell inlet rounding and K_{fi} denoting the fill loss coefficient (see Section 2.2.1.6). The loss coefficient is referred to the fill using Equation 2.33:

$$K_{ctfi(norz)} = K_{ct(norz)}(\rho_{av15}/\rho_{av1})(m_{av1}/m_{av15})^2(4A_{fr}/\pi d_3^2)^2 \tag{2.39}$$

The fill referred loss coefficient is corrected with the rain zone correction factor C_{rz} (De Villiers and Kröger, 2001):

$$\begin{aligned} C_{rz} = {} & \big[0.2394 + 80.1\ (0.0954/(d_3/H_3) + d_d) \times e^{0.395\times G_w/G_a} \\ & - 0.3195\ (G_w/G_a) - 966\ (d_d/(d_3/H_3)) \times e^{0.686\times G_w/G_a}\big] \\ & \times (1 - 0.06825\ G_w) K_{fi}^{0.09667} \times e^{8.7434\ (1/d_3 - 0.01)} \end{aligned} \tag{2.40}$$

where G_a is the dry air mass flux through the fill and d_d is the mean droplet diameter in the rain zone, which may be calculated as the Sauter mean droplet diameter using the following equation from Kröger (2004):

$$d_{dsm} = \sum_i n_{di} d_{di}^3 / \sum_i n_{di} d_{di}^2 \tag{2.41}$$

where n_{di} denotes the number of droplets with diameter d_{di}.

The fill referred and rain zone corrected shell inlet loss coefficient for splash or trickle fills is:

$$K_{ctfi} = C_{rz} K_{ctfi(norz)} \tag{2.42}$$

2.2.1.4 Rain zone loss coefficient

The loss coefficient in the rain zone is expressed as:

$$\begin{aligned} K_{rz} = 3a_v v_{w3}(H_3/d_d)\Big[&0.2246 - 0.31467\ a_\rho \rho_{av1} + 5263.04\ a_\mu \mu_{av1} \\ &+ 0.775526\ (1.4824163\ e^{71.52\ a_L d_d} - 0.91) \\ &\times (0.39064\ e^{0.010912\ a_L d_3} - 0.17) \\ &\times (2.0892\ (a_v v_{av3})^{-1.3944} + 0.14) \times e^k\Big] \end{aligned} \tag{2.43}$$

where:

$$\begin{aligned} k = &(0.8449\ \ln(a_L d_3/2) - 2.312) \times (0.3724\ \ln(a_v v_{av3}) + 0.7263) \\ &\times \ln(206.757\ (a_L H_3)^{-2.8344} + 0.43) \end{aligned} \tag{2.44}$$

and μ denotes dynamic viscosity and the subscript w denotes water. The applicability ranges for Equation 2.43 are:

$0.00075\ \text{m/s} \leq v_w \leq 0.003\ \text{m/s}$	$10\ ^\circ\text{C} \leq T_w \leq 40\ ^\circ\text{C}$
$0.0696\ \text{N/m} \leq \sigma_w \leq 0.0742\ \text{N/m}$	$0.002\ \text{m} \leq d_d \leq 0.008\ \text{m}$
$0.927\ \text{kg/m}^3 \leq \rho_a \leq 1.289\ \text{kg/m}^3$	$0\ ^\circ\text{C} \leq T_a \leq 40\ ^\circ\text{C}$
$1\ \text{m/s} \leq v_{azo} \leq 3\ \text{m/s}$	$4\ \text{m} \leq H_3 \leq 12\ \text{m}$
$992.3\ \text{kg/m}^3 \leq \rho_w \leq 1000\ \text{kg/m}^3$	$9.7\ \text{m/s}^2 \leq g \leq 10\ \text{m/s}^2$
$1.717 \times 10^{-5}\ \text{kg/ms} \leq \mu_a \leq 1.92 \times 10^{-5}\ \text{kg/ms}$	$30\ \text{m} \leq d_i/2 \leq 70\ \text{m}$

with σ_w denoting surface tension, g denoting gravitational acceleration and the subscript wo denoting the water outlet conditions of the NDWCT. Flow velocities in Equation 2.43 and 2.44 are calculated using:

$$v_{w3} = G_w/\rho_{wo} \tag{2.45}$$

$$v_{av3} = m_{av1}/(\rho_{av1} A_{fr}) \tag{2.46}$$

$$v_{azo} = m_a/(\rho_{av1} A_{fr}) \tag{2.47}$$

Equations for the coefficients in Equation 2.43 and 2.44 are:

$$a_\mu = 3.061 \times 10^{-6}\ [\rho_{wo}^4 g^9/\sigma_{wo}]^{0.25} \tag{2.48}$$

$$a_\rho = 998.0/\rho_{wo} \tag{2.49}$$

$$a_v = 73.298\ [g^5 \sigma_{wo}^3/\rho_{wo}^3]^{0.25} \tag{2.50}$$

$$a_L = 6.122\ [g\sigma_{wo}/\rho_{wo}]^{0.25} \tag{2.51}$$

The rain zone loss coefficient is referred to the fill using Equation 2.33:

$$K_{rzfi} = K_{rz}(\rho_{av15}/\rho_{av1})(4A_{fr}/\pi d_3^2)^2 (m_{av1}/m_{av15})^2 \tag{2.52}$$

2.2.1.5 Fill support and contraction loss coefficient

The fill support structure usually consists of beams beneath the fill, causing an obstruction to the air-flow. Additionally, the fill may not cover the entire cooling tower cross-section, with the remaining area being blocked by plates (or similar devices), causing a flow contraction loss. The loss coefficient symbols for these are K_{fs} and K_{ctc} respectively. Kröger (2004) does not provide specific

values or equations for these, but uses a value of 0.5 for $K_{fs} + K_{ctc}$ in example calculations. Referred to the fill using Equation 2.33, this is expressed as:

$$(K_{fs} + K_{ctc})_{fi} = 0.5\ (\rho_{av15}/\rho_{av1})(m_{av1}/m_{av15})^2 \tag{2.53}$$

If additional information is available for these loss coefficients for specific NDWCT installations, that should be used and referred to the fill.

2.2.1.6 Fill loss coefficient

The fill pressure loss coefficient is one of the main performance parameters of the cooling tower fill, along with the Merkel number. The pressure loss coefficient (K_{fd}, where the subscript fd denotes friction and drag) is not constant and is usually characterised as a function of G_w and G_a for a specific fill design.

The fill loss coefficient is usually characterised by the supplier or other party from data obtained in a test program which results in an empirical characteristic pressure loss equation for a specific fill design. There are a number of accepted forms of this equation, including (from Kröger (2004)):

$$K_{fd} = aL_{fi}G_w^b G_a^c \tag{2.54}$$

while Kloppers (2003) suggests taking account of variation in the fill height with:

$$K_{fd} = aG_w^b G_a^c L_{fi}^d \tag{2.55}$$

In each case the coefficients a through c (or d) are determined experimentally.

Because of the large amount of heat and mass transfer taking place in the fill, the pressure loss coefficient as used in the NDWCT performance prediction calculation, K_{fi}, takes account of both static and dynamic pressure loss through the fill using the following equation:

$$\begin{aligned} K_{fi} &= [(p_i + \rho_{avi}v_{avi}^2/2) - (p_o + \rho_{avo}v_{avo}^2/2)]/(\rho_{avm}v_{avm}^2/2) \\ &= \left[\Delta p_{fd} + (\rho_{avo}v_{avo}^2 - \rho_{avi}v_{avi}^2) + (\rho_{avi}v_{avi}^2/2 - \rho_{avo}v_{avo}^2/2)\right] \\ &\quad / \left(\rho_{avm}v_{avm}^2/2\right) \\ &= K_{fd} + (\rho_{avo}v_{avo}^2/2 - \rho_{avi}v_{avi}^2/2)/\left(\rho_{avm}v_{avm}^2/2\right) \\ &= K_{fd} + (G_{avo}^2/\rho_{avo} - G_{avi}^2/\rho_{avi})/(G_{avm}^2/\rho_{avm}) \end{aligned} \tag{2.56}$$

where the change in static pressure is calculated using:

$$\Delta p_{fd} = p_i - p_o = \frac{K_{fd}\rho_{avm}v_{avm}^2}{2} \tag{2.57}$$

and subscripts i, o and m denote the fill air inlet (bottom), outlet (top) and mean locations respectively and where:

$$\rho_{avm} = 2/(1/\rho_{avi} + 1/\rho_{avo}) \tag{2.58}$$

$$G_{avm} = (G_{avi} + G_{avo})/2 \tag{2.59}$$

The use of Equation 2.33 is not required here since fluid and flow properties of the fill are used to perform the pressure loss coefficient calculation.

2.2.1.7 Expansion loss coefficient

If the fill does not cover the entire tower cross-section, the flow expands downstream of the fill, with a resultant flow expansion loss. The coefficient for this loss is expressed as:

$$K_{cte} = \left(1 - \frac{A_{fr}}{A_3}\right)^2 \tag{2.60}$$

This is referred to the fill using Equation 2.33:

$$K_{ctefi} = K_{cte}(\rho_{av15}/\rho_{av5})(m_{av5}/m_{av15})^2 \tag{2.61}$$

2.2.1.8 Spray zone loss coefficient

The falling water droplets in the spray zone cause an air-flow pressure loss, with the loss coefficient expressed by Cale (1982) as:

$$K_{sp} = L_{sp}[0.4\ (G_w/G_a) + 1] \tag{2.62}$$

and referred to the fill using Equation 2.33:

$$K_{spfi} = K_{sp}(\rho_{av15}/\rho_{av5})(m_{av5}/m_{av15})^2 \tag{2.63}$$

2.2.1.9 Water distribution system loss coefficient

The value of the loss coefficient for the piping and ducts in the water distribution system used by Kröger (2004) is $K_{wd} = 0.5$ and is utilised in this study. The resulting equation for the pressure loss factor referred to the fill using Equation 2.33 is:

$$K_{wdfi} = 0.5\ (\rho_{av15}/\rho_{av5})(m_{av5}/m_{av15})^2 \tag{2.64}$$

If additional information is available for these loss coefficients for specific NDWCT installations, that should be used and referred to the fill.

2.2.1.10 Drift eliminators loss coefficient

The coefficient for the pressure loss caused by drift eliminators is expressed as:

$$K_{de} = a_{de} Ry_{de}^{b_{de}} \tag{2.65}$$

with the values for a_{de} and b_{de} being dependent on the drift eliminator design and the flow parameter Ry being calculated using:

$$Ry = m_{av5}/(\mu_{av5} A_{fr}) \tag{2.66}$$

Referring this to the fill using Equation 2.33 yields:

$$K_{defi} = K_{de}(\rho_{av15}/\rho_{av5})(m_{av5}/m_{av15})^2 \tag{2.67}$$

2.2.1.11 Pressure reduction in column of rising air above the fill

The column of rising air above the fill is assumed to be saturated with water vapour. As the air rises, it cools and water vapour condenses from it due to the reduced vapour capacity of cooler air. The static pressure reduction in the

column of rising air is expressed as:

$$p_{a34} - p_{a6} = p_{a5}\Big[1 - \big(1 + \xi_{Ta5}(H_6 - H_3 - L_{fi}/2) /T_{a5}\big)^{-0.021233\ (1+w_5)/(\xi_{Ta5}(w_5+0.622))}\Big] \tag{2.68}$$

where the temperature lapse rate is expressed as:

$$\xi_{Ta5} = \frac{-(1+w_5)g}{c_{pma5} + 3.6693\times10^{-8}\ w_5^2 p_{a5}\ e^{5406.1915/T_{a5}} i_e/T_{a5}^2} \times [1 + 0.42216\times10^{-11}\ w_5^2 p_{a5}\ e^{5406.1915/T_{a5}} i_e /((w_5 + 0.622)\ R_a T_{a5})] \tag{2.69}$$

with the specific gas constant for dry air $R_a = 287.08$ J/kgK and the specific heat capacity for the air-vapour mixture is calculated using:

$$c_{pma5} = c_{pa5} + w_5 c_{pv5} \tag{2.70}$$

where c_{pa5} and c_{pv5} are evaluated at $(T_{a5} + 273.15\ \text{K})/2$, and:

$$i_e = i_{fgw0} - (c_{pw} - c_{pv})(T_{a5} - 273.15\ K) \tag{2.71}$$

2.2.1.12 Tower outlet pressure difference

The difference between the mean pressure at the tower outlet and the atmospheric pressure at the same elevation outside the shell is expressed by Du Preez and Kröger (1994) as:

$$p_{a6} - p_{a7} = (0.02\ Fr_D^{-1.5} - 0.14/Fr_D)(m_{av5}/A_6)^2/\rho_{av6} \tag{2.72}$$

where A_6 is the area of the cooling tower outlet. The densimetric Froude number is given by:

$$Fr_D = \frac{(m_{av5}/A_6)^2}{\rho_{av6}(\rho_{av7} - \rho_{av6})g d_6} \tag{2.73}$$

The value of ρ_{av6}, the density of the air-vapour mixture at the cooling tower outlet, is a function of p_{a6}, making the calculation of $p_{a6} - p_{a7}$ implicit. To perform the iterative solution of p_{a6}, Equation 2.72 is rearranged:

$$p_{a6} = p_{a7} + [0.02\ Fr_D^{-1.5} - 0.14/Fr_D](m_{av5}/A_6)^2/\rho_{av6} \tag{2.74}$$

In addition, Du Preez and Kröger (1994) found that a pressure loss is caused by distortions in the velocity profile and is expressed as:

$$\Delta p_\alpha = \alpha_{e6}(m_{av5}/A_6)^2(2\rho_{av6}) \tag{2.75}$$

with kinetic energy coefficient of the outlet $\alpha_{e6} \approx 1$ for hyperbolic cooling tower shells with horizontal heat exchangers or packing. Adding Equation 2.75 to Equation 2.72 yields:

$$p_{a6} - p_{a7} = (0.02\ Fr_D^{-1.5} - 0.14/Fr_D)(m_{av5}/A_6)^2/\rho_{av6} + \alpha_{e6}(m_{av5}/A_6)^2(2\rho_{av6}) \tag{2.76}$$

It is unclear why the pressure loss due to the velocity profile distortion is added by Kröger (2004) only after the iterative solution for p_{a6} in Equation 2.74 is found.

2.2.1.13 Pressure reduction due to elevation increase in atmospheric air

The atmospheric pressure decrease from ground level due to elevation change is expressed as:

$$\begin{aligned}\Delta p_{elevation} = p_{a1}\Big[1 - (1 - 0.00975 \\ \times H/T_{a1})^{3.5\ (1+w_1)\left(1-\frac{w_1}{w_1+0.62198}\right)}\Big]\end{aligned} \tag{2.77}$$

where H is the elevation above ground level, T_{a1} is the air temperature and w_1 the vapour fraction at ground level. Equation 2.77 is used to calculate the pressure reduction between ground level and the top of the tower due to elevation change, with $H = H_7$ and from ground level to the mean fill elevation, with $H = H_3 + L_{fi}/2$.

2.2.1.14 Draught equation solution

The total air-pressure reduction due to air-flow losses is expressed as a modification of Equation 2.32 at the fill location with the sum of all fill referred pressure loss factors:

$$\begin{aligned}\sum \Delta p_K &= (K_{ts} + K_{ct} + K_{rz} + K_{fs} + K_{ctc} + K_{fi} + K_{cte} + K_{sp} \\ &\quad + K_{wd} + K_{de})_{fi} \times (m_{av15}/A_{fr})^2/(2\rho_{av15}) \\ &= \sum K_{fi} \times (m_{av15}/A_{fr})^2/(2\rho_{av15})\end{aligned} \tag{2.78}$$

The draught equation is expressed as:

$$(p_{a1} - p_{a7}) = (p_{a1} - p_{a34}) + (p_{a34} - p_{a6}) + (p_{a6} - p_{a7}) + \sum \Delta p_K \tag{2.79}$$

Substituting Equation 2.77 with both $H = H7$ and $H = H3 + L_{fi}/2$ and Equations 2.68, 2.72 and 2.78 into Equation 2.79 and rearranging yields:

$$\begin{aligned}&p_{a1}[1 - (1 - 0.00975 \times H_6/T_{a1})^{3.5\ (1+w_1)\{1-\frac{w_1}{w_1+0.62198}\}}] \\ &- p_{a1}[1 - (1 - 0.00975\ (H_3 + L_{fi}/2)/T_{a1})^{3.5\ (1+w_1)\{1-\frac{w_1}{w_1+0.62198}\}}] \\ &- p_{a5}\Big[1 - \big(1 + \xi_{Ta5}(H_6 - H_3 - L_{fi}/2) \\ &/T_{a5}\big)^{-0.021233\ (1+w_5)/(\xi_{Ta5}(w_5+0.622))}\Big] \\ &- (0.02\ Fr_D^{-1.5} - 0.14/Fr_D)(m_{av5}/A_6)^2/\rho_{av6} \\ &= \sum K_{fi} \times (m_{av15}/A_{fr})^2/(2\rho_{av15}) + \alpha_{e6}(m_{av5}/A_6)^2(2\rho_{av6})\end{aligned} \tag{2.80}$$

Using Equation 2.77 and 2.78, the pressure at location 5 above the drift eliminators can be expressed as:

$$p_{a5} = p_{a1}\left[1 - 0.00975 \times \frac{H_3 + L_{fi}/2}{T_{a1}}\right]^{3.5\ (1+w_1)\left(1-\frac{w_1}{w_1+0.62198}\right)} - \sum K_{fi} \times (m_{av15}/A_{fr})^2/(2\rho_{av15}) \tag{2.81}$$

With the flow and fluid properties at location 15 being functions of p_{a5}, Equation 2.81 is implicit and is solved iteratively. Substituting Equation 2.81 into Equation 2.80, multiplying and simplifying yields the NDWCT draught equation:

$$\begin{aligned} & p_{a1}\Bigg[(1 - 0.00975\ (H_3 + L_{fi}/2)/T_{a1})^{3.5\ (1+w_1)\left(1-\frac{w_1}{w_1+0.62198}\right)} \\ & \times \left(1 + \xi_{Ta5}(H_6 - H_3 - L_{fi}/2)/T_{a5}\right)^{-0.021233\ (1+w_5)/(\xi_{Ta5}(w_5+0.622))} \\ & - (1 - 0.00975\ H_6/T_{a1})^{3.5\ (1+w_1)\left(1-\frac{w_1}{w_1+0.62198}\right)}\Bigg] \\ & - (0.02Fr_D^{-1.5} - 0.14/Fr_D)(m_{av5}/A_6)^2/\rho_{av6} \\ & = \left[\sum K_{fi} \times (m_{av15}/A_{fr})^2/(2\rho_{av15})\right] \\ & \times \left(1 + \xi_{Ta5}(H_6 - H_3 - L_{fi}/2)/T_{a5}\right)^{-0.021233\ (1+w_5)/(\xi_{Ta5}(w_5+0.622))} \\ & + \alpha_{e6}(m_{av5}/A_6)^2/(2\rho_{av6}) \end{aligned} \tag{2.82}$$

Equation 2.82 is balanced by solving for the mean air-vapour mixture mass flow rate between locations 1 and 5, m_{av15}.

2.2.2 The transfer equation

The transfer equation states that the Merkel number of the NDWCT is equal to the sum of the Merkel numbers of the rain zone, fill and spray zone:

$$Me_{NDWCT} = Me_{rz} + Me_{fi} + Me_{sp} \tag{2.83}$$

The NDWCT Merkel number (Me_{NDWCT}) is calculated using Equation 2.31. The methods for calculating the values of the three heat and mass transfer zone Merkel numbers are shown below in Section 2.2.2.1 to 2.2.2.3. The transfer equation is balanced by solving for the NDWCT T_{wo}.

2.2.2.1 Rain zone Merkel number

The Merkel number for the rain zone is expressed as:

$$\begin{aligned} Me_{rz} = 12 &\left(\frac{D_1}{v_{av3} d_d}\right)\left(\frac{H_3}{d_d}\right)\left(\frac{p_{a1}}{R_v T_{a1} \rho_{wo}}\right) Sc_1^{0.33} \\ &\times \left[\ln\left(\frac{w_{s1}+0.622}{w_1+0.622}\right)/(w_{s1}-w_1)\right] \\ &\times \Bigg[0.90757\ a_\rho \rho_{av1} - 30341.04\ a_\mu \mu_{av1} - 0.37564 \\ &+ 4.04016\ \Big[\Big(0.55 + 41.7215\ (a_L d_d)^{0.80043}\Big) \\ &\times \Big(0.713 + 3.741\ (a_L H_3)^{-1.23456}\Big)\Big(3.11 e^{0.15\ a_v v_{av3}} - 3.13\Big) \\ &\times \Big(e^{(5.3759\ e^{-0.2092\ a_L H_3})\ln(0.3719\ e^{0.0019055\ a_L d_3}+0.55)}\Big)\Big]\Bigg] \end{aligned} \tag{2.84}$$

with the same applicability ranges as Equation 2.43. The specific gas constant for water vapour is $R_v = 461.52$ J/kgK and the Schmidt number at location 1 is calculated using:

$$Sc_1 = \mu_{av1}/(\rho_{av1} D_1) \tag{2.85}$$

with the diffusion coefficient in gases is expressed by Gilliland (1934) as:

$$D_1 = \frac{0.04357\ T_{a1}^{1.5}\left(\frac{1}{M_a}+\frac{1}{M_v}\right)^{0.5}}{p_{abs}\left(V_a^{0.333}+V_v^{0.333}\right)^2}\ \text{m}^2/\text{s} \tag{2.86}$$

with molecular masses $M_a = 28.97$ g/mol and $M_v = 18.016$ g/mol and molecular volumes $V_a = 29.9$ m^3/mol and $V_v = 18.8$ m^3/mol.

2.2.2.2 Fill Merkel number

The fill Merkel number is dependent on the fill as well as its operating conditions. It is usually expressed as a function of both G_w and G_a for a specific fill design, with the function taking one of many different forms. Like with the fill pressure loss factor, the characteristic equations of fill Merkel numbers are obtained experimentally. A common expression provided by Kröger (2004) is:

$$Me_{fi} = a L_{fi} G_w^b G_a^c \tag{2.87}$$

with the coefficients a, b and c being determined experimentally as part of a test program. Kloppers (2003) determined that the water inlet temperature and fill height must be taken into account and proposed the following equation:

$$Me_{fi} = a G_w^b G_a^c L_{fi}^d T_{wi}^e \tag{2.88}$$

with the coefficients a through e being determined experimentally.

2.2.2.3 Spray zone Merkel number

The Merkel number of the spray zone is determined with the following empirical equation from testing data by Lowe and Christie (1961):

$$Me_{sp} = 0.2\ L_{sp}\left(\frac{G_a}{G_w}\right)^{0.5} \tag{2.89}$$

where L_{sp} denotes the height of the spray zone.

2.2.3 The energy equation

The energy equation states that the enthalpy gain of the air stream, as it moves through the cooling tower from the inlet (1) to the top of the drift eliminators (5), is equal to the enthalpy loss by the cooling water between its inlet (wi) and outlet (wo):

$$Q_{NDWCT} = m_a(i_{ma5} - i_{ma1}) = m_w c_{pwm}(T_{wi} - T_{wo}) \tag{2.90}$$

This equation is balanced by solving for the outlet air temperature above the drift eliminators (T_{a5}).

2.3 Heat rate correction

Annual NDWCT performance prediction calculations are performed by Kröger (2004) to calculate the total annual power output of a wet-cooled Rankine cycle using annual weather data. A NDWCT performance calculation is performed for each entry of the tabulated annual wet-bulb temperature, dry-bulb temperature and operating hours (see the first columns of Table F.3) of the power plant under consideration. The rate of heat rejection by the SSC and the power output of the plant are presented as functions of the SSC water inlet temperature (which is equal to the NDWCT T_{wo} with heat losses in the connecting pipework neglected). The operating point of the NDWCT, for each weather data entry, is then determined iteratively as the NDWCT T_{wi} where the Q_{NDWCT} according to Equation 2.90 matches the SSC heat rejection rate (function of NDWCT T_{wo}). The annual power output is calculated as the sum (weighted by operating hours) of the power outputs (function of the iteratively calculated SSC water inlet temperature) of the weather data entries.

A variation of this method is the use of heat rate corrections which quantify the primary cycle efficiency change, due to SSC water inlet temperature change, introduced in Section 1.1. The heat rate is the energy input (kJ) required to generate one kilowatt-hour of electricity, and the heat rat correction (C_{HR}) is the percentage change from some base heat rate (HR_B) at a certain SSC water inlet temperature. Heat rate corrections may be presented graphically, such as the "heat-rate correction curve" in Figure 2.3.

The heat rate at a specific NDWCT T_{wo} is calculated as:

$$HR(T_{wo}) = HR_B\ \left(100 + C_{HR}(T_{wo})\right)/100 \tag{2.91}$$

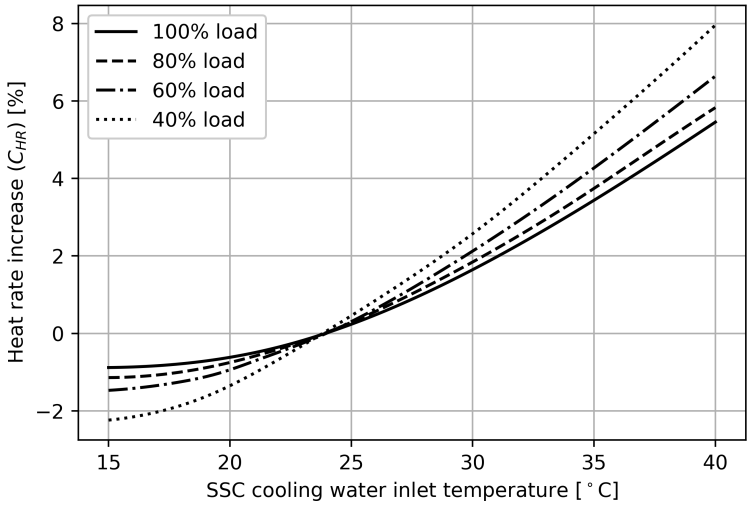

Figure 2.3: Heat rate correction curves for SSC water inlet temperatures at various loads for an Eskom power plant

The rate of heat rejection by the NDWCT is the difference between the heat input by the boiler (Q_{boiler}) and the electricity generated (P), assuming no losses in the generator:

$$\begin{aligned} Q_{NDWCT} &= Q_{boiler} - P = P \times HR\big(T_{wo}\big)/3600 - P \\ &= P\big(HR(T_{wo})/3600 - 1\big) \end{aligned} \tag{2.92}$$

As with the power output calculations in Kröger (2004), the operating point is determined iteratively as the NDWCT T_{wi} where the Q_{NDWCT} according to Equation 2.90 matches Q_{NDWCT} according to Equation 2.92. With the operating point, and thus also the heat rate, known for every weather data entry, the annual power plant energy input can be calculated as the sum (weighted by operating hours) of the energy inputs, if the expected electrical outputs are known, ultimately enabling calculation of the lifecycle energy input of a power plant.

Kröger (2004) proposes the consideration of the long-term effects of the fouling characteristics of competing NDWCT fills in the process of fill selection, as fouling can have significant effects on the plant operating costs. Kröger (2004) does not provide methods for quantification of fill fouling effects.

Chapter 3: NDWCT fill fouling literature study

This chapter provides a review of the relevant literature on NDWCT fill fouling. It discusses the formation, growth and natural removal processes as well as the factors which influence the accumulation of the three types of fill fouling listed by Mirsky and Monjoie (1991): scale, biological fouling and suspended solid deposition. After this, the effects of combined fouling of multiple types is discussed, followed by fill fouling control methods and fouling quantification methods.

3.1 Scale

Scale is defined as deposited salts formed by crystallisation and is commonly found on heat exchanger surfaces where aqueous solutions, such as natural water, are in use (Bott, 1995). The main scaling salts found in NDWCTs, according to Monjoie (2009), are calcium carbonate ($CaCO_3$) and calcium sulphate ($CaSO_4$).

3.1.1 Formation and growth

The crystallisation process of a dissolved salt in an aqueous solution is described according to Bott (1995). It consists of three stages: supersaturation, nucleation and crystal growth. Supersaturation is a concentration of the dissolved salt greater than the solubility limit of the salt at a specific temperature. In evaporative cooling towers, the concentration of dissolved salts is increased by the evaporation of water. Nucleation is the formation of micro-crystals, called crystallites, in the supersaturated solution. Initially, crystallites form at nucleation sites on surfaces or on impurities in the solution; this process is called primary nucleation. More crystallites form near the existing crystallites and this is called secondary nucleation. After the formation of stable crystallites, individual crystals grow in the supersaturated solution. Different theories are presented on the crystal growth process, but it may be described as a diffusive mass transfer process governed by the following equation:

$$\frac{dM_c}{dt} = K_G A (c_b - c_e)^n \tag{3.1}$$

where M_c represents crystal mass, K_G is the crystal growth coefficient, A is the surface area of the crystal, c_b is the bulk fluid concentration of the salt, c_e is the equilibrium saturation concentration of the salt at the crystal face and the integer n is the "order" of the process. The values of K_G and n are dependent on the exact crystallisation process.

Figure 3.1a shows scale formed on flat asbestos cement fill sheets. The scale deposits form as sheets of approximately uniform local thickness across the

asbestos fill surface. Figure 3.1b shows scale on splash fill, a fill type that is considered highly resistant to fouling (see Section 1.3.2.1). Here scale forms as stacked crystals with jagged edges.

(a) Asbestos cement fill with severe scaling (Augustyn *et al.*, 2018)

(b) Scaling on splash fill

Figure 3.1: Scaling on different fill types

3.1.2 Natural removal or growth inhibition

No mechanism was found that naturally inhibits the progress of fill scaling as long as supersaturated concentrations of salts and nucleation sites exits. As seen in Figure 3.1a, relatively large areas of scale may become detached from the fill surface due to the increased mass of the scale overcoming the strength of the bond with the fill surface.

3.1.3 Influencing factors

The influencing factors of NDWCT fill scaling according to Aull (2013) are cycles of concentration being too high or incorrect treatment of the make-up water (see Section 3.5.1.1), both leading to high concentrations of dissolved solids. Whittemore and Massey (1992), Monjoie (2009) and Aull (2013) state that areas of low water flow, caused by poor water distribution, have increased likelihood of scale formation.

3.2 Biological fouling

Biological fouling of NDWCT fills consists of micro-organism attachment and growth on fill surfaces. The details of biological fouling in the following sub-sections are obtained from Characklis and Marshall (1990), unless otherwise stated.

3.2.1 Formation and growth

Three types of biological fouling are associated with NDWCT fills: bacterial, algal and fungal, although fungal fouling only affects wooden fills, which are not considered in this study. Biological fouling is usually present on fills as

a "biofilm" (Zaorski and Miller, 2017), which is defined as "cells immobilized at a substratum and frequently embedded in an organic polymer matrix of microbial origin". Formation of biofilm on fill surfaces is described similarly by Characklis and Marshall (1990) and Zaorski and Miller (2017) and consists of the following steps:

(i) The fill is initially clean of any contaminants. In the case of polypropylene and polyvinyl chloride (PVC) fills, they are initially hydrophobic, resulting in reduced thermal performance.

(ii) Organic molecules in the flowing water become attached to the fill surface to "condition" it (also known as "aging" of the fill), shown in Figure 3.2a.

(iii) Individually floating (planktonic) microbial cells in the flowing water impact the fill surface (see Figure 3.2b) where some become weakly and temporarily attached (adsorped) and are then removed by shear forces (desorped), known as reversible adsorption. A small number of the reversibly adsorped cells become irreversibly adsorped after remaining adsorped for a certain critical time.

(iv) The adsorped cells grow on the surface, obtaining nutrition from the flowing water.

(v) The cells excrete substances including extracellular polymeric substances (EPS) which acts as a glue, keeping the structure of the biofilm intact.

(vi) Additional cells and inorganic matter become attached to the biofilm, increasing its size and mass.

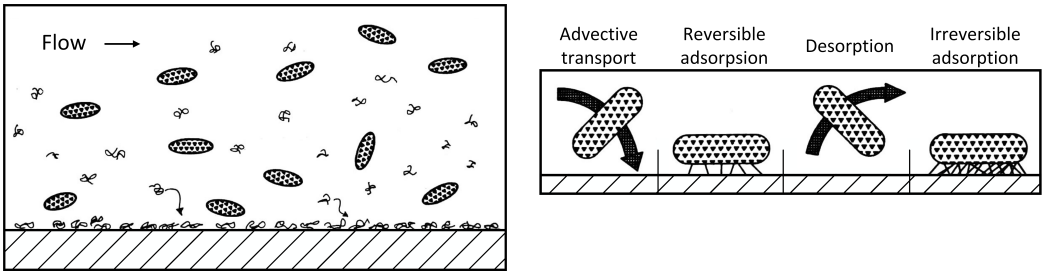

(a) Conditioning of the fill surface with organic molecules

(b) Reversible and irreversible adsorption of microbial cells

Figure 3.2: Biological fouling processes (Characklis and Marshall, 1990)

3.2.2 Natural removal or growth inhibition

Natural removal or detachment of the biofilm can be as a result of erosion or sloughing. Erosion is the loss of small amounts of the biofilm due to shear

forces, while sloughing is the loss of large amounts of biofilm at a time. Sloughing is more prevalent in thick biofilms with nutrient-rich flow and may be initiated by oxygen starvation or, according to Bott (1995), nutrient starvation causing layers near the surface to die, leading to reduced adhesion capability.

The rate of growth of a biofilm is characterised as having an induction phase with slow growth, a log accumulation phase with rapid mass increase and a plateauing phase where approximately equal growth and removal rates, with stable biofilm thickness, are reached. The entire growth period is represented with a sigmoidal curve as shown in Figure 3.3.

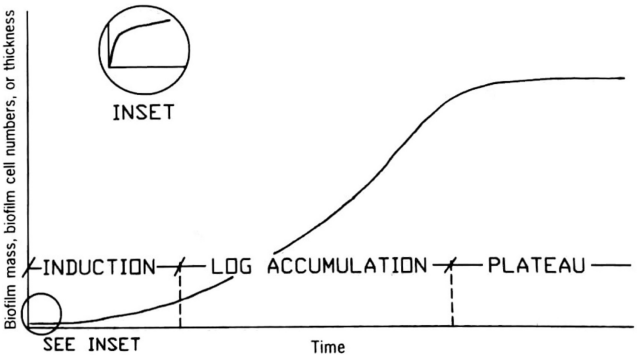

Figure 3.3: Biological growth usually follows a sigmoidal curve (Characklis and Marshall, 1990)

3.2.3 Influencing factors

Increased roughness of the fill surface leads to greater biofilm growth due to a greater surface area and greater protection of microbrial cells from shear forces. Water quality factors which affect biological fouling accumulation include the availability of organic carbon and other nutrients, which provide energy for microbial growth, and inorganic particles, which get stuck in the biofilm structure and add mass.

Biological processes in biofilms tend to increase in rate at higher temperatures between 15 °C and 40 °C, with a marked decrease at 45 °C (these temperature ranges are applicable to NDWCTs). The change in microbial growth rate is highly sensitive to temperature when the biofilm is nutrient-saturated.

At very low water flow velocities, the biofilm accumulation rate is limited by nutrient supply to the biofilm and thus, increased velocity increases the biofilm accumulation. At high velocities, however, the biofilm growth accumulation is limited by the detachment rate and increased velocity reduces the accumulation rate. No indication is provided on what constitutes low and high water flow velocities in NDWCT fills.

Biological factors have a significant effect on the rate of biofilm accumulation. This includes the specific microbial communities present, as well as their inter-

dependent interactions, which may range from no interaction, to cooperation, to parasitism or a mixture of these interactions.

3.3 Suspended solid deposition

Suspended solid deposition or particulate deposition (see Figure 3.4) on NDWCT fill occurs when entrained particles in the cooling water such as silt, mud, ash, metallic corrosion products or other particles settle on the fill surfaces. According to Bott (1995), the deposition of both detached scale products (crystals) and micro-organisms responsible for biological fouling may also be treated as particulate deposition. The details of suspended solid deposition in the following subsections are obtained from Bott (1995), unless otherwise stated.

3.3.1 Formation and growth

Suspended solid formation and growth is expressed as the difference between the deposition and removal rates:

$$\frac{dM_{ss}}{dt} = \phi_D - \phi_R \tag{3.2}$$

where M_{ss} is the suspended solid mass, ϕ_D is the deposition rate and ϕ_R is the removal rate. Two steps are required for a suspended particle to be deposited on the fill surface: firstly, the particle must be transported to the surface by either Brownian motion (very small particles), turbulent diffusion or momentum (very large particles) and, secondly, the particle must stick to the surface.

A complex set of theoretical models for heat exchanger particle deposition are presented, although these only partly describe the mass transfer to the surface, since values of many of the variables required for deposition quantification are unknown. Greater reliance is placed on empirical data, where it is available. A simple quantification of the particulate deposition rate is:

$$\phi_D = K_t c_b P \tag{3.3}$$

where K_t is a transport coefficient for the case where all particles stick to the surface, c_b is the particle concentration in the bulk fluid and P is the "sticking probability" which has a value $0 \leq P \leq 1$. The values for both K_t and P are empirically determined, but they are known to vary depending on the surface condition, which changes as fouling progresses.

3.3.2 Natural removal or growth inhibition

While the suspended solid removal rate (ϕ_R) is not quantified in Bott (1995), the mechanism of removal is explained as follows. Bulk fluid velocity generates shear force in the viscous sublayer of a turbulent fluid flow near a wall. Pure shear forces would only tend to drag particles along the surface, without removing them from the surface. Cleaver and Yates (1973) proposes a mechanism consisting of unsteady "turbulent bursts" which generate lift, acting to

remove particles from the viscous sublayer and entrain them into the turbulent flow. The frequency of the turbulent bursts increases with increased wall shear stress and thus bulk fluid velocity. The strength of turbulent bursts are dependent on both the flow velocity and geometry.

3.3.3 Influencing factors

Both the deposition and removal rates of suspended solids are influenced by flow geometry, velocity and surface condition. Monjoie (2009) states that the deposition rate is influenced by the suspended solids concentration and that smaller particles, such as those in clays, are deposited more easily.

According to Mortensen and Michell (2013), exposure to silt alone can not cause detrimental blockage of fills; biological growth is a requirement. Similarly Gill *et al.* (1994) states that silt alone can only be responsible for small amounts of fouling. According to Zaorski and Miller (2017), biological growth acts as a "glue", which captures solid particles in the flow. Consequently, the presence of biological fouling is a major influencing factor on the growth of suspended solid deposition fouling.

Despite these claims, at the cooling towers mentioned in Du Preez (2018), extremely high concentrations of suspended solids in the cooling water, combined with poor fill design, has caused significant suspended solid deposition without the presence of scale or biological fouling (see Figure 3.4b). The asbestos cement fill in this case is arranged with different layers crossing each other at 90° angles, creating millions of contact points where the water flow stagnates and suspended solid deposition is initiated.

(a) Mud on film fill (Mortensen and Michell, 2013)

(b) Extreme fouling of asbestos cement fill (Augustyn *et al.*, 2018)

Figure 3.4: Suspended solid deposition

3.4 Combined fouling types

The combination of fouling types appears to be important given that numerous sources, including Monjoie *et al.* (1993), Gill *et al.* (1994) and Mortensen and

Michell (2013), consider the most severe cases of fouling to be those where suspended solids are captured by biological fouling. A study of fouling in operational cooling towers by Gill *et al.* (1994) found that biological growth and silt deposition were present in the fills of the majority (95% of over 30) of cooling towers investigated. In the remaining 5% of locations, scale was also present. Analysis of fouling solids in a NDWCT fill by Mortensen and Michell (2013) found 10% biological matter and 90% inorganic matter by mass.

The combination of scale and suspended solid deposition was also reported by Augustyn (2019) in a testing sample of film fill installed in a NDWCT. In this case the film fill surface was extensively scaled and the flutes were completely blocked and filled with solid particles, as shown in Figure 3.5.

Figure 3.5: Film fill with both scaling and suspended solid deposition (Augustyn, 2019)

3.5 Fill fouling control

3.5.1 Prevention

3.5.1.1 Cooling water quality and treatment

Water lost from the cooling cycle, through evaporation, drift, leakage and blowdown (the controlled release of water from the cooling cycle when the cooling water quality measurements increase to pre-set levels), is replaced by make-up water. This make-up water is obtained from natural sources such as the ocean, rivers or dams and may include mud, silt and dissolved solids (Aull, 2013). Furthermore, airborne particles including dust, soil, pollen, bacteria and plant material may be scrubbed from the air entering the cooling tower shell by the dense water shower in the lower parts of the NDWCT (DiFilippo and Maulbetsch, 2003).

The cycles of concentration (COC) is defined by Bott (1995) as the ratio of dissolved salts concentration in blowdown water to dissolved salts concentra-

tion in make-up water and has a typical value of 3 to 5. Cooling water quality may be improved by increasing the blowdown rate, thus allowing more make-up water into the system and reducing the COC and concentration of fouling contaminants in the cooling water. The amount of blowdown may be limited by environmental legislation or the cost of water (Monjoie, 2009).

Cooling water is usually treated to remain within specific chemical parameter limits, with the treatment schemes being dependent on the quality of the natural water used and the specific power plant requirements. In Eskom, cooling water treatment usually consists of softening, followed by one or more clarification steps. Softening consists of the removal of calcium and magnesium ions by the addition of softening agents such as lime or soda ash (DiFilippo and Maulbetsch, 2003). Clarification is performed by keeping the water stationary for a pre-set period of time in a vessel known as a clarifier. A coagulation agent is added and suspended solids settle to the bottom of the clarifier, forming a sediment which can be removed (Department Of water affairs and forestry, 1996). Cooling water treatment may either be performed as a side-stream, where a portion of the water is continuously fed to the treatment plant and returned to the cooling cycle, or the entire make-up flow is treated before being admitted to the cooling cycle. Biological fouling is controlled by dosing the cooling water with a mixture of biocides, which kill micro-organisms, and biostats, which inhibit their growth (Govender, 2017).

3.5.1.2 Fill selection

As mentioned in Section 1.3.2 and in sources such as Monjoie (2009) and Zaorski and Miller (2017), different fill types, subtypes and designs have different general fouling tendencies. Puckorius (2013) indicates fill fouling potential, along with thermal performance, as one of the main criteria when making a fill selection. Monjoie (2009) specifically proposes the use of very low scaling fill where fouling is expected, including for the replacement of fouled fills.

3.5.1.3 Other methods

Both Aull (2013) and Monjoie (2009) stress the importance of uniform water distribution to avoid fouling. Blocked or broken cooling water sprayers need to be replaced regularly.

Concrete weirs, as described in Augustyn (2017), may be installed in the NDWCT pond near the cooling water outlet (see Figure 3.6a) to prevent sludges of suspended solids from exiting the pond and ultimately returning to the cooling tower and being sprayed onto the fill. Sludge and other debris collected behind these weirs are removed when the pond is cleaned during outages.

3.5.2 Removal

Gill *et al.* (1994) reports on several previous studies from the early 1990s which show that cleaning of fouled fill has very little success in the long term.

Gill *et al.* (1994) also refers to a study showing that biocides do not remove biofilm, even though they kill the bacterial cells in it. Dahm *et al.* (2015) states that cleaning of film fill at an operational power plant did improve the NDWCT thermal performance, but that this effect did not last and the performance degraded again to the levels before cleaning in approximately one year. Monjoie *et al.* (1993) witnessed an increase in fill thermal performance after a fill test section was completely dried out, however, like other types of fill removal, this improvement was only temporary.

The use of high-pressure water to clean asbestos cement fill (see Figure 3.6b) is in use at Eskom power stations (Du Preez, 2018). Thermal performance benefits from these activities are minor and short-term.

(a) Concrete weir installed in a NDWCT (Augustyn, 2017)

(b) Cleaning of asbestos cement fill with high-pressure water (Augustyn, 2019)

Figure 3.6: Fouling control measures

3.6 Fill fouling quantification

Fill fouling has been traditionally quantified using mass gain and/or performance change. While the literature usually provides details on the experimental setups utilised and their mass measurement techniques, there is no detailed information on how performance changes were calculated.

3.6.1 By mass gain

Gill *et al.* (1994) investigated the fouling characteristics of small (approximately 75 cm diameter and 50 cm deep) fill samples by adding fouling contaminants such as clay and bacteria. The daily fouling mass gains were recorded and the biological deposits were quantified using a biofilm heterotrophic plate count procedure.

Both Mirsky and Monjoie (1991) and Whittemore and Massey (1992) conducted long-term testing of various fills using cooling water at operational power plants. Mass gain was monitored periodically during these tests and all fills indicated mass gain, although wide variation was observed (see Figure 3.7).

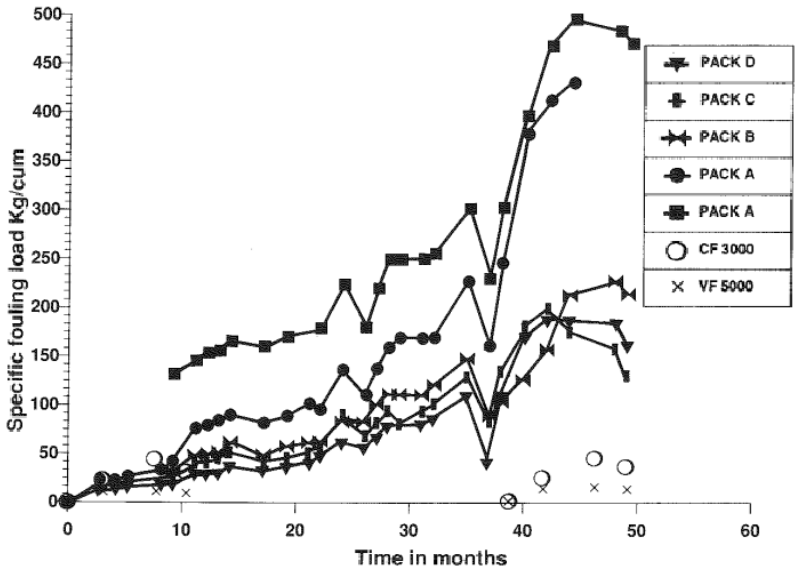

Figure 3.7: Fouling mass gain of various fills (Whittemore and Massey, 1992)

Mortensen and Michell (2013) states that fouling mass accumulation of 12 - 20 lb/ft^3 (192 - 320 kg/m^3) leads to thermal performance degradation. Troncin (2012) tested the thermal performance (as new) and the fouling mass gain of several fills. A graphical method was proposed to identify the best fill, although it was mentioned that the method needs to be combined with economic factors and is not sufficient on its own.

Monjoie *et al.* (1993) proposes the calculation of an average mass gain per day during the fill fouling test period and comparing this to a set criteria for an acceptable fouling limit. A certain NDWCT user mentioned put a maximum limit of 0.1 kg/m^3 per day on the mass gain for fills to be used in its NDWCTs. However, the same source states that different fills have different relations between mass gain and thermal and hydraulic performance.

3.6.2 By inspection

Mortensen and Michell (2013) developed a visual film fill inspection method. It consists of visual inspection of exposed (top or bottom) fill layers as well as manual insertion of probes into the fill and judging the fouling intensity by the difficulty of passing the probe through the fill layers. This method is useful where it is not possible to remove fill layers to visually inspect the inner layers of the fill.

The assessments include estimations of the accumulated fouling mass per unit volume of fill. This clearly requires significant experience by the assessor while providing no direct indication of changes in fill performance.

3.6.3 By performance change

Mirsky and Monjoie (1991) and Whittemore and Massey (1992) performed

fill performance measurements periodically during extended test periods of 19 and 50 months respectively, during which fouling occurred. Both sources report the change in fill thermal performance (Merkel number) and hydraulic performance (pressure loss) as well as calculated changes in NDWCT recooled temperature. Performance changes were also graphically related to mass gain (see Figure 3.8). It is unknown whether the performance tests for these studies were performed at single or multiple operating points, making it difficult to understand whether the changes apply generally across the operating ranges of water- and air-flow rates. Reported changes in NDWCT recooled temperature due to fouling would only apply to the specific cooling towers considered.

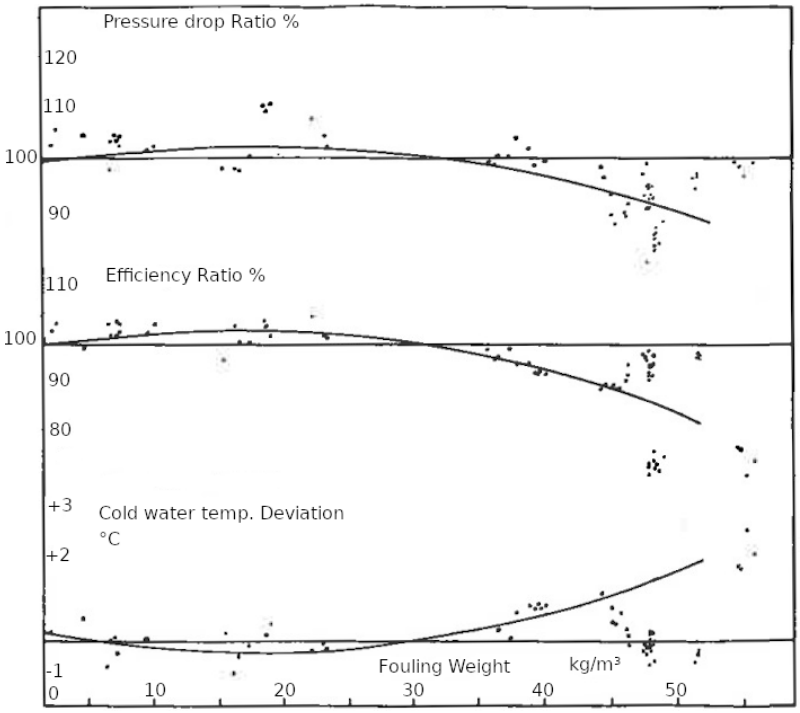

Figure 3.8: Change in the fill performance as a function of fouling mass gain (adapted from Mirsky and Monjoie (1991))

Zaorski and Miller (2017) improved on the aforementioned studies somewhat, reporting the changes in the thermal and hydraulic performance of several fills across a range of water- and air-flow rates. This data can be directly used for NDWCT performance prediction calculations. The test period was quite limited at 21 weeks and the performance data was only reported for the start (clean) and end (fouled) of the test period, meaning that transient calculations can not be performed.

3.7 Conclusion

NDWCT fill fouling may consist of one or more of scale, biological fouling and suspended solid deposition. Fouling accumulation is dependent on a multitude

of factors, many of which are difficult or impossible to quantify. The factors relate to the operating environment, cooling water and the cooling tower and fill designs. Fill fouling is therefore considered to be location-specific.

Fill fouling performance may be determined by a combination of observed mass gain, physical inspection and expected performance changes, although no standard methodologies for any of these exist. In order to estimate the fill fouling performance of competing fills for selection for installation in a NDWCT, it is deemed appropriate to perform long-term testing of fill samples, with the fill performance being quantified periodically while replicating the fills' operating conditions as closely as possible.

Chapter 4: Fill performance testing

4.1 Introduction

This chapter provides a description of the Eskom fill fouling test facility and the methods used to calculate the required fill performance test results for use in NDWCT performance prediction calculations. An example calculation of the fill performance characteristic equations is provided in Appendix C, while Appendix D provides an example of NDWCT performance prediction using the generated fill performance characteristic equations.

The test facility was designed, manufactured and is operated by an Eskom contractor. The design, manufacture and results of the first few weeks of testing are detailed in Kotze (2019). The candidate had no input on the design or manufacture, although he did have input on the testing process (required flow rates, timing, frequency and duration) for the periodic fill performance tests. The test facility is designed to calculate instantaneous results (G_w, G_a, Me_{fi} and K_{fd}) for monitoring and control purposes. These calculations follow the fill performance calculation method from Kröger (2004), but includes additional calculations required for the specific test facility layout. This study follows the same result calculation methods for fill performance analysis. The performance test data selection and result calculation were performed independently of the contractor, although the result calculation was verified against those calculated by the test facility. The contractor provided no input to the result corrections or regressions in the current chapter or to any work in subsequent chapters.

4.2 Fill fouling test facility

4.2.1 Purpose and general layout

The fill fouling test facility (see Figure 4.1) was procured by Eskom to better understand the long-term effects of NDWCT fill fouling. It is designed to expose fill samples to conditions closely replicating NDWCT operating conditions for months or years, while periodically measuring the mass gain and thermal and hydraulic performance of the fill samples. The facility consists of four identical mechanical draught counterflow test cooling towers, called test sections, as well as walkways, ladders and access doors for maintenance, fill inspections and fill replacement. It is designed largely using stainless steel components and PVC piping to ensure good long-term operation.

Hot water from an elevated inlet duct in the main NDWCT is fed to the facility by gravity and is split to the four test sections. Cooled water exiting the test sections is collected and drains to the cooling tower pond, also by gravity.

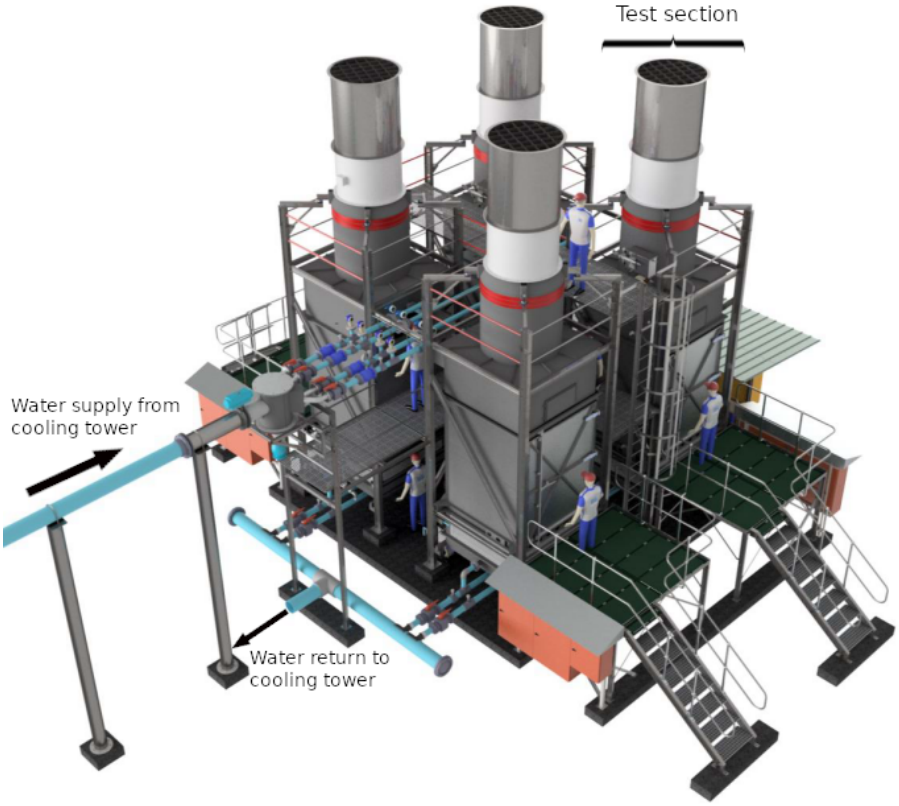

Figure 4.1: Eskom fill fouling test facility (Kotze, 2019)

The test facility is designed for autonomous operation through the use of a PLC (programmable logic controller), allowing control, monitoring and remote manual intervention through an internet connection. Testing started in April 2019 with a different fill sample, selected by Eskom, installed in each test section. Testing was temporarily suspended in January 2020.

4.2.2 Test section layout

Each of the four test sections (see Figure 4.2) consists of a enclosed space to install a fill sample of 1.5 m by 1.5 m horizontal cross-section and up to 2 m in height. The fill sample is installed through a large access door covering one entire side of the test section.

Water enters the test section above the fill sample, is sprayed onto the top of the sample using four sprayers with square spray patterns (see Figure 4.3) and flows downwards through the sample. Below the sample, the water rains down into a collection sump from where it is routed to the common drain pipe. The water flow rate into each test tower is controlled by a pneumatic pinch valve in the inlet piping.

Air-flow (draught) is provided by an electrically-powered fan at the test section outlet (top) to replicate the natural draught of a NDWCT. Air is drawn

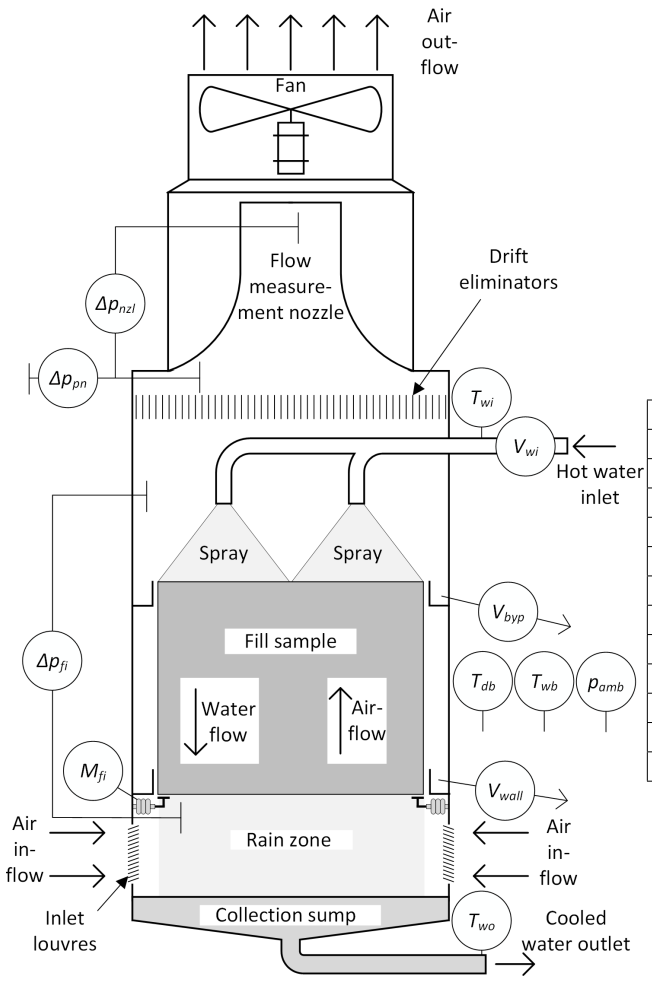

Sym.	Measurement
V_{wi}	Water inlet volume flow
Δp_{pnz}	Pre-nozzle pressure difference
Δp_{nzl}	Nozzle pressure difference
Δp_{fi}	Fill pressure difference
T_{wi}	Water inlet temperature
T_{wo}	Water outlet temperature
T_{db}	Dry-bulb air temperature
T_{wb}	Wet-bulb air temperature
V_{wall}	Wall water volume flow
V_{byp}	Bypass water volume flow
p_a	Ambient pressure
M_{fi}	Fill mass

Figure 4.2: Layout of a single test section (adapted from Kotze (2019))

through the inlets located on all four sides of the test section, below the fill sample. Louvres (see Figure 4.4) cover the air inlets to provide an even air-flow distribution and reduce the amount of water lost due to splashing. Air enters the rain zone near horizontally and turns upwards, resulting in a cross-counterflow rain zone, to travel through the fill sample and sprayed water. Above the sprayers, drift eliminators remove droplets entrained in the air-flow. An air-flow measurement nozzle is located above the drift eliminators. The air-flow rate is controlled by manipulating the fan speed.

4.2.3 Measurement equipment

The details of the measurement equipment used at the fill fouling test facility are described below. The implication of the equipment uncertainty details, where provided, is discussed in Chapter 5. All uncertainty information is obtained from published equipment documentation. Unless otherwise mentioned, published accuracy or uncertainty values are assumed, as in ASME (2014), to be at the 95% confidence level with infinite degrees of freedom (see Section

Figure 4.3: Sprayer assembly viewed from below (courtesy of TF Design)

Figure 4.4: Inlet louvres

5.2.5). Since equipment uncertainties are frequently supplied (or are assumed to be supplied) at the 95% confidence level, the calculation is divided by 2 to obtain the standard (68%) uncertainty. Unless another confidence interval is provided, this is done without further mention in the following sections.

4.2.3.1 Data capture and control

The test facility data capture and control system has a single central Siemens S7-1200 CPU 1214C DC/DC/DC PLC with a SM 1231 AI 4 16 bit module. This analogue input module receives the input signals from the equipment that is common to all test sections, including the wind speed and direction (used for monitoring only) and the ambient pressure measurement (p_a). All control functions are performed by the central PLC, including the air- and water flow rates using PID (proportional, integral, derivative) control.

Each of the four test sections is served by a Siemens SIMATIC ET200SP Distributed I/O (input/output) system. Each I/O system has two AI 8XL 2-/4-wire analogue input modules, with four analogue inputs each, receiving signals from the respective test section's measurement equipment. All measurement signals to the analogue input modules are $4 - 20$ mA signals which are either supplied directly by the instrument or are converted to $4 - 20$ mA signals by intermediate components. The I/O system digitises each analogue signal it receives to one of 27649 digital values, with this digital data then being sent, via cable, to the central PLC for processing and storage.

The maximum current error of the inputs to the I/O system serving each test section is 0.5% of the 4-20 mA range (r_{sig}) according to Siemens AG (2015). This uncertainty is calculated using:

$$b_{IO} = [0.5\% \times r_{sig}]\,/2 \tag{4.1}$$

The uncertainty of the digitisation is equal to the resolution of the 27648 intervals in the 4-20 mA range. This digitisation is considered independent

of the confidence level since the same error is always expected, no matter the sample size of input analogue values provided to the digitization process:

$$b_{digi} = r_{sig}/27648 \tag{4.2}$$

The accuracy of the analogue input module on the central PLC, to which the ambient pressure measurement is connected, is 0.3% of the full range, according to Siemens AG (2012):

$$b_{PLC} = [0.3\% \times r_{sig}]\,/2 \tag{4.3}$$

The digitisation uncertainty of the central PLC is also calculated using Equation 4.2.

4.2.3.2 Inlet water flow rate

The inlet water flow rate (V_{wi}) of each test section is measured by an Endress + Hauser Promag 10D 3" electromagnetic flow meter installed after the flow control valve. The output range of the instrument is 0 m^3/hr at 4 mA and 45 m^3/hr at 20 mA.

The instrument uncertainty is stated by Endress + Hauser (undated *a*) as 0.5% of the reading + 2 mm/s. The inside diameter of the instrument is 0.076 m. The instrument uncertainty is converted to m^3/hr:

$$\begin{aligned} b_{V_{wi_{instr}}} &= [0.5\ \% \times \text{value} + 2\ \text{mm/s}]\,/2 \\ &= \left[0.005 \times V_{wi} + 2\ \text{mm/s} \times \frac{3600\ \text{s}}{1\ \text{hr}} \times \frac{1\ \text{m}}{1000\ \text{mm}}\right. \\ &\quad \left. \times\ (0.076\ \text{m})^2\right]/2 \\ &= [0.005 \times V_{wi} + 0.0416]\,/2\ \text{m}^3/\text{hr} \end{aligned} \tag{4.4}$$

There is an additional uncertainty on the instrument's current output of 5 μA, with the resulting uncertainty calculated as:

$$\begin{aligned} b_{V_{wi_{curr}}} &= \left[\frac{5\ \mu\text{A}}{20\ \text{mA} - 4\ \text{mA}} \times (45\ \text{m}^3/\text{hr} - 0\ \text{m}^3/\text{hr})\right]/2 \\ &= 0.00703\ \text{m}^3/\text{hr} \end{aligned} \tag{4.5}$$

4.2.3.3 Air-pressure difference measurement

Three air-pressure differences are measured, each using a single Endress + Hauser Deltabar S PMD75 sensor. This sensor provides a $4 - 20$ mA output, with a maximum range of -1000 Pa to 1000 Pa and has been turned down to a range of -500 Pa to 100 Pa.

The fill pressure difference (Δp_{fi}), measured between the spaces below and above the fill sample, make use of static H-taps (see Figure 4.5), similar to those used by Bertrand (2011), at the ends of the pressure measurement tubes. The H-taps allow the measurement of static pressure while reducing water ingress into the measurement tubes, which cause measurement errors.

The remaining two measurements, the pre-nozzle pressure difference (Δp_{pnz}) and the nozzle pressure difference (Δp_{nzl}), make use of the same pressure connection on the inside wall of the test section above the drift eliminators (see Figure 4.2 for this arrangement). The high-pressure side of the pre-nozzle pressure difference is the atmosphere outside the test section, while the nozzle pressure difference's low-pressure side is connected to four pressure taps equally spaced about the flow measurement nozzle throat circumference.

The instrument's datasheet (Endress + Hauser, 2019*b*) provides equations to calculate the 3-sigma (99.7% confidence level) uncertainty, which is then converted to the 68% confidence level by dividing by 3:

$$b_{\Delta p_{instr}} = 8.902/3 = 2.967 \text{ Pa} \tag{4.6}$$

Additionally the instrument's current output has a resolution of 1 μA, which is considered a separate uncertainty with an assumed 95% confidence level:

$$\begin{aligned} b_{\Delta p_{curr}} &= \left[\frac{1\ \mu\text{A}}{20\ \text{mA} - 4\ \text{mA}} \times (100\ \text{Pa} - (-500\ \text{Pa}))\right]/2 \\ &= 0.0188\ \text{Pa} \end{aligned} \tag{4.7}$$

4.2.3.4 Temperature measurements

The water temperatures at the inlet (T_{wi}) and outlet (T_{wo}) of the test section are measured using Endress + Hauser TLSR1 Pt100 3-wire resistance temperature detectors (RTDs). The RTDs are installed in titanium thermowells in the PVC piping (see Figure 4.6), with the piping being thermally insulated to increase the temperature measurement accuracy. Each RTD is supported by a PR Electronics 3112 Pt100 RTD converter which provides the required supply voltage for the RTD and converts the signal from the RTD to a $4 - 20$ mA signal, corresponding to measured values of -10 °C to 100 °C.

Figure 4.5: Static pressure measurement H-tap

Figure 4.6: Outlet water temperature measurement

The dry- and wet-bulb temperatures of the inlet air are also measured using Endress + Hauser TLSR1 Pt100 3-wire RTDs and PR Electronics 3112 Pt100 RTD converters at a combined "station" (see Figure 4.7a). Atmospheric air near the test section air inlet is drawn to the station using a fan (the PVC air inlet pipe is visible in Figure 4.4). Air flows over the dry-bulb temperature RTD (T_a) first. The air then flows over the wet-bulb RTD (T_{wb}) which is covered by a cotton wick (see Figure 4.7b) that is continuously wetted by cooling water in the level-controlled water container.

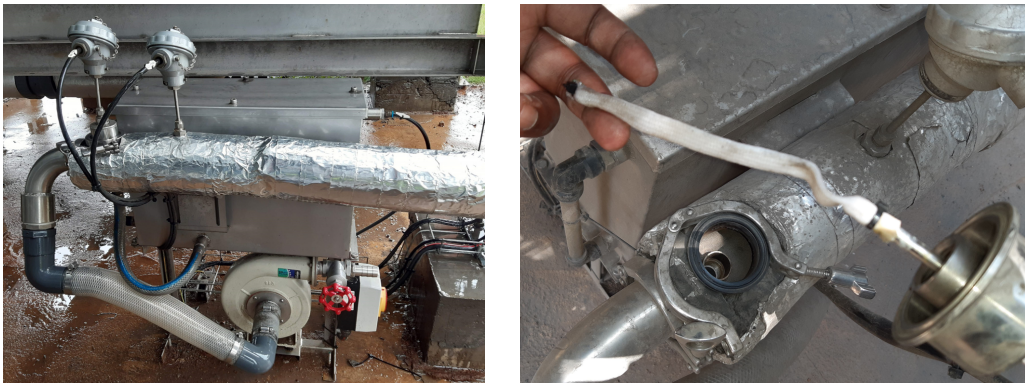

(a) Wet- and dry-buld temperature measurement station

(b) Cotton wick installed on the wet-bulb temperature RTD

Figure 4.7: Ambient temperature measurement equipment

The accuracy of the TLSR1 Pt100 RTDs is provided by Endress + Hauser (undated b) as:

$$b_{T_{RTD}} = [0.15 + 0.002\ |t|]\ /2\ ^\circ\text{C} \tag{4.8}$$

The accuracy of the RTD converter is provided by PR Electronics (undated) as the greater of 0.05% of the range and 0.1 °C. The ranges of all temperature measurements are identical and the uncertainty is calculated as:

$$\begin{aligned} b_{T_{converter}} &= [\max(0.1\ ^\circ\text{C}, 0.05\% \times (100\ ^\circ\text{C} - (-10\ ^\circ\text{C})))]\ /2 \\ &= 0.05\ ^\circ\text{C} \end{aligned} \tag{4.9}$$

4.2.3.5 Wall and bypass water flow rates

The amount of water that enters the test section, but does not flow all the way through the fill is measured in two locations as shown in Figure 4.8a. "Bypass water" is water that is not sprayed onto the fill, but past the fill edges. "Wall water" is sprayed onto the fill, but migrates to the walls by droplets or splashing. Both of these flows are captured by troughs installed on the test section inner walls.

Water captured in the troughs is drained via small drain holes for measurement. Due to the large variation that may exist in these flow rates, a con-

ventional flow instrument, with limitations on allowable flow rate, would not have been sufficient for these measurements. Each flow rate (V_{byp} and V_{wall}) is therefore measured using an iterative flow measurement system where an 8 L container (see Figure 4.8b) is gradually filled by water drained from the respective troughs. When the container is full, an Endress + Hauser Liquiphant FTL31 tuning fork level switch is activated and the contents of the container are drained to the test facility outlet.

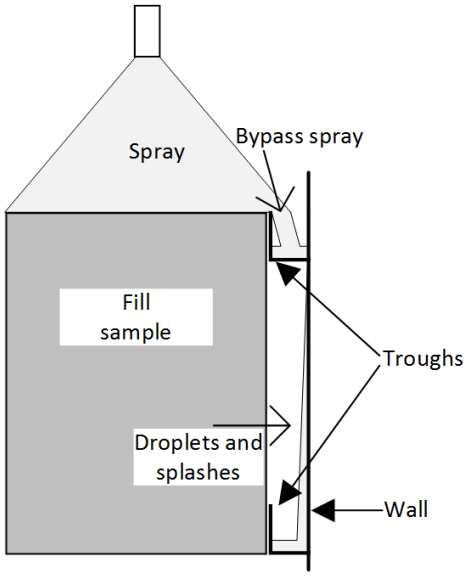

(a) Bypass and wall water flow

(b) Flow measurement container

Figure 4.8: Bypass and wall water

Whenever the container is filled and emptied, the container volume (8 L) is added to a continuously running volume accumulator value stored by the PLC. The change in the volume accumulator value is continuously averaged over the past hour of operation to provide a continuous volume flow rate measurement.

The method of wall and bypass wall water, while reliable, does not provide accurate instantaneous flow measurements. The uncertainty is difficult to estimate given that it is affected by events that may have occurred up to an hour in the past from a particular value being produced. This flow typically makes up less than 3% of the total water flow and uncertainties are expected to be small. Because it is impossible to calculate the uncertainties for a measurement, both the systematic and random uncertainties are neglected for these two flow rates.

4.2.3.6 Fill mass measurement

The fill is installed on top of a steel lattice which is supported from the bottom by three Tedea-Huntleigh 355 500kg C4 hermetically sealed load cells. The load cells are excited by a Loadtech LT1300 load cell indicator, which also digitally

sums the inputs from the load cells and converts this sum to a $4-20$ mA signal. The fill mass is continuously measured for monitoring purposes, with both the water mass and draught affecting the measured mass during operation. The water- and air-flow are shut off once a day for 10 minutes to measure the drip-dry mass of the fill. Changes in the drip-dry fill mass over time are used to determine the accumulated fouling mass. The uncertainty analysis of fill mass measurements do not form part of this study and thus the mass measurement equipment's uncertainties are not discussed.

4.2.3.7 Ambient pressure measurement

The ambient pressure is measured using a single Endress + Hauser Cerabar M PMP51 absolute pressure sensor. This sensor provides a $4-20$ mA output, with a maximum range of 0 kPa to 200 kPa that has been turned down to a range of 60 kPa to 140 kPa.

The instrument's datasheet (Endress + Hauser, 2019*a*) provides equations to calculate the 3-sigma (99.7% confidence level) uncertainty, which is then converted to the 68% confidence level by dividing by 3:

$$b_{p_{a_{instr}}} = 2.167/3 = 0.722 \text{ kPa} \tag{4.10}$$

Additionally, the instrument's current output has a resolution of 1 μA, which is considered a separate uncertainty with an assumed 95% confidence level.

$$\begin{aligned} b_{p_{a_{curr}}} &= \left[\frac{1\ \mu\text{A}}{20\ \text{mA} - 4\ \text{mA}} \times (140\ \text{kPa} - 60\ \text{kPa})\right]/2 \\ &= 0.0025\ \text{kPa} \end{aligned} \tag{4.11}$$

4.2.4 Periodic fill performance tests

Periodic fill performance tests are performed autonomously by the test facility at all four test sections simultaneously. Tests are usually performed weekly during the night, when thunderstorms and high winds are less common in the South African Highveld, and the ambient temperatures are expected to be steady.

A fill performance test consists of interrupting the normal operation of the fill test facility (typically $G_w = 2.6$ kg/m^{2}s and $G_a = 2.0$ kg/m^{2}s) and operating the test sections over ranges of pre-set G_w and G_a values. Each test operating point is maintained for a period of 10 minutes, with all measurements being recorded and stored every 1 minute by the PLC.

The G_a- and G_w-values of a typical fill performance test, as calculated by the test facility PLC, are plotted with time in Figure 4.9. The G_a setpoints for this test are 2.8, 2.5, 2.0, 1.5 and 1 kg/m^{2}s and the G_w setpoints are 2.6, 2.5, 2.0, 1.5 and 1 kg/m^{2}s. Since all combinations of the G_a and G_w setpoints are tested, this results in 25 test operating points. This procedure yields a good compromise between maximising the number of test operating points

and keeping the performance test to a reasonable duration. The small step changes in the G_w-values (for example around 110 minutes in Figure 4.9) are due to suboptimal PID control settings. This does not affect the integrity of the data obtained, as any changes at a single set-point are taken into account in the uncertainty analysis (see Chapter 5).

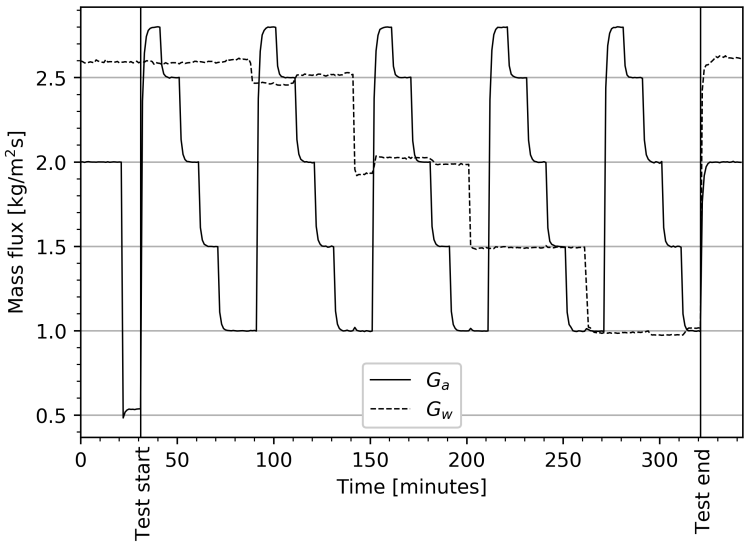

Figure 4.9: G_a and G_w values during a fill performance test

4.3 Data processing

The following sections show the calculation methods for the results (G_w, G_a, Me_{fi} and K_{fd}) of a single test operating point.

4.3.1 Data selection

Data selection for analysis of a fill performance test consists mainly of neglecting transient effects measured after setpoint changes. Due to the relatively long settling time of approximately two minutes for the G_a-value after set-point changes (see Figure 4.9), only the data of the last eight minutes of each 10 minute test operating period is used.

4.3.2 Water mass flux

The fill water mass flux is calculated using the water inlet (V_{wi}), bypass (V_{byp}) and wall (V_{wall}) volume flow rates measured. These volumetric flow rates are converted to mass flow rates using the water inlet density calculated at the water inlet temperature T_{wi} using Equation A.6 to obtain m_{wi}, m_{byp} and m_{wall}.

The fill water mass flow is calculated by subtracting the bypass and wall water flow rates from the inlet flow rate:

$$m_w = m_{wi} - m_{byp} - m_{wall} \tag{4.12}$$

This is divided by the fill frontal area to obtain the fill water mass flux:

$$G_w = \frac{m_w}{A_{fr}} \tag{4.13}$$

4.3.3 Dry air mass flux

The air-flow rate is calculated by measuring the pressure difference across a 550 mm ASME nozzle with a low ratio of throat diameter to outside diameter and a discharge coefficient of $C_d = 0.98$ (see Figure 4.10). The air-vapour mass

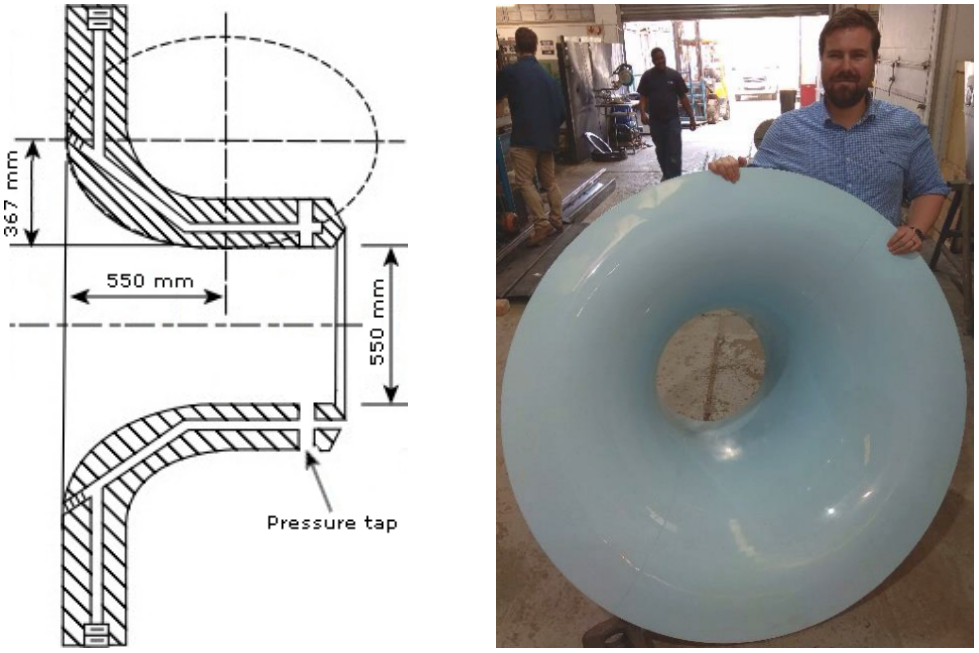

(a) Diagram of air-flow measurement nozzle

(b) Manufactured flow measurement nozzle (Kotze, 2019)

Figure 4.10: Air-flow measurement nozzle

flow rate at the fill outlet (m_{avo}) is calculated using the following equation, modified from White (2005):

$$m_{avo} = \frac{C_d \ \pi \ d_{nzl}^2 \sqrt{2 \ \rho_{avo} \ \Delta p_{nzl}}}{4} \tag{4.14}$$

The nozzle throat diameter is denoted by d_{nzl}. The density at the nozzle inlet (ρ_{avo}) is calculated using Equation A.10, which is a function of air pressure, dry-bulb temperature and wet-bulb temperature. The air pressure at the nozzle inlet is calculated by subtracting the measured pressure difference between the nozzle inlet and atmospheric pressure from the measured atmospheric pressure:

$$p_{pnz} = p_a - \Delta p_{pnz} \tag{4.15}$$

The dry- and wet-bulb temperatures are calculated by assuming that the air-flow at the nozzle inlet (fill outlet) is saturated at a temperature T_{ao} and applying the energy balance:

$$m_w c_{pwm}(T_{wi} - T_{wo}) = m_a(i_{ao} - i_{ai}) \tag{4.16}$$

where c_{pwm} is the mean specific heat capacity of water, calculated using Equation A.5 at $\frac{T_{wi}+T_{wo}}{2}$. The fill inlet and outlet air enthalpies are denoted by i_{ai} and i_{ao} respectively and are both calculated using Equation A.14. The dry air mass flow rate (m_a) is calculated using the following equation:

$$m_a = m_{avo}/(1 + w_{avo}) \tag{4.17}$$

with w_{avo} calculated using Equation A.11 at the saturated outlet temperature T_{ao}. Since m_a is a function of T_{ao}, these equations are implicit and T_{ao} is calculated iteratively.

The dry air mass flux is then calculated using:

$$G_a = \frac{m_a}{A_{fr}} \tag{4.18}$$

4.3.4 Merkel number

The measured Merkel number (Me_{meas}) as presented in Equation 2.31 can not be solve analytically and is approximated using the Chebychev integral as presented in Appendix B.1.

4.3.5 Pressure loss factor

The pressure loss factor can be expressed in different ways depending on the air-vapour mixture's mass flow rate and density (both vary through the fill) being used. The test facility manufacturer chose the mean mass flow rate and density during the software design of the facility and that selection is maintained during this study.

Kröger (2004) provides the following equation for the arithmetic mean air-vapour mass flow rate:

$$m_{avm} = \frac{m_{avi} + m_{avo}}{2} \tag{4.19}$$

and for the harmonic mean density:

$$\rho_{avm} = 2\left(\frac{1}{\rho_{avi}} + \frac{1}{\rho_{avo}}\right)^{-1} \tag{4.20}$$

The pressure loss factor factor, taking the dynamic pressure and elevation difference into account, is calculated (as in Kröger (2004), also see Section 2.2.1.6) using:

$$\begin{aligned} K_{meas} = 2\,[\Delta p_{fi} - (\rho_{avo} v_{avo}^2 - \rho_{avi} v_{avi}^2) + (\rho_{avi} - \rho_{avm})\; g\; L_{fi}] \\ \times\, \rho_{avm} A_{fr}^2 / m_{avm}^2 \end{aligned} \tag{4.21}$$

4.4 Rain zone and spray zone corrections

4.4.1 Premise

Since the water inlet and outlet temperatures (T_{wi} and T_{wo}) measured include the effects of heat- and mass-transfer in the rain and spray zones, the Merkel number, as measured, needs to be corrected by removing the effects of these zones. Similarly, with the fill pressure difference (Δp_{fi}) being measured between the spaces directly below the fill (at the top of the rain zone) and above the spray zone, the effect of the spray zone pressure loss needs to be corrected for.

In the same way that the Merkel number and pressure loss factors of components in series in a NDWCT performance prediction calculation can be summed algebraically, the spray and rain zone Merkel number and the spray zone pressure loss factor are algebraically subtracted from the measured values to calculated the corrected values:

$$Me_{fi} = Me_{meas} - Me_{sp} - Me_{rz} \tag{4.22}$$

$$K_{fd} = K_{meas} - K_{sp} \tag{4.23}$$

Bertrand (2011) did a similar analysis of a cooling tower fill test facility located at Stellenbosch University, although in that design, with the fan providing draught located at the inlet, the outlet water is captured by metal troughs located below the fill, which cause a relatively high pressure loss. In that case, the Merkel number and pressure loss factors of both the spray zone and rain zone were measured by removing the fill sample from the facility, locating the movable sprayer assembly at 150 mm above the troughs and performing tests of the Merkel number and pressure loss factor. Regressions of these as functions of G_w and G_a were performed and used to calculate Merkel number and pressure loss factor corrections that are subtracted from the corresponding values during fill performance testing.

The same method is not possible in the current test facility since the spray assembly and water collection sump can not be moved. Simply testing without fill samples installed would overestimate both the Merkel number and pressure loss factor due to the large distance between the sprayers and the collection sump contributing to both performance parameters. A different method of taking the rain and spray zones into account is thus required.

4.4.2 Rain zone

Kröger (2004) provides an equation for the Merkel number of the cross-counter flow rain zone of rectangular mechanical draught counterflow wet cooling towers with air entering from both sides. The rain zone width and height of the fill fouling test facility do not fall within the ranges of applicability of this equation. Kröger (2004) further provides the following equation for a purely

counterflow rain zone:

$$\begin{aligned} Me_{rz} = 3.6 &\left(\frac{p_a}{R_v T_a \rho_w}\right)\left(\frac{D}{v_{azo} d_d}\right)\left(\frac{H_{rz}}{d_d}\right) Sc^{0.33} \\ &\times \left[\ln\left(\frac{w_s + 0.622}{w + 0.622}\right)/(w_s - w)\right] \\ &\times [4.68851\ a_\rho \rho_a - 187128.7\ a_\mu \mu_a - 2.29322 \\ &+ 22.4121\ \left(0.350396\ (a_v v_{azo})^{1.38046} + 0.18\right) \\ &\times \left(0.83666\ (a_L H_{rz})^{-0.5299} + 0.42\right) \\ &\times \left(43.0696\ (a_L d_d)^{0.7947} + 0.52\right)] \end{aligned} \tag{4.24}$$

Where the range of applicability is:

$$1 \text{ m/s} \leq v_{azo} \leq 5 \text{ m/s}$$
$$0.5 \text{ m} \leq H_{rz} \leq 5.5 \text{ m}$$

which is acceptable for this study. Sc denotes the Schmidt number, calculated using Equation 2.85, D denotes the diffusion coefficient in gases, calculated using Equation 2.86. The coefficients a_μ, a_ρ, a_v and a_L are calculated using Equations 2.48 through 2.51 respectively. A comparison of the rectangular tower rain zone and pure counterflow rain zone Merkel numbers showed a difference in the overall measured Merkel number less than 1% and therefore the pure counterflow of Equation 4.24 is used within its applicability limits in this study.

The droplet diameter (d_d) in the test facility rain zone is unknown. To ensure a fair comparison between different fill samples without measurement of the droplet sizes, the same droplet size of 5.0 mm is assumed. The performance effect of rain zone droplet size was studied by Terblanche (2008) and Terblanche (2011) using photographic and videographic methods respectively. If detailed quantification of rain zone performance becomes necessary, these methods, or variations thereof, may be used. These are, however, highly specialised methods and may not be adequate for long-term testing.

4.4.3 Spray zone

The Merkel number and pressure loss factors for the test section spray zone are calculated using Equation 2.89 and Equation 2.62 respectively. These equations are independent of cooling tower dimensions other than the spray zone depth and they are therefore expected to be relatively accurate for the test facility.

4.5 Fill performance characteristic equation

The capabilities of this test facility determines the fill characteristic equation forms that may be used in this study. Since the water inlet temperature, determined by the operation of the power plant and main NDWCT, can not

be controlled, its effects on the fill thermal performance, suggested for inclusion in charateristic equations by Kloppers (2003), can not be quantified.

Furthermore, due to the long test duration of each fill sample, it is not possible to investigate the effects of fill height. The characteristic equation forms selected for this study are therefore Equation 2.87 for the Merkel number and Equation 2.54 for the pressure loss factor. The characteristic equations are obtained by non-linear least squares regression of the corrected results of all test operating points in a performance test.

Chapter 5: Uncertainty analysis

5.1 Introduction

It is desirable to quantify the effect of fill performance testing experimental uncertainty on the performance prediction of NDWCTs to provide confidence when selecting fills for installation. This is especially important for state-owned companies, like Eskom, which need to adequately justify their commercial decisions.

The uncertainty analysis of a single test operating point was performed by Van der Merwe (2007) for a NDWCT fill test facility located at Stellenbosch University. The Merkel number per meter fill height and pressure loss coefficient per meter fill height uncertainties were applied directly to a NDWCT performance prediction calculation by multiplying these values by the modelled fill height as a form of propagation (taking account of the experimental uncertainty in NDWCT performance prediction calculations). This propagated uncertainty, combined with other measurement uncertainties anticipated for NDWCT performance tests, was used to determine the feasibility of attaining a specified accuracy of NDWCT performance tests using fill performance test inputs. The fact that this method only uses a single test operating point, the method of propagation, and the fact that it also neglects correlated uncertainties makes it inadequate to evaluate the effects of experimental uncertainties of a fill performance test on NDWCT performance predictions.

A process similar to that of Van der Merwe (2007) is followed in this study to calculate test operating point result uncertainties (G_w, G_a, Me_{fi} and K_{fd}), with this process being repeated for every test operating point in a fill performance test. The uncertainties of all test operating points, including correlated uncertainties, are propagated first to regression uncertainties and finally to the NDWCT performance uncertainty to provide a general uncertainty analysis approach for NDWCT fill performance testing.

5.2 Uncertainty analysis theory

The uncertainty analysis in this study is performed mainly according to ASME (2014), with the symbols, definitions and equations being from that source, unless otherwise mentioned.

5.2.1 Core concepts

Testing, or obtaining a test result, is the act of obtaining an estimate of a true value by measurement. This true value, and consequently also the true error, of the measurement can never be known. As such, the uncertainty, defined as the "limit of the error" can only be estimated using statistical and other

means.

Figure 5.1 provides an illustration of measurement errors in a population of measurements. The population here indicates the set of all possible values of the measurement, with the population distribution indicating the frequency of occurrence of specific values if infinitely many measurements are taken. The difference between the true value and the population mean (μ), is called the systematic error (β). The figure also shows the following for a single measurement (j) within the population: the value of the measurement (X_j), the total error of the measurement (δ_j), which is the difference between the measured value and the true value and the random error (ε_j), the difference between the measured value and the population mean.

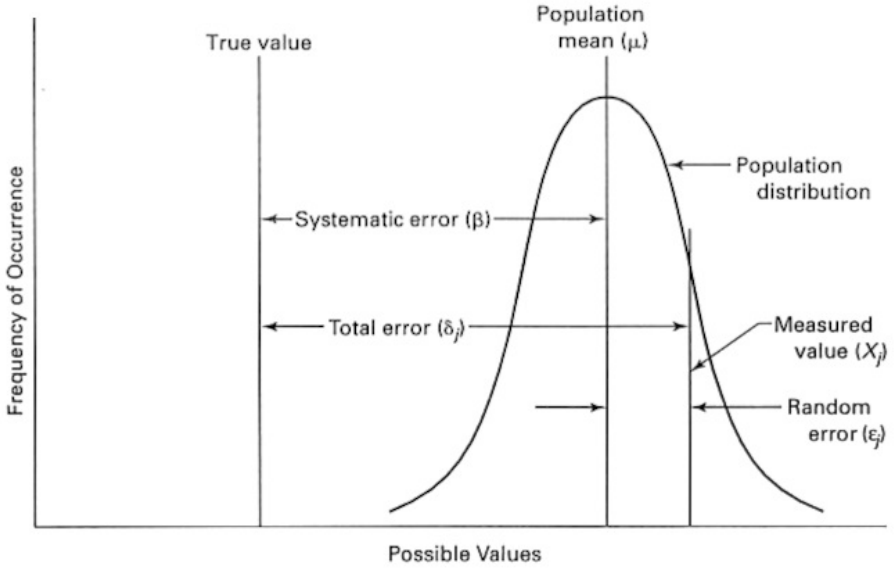

Figure 5.1: Frequency of occurrence of values in a population of measurements (ASME, 2014)

5.2.2 Random measurement uncertainty

Random measurement uncertainty is the estimate of the limit of errors caused by random changes during repeated measurement of the true value of a single parameter. For real measurements (not an infinite number), μ is estimated by the mean of a sample of N measured values (X_j) using:

$$\overline{X} = \frac{\sum_{j=1}^{N} X_j}{N} \tag{5.1}$$

The random standard uncertainty, the range from the mean within which the true population mean lies with a probability of approximately 68%, is an

estimate of the population standard error and is expressed as:

$$s_{\overline{X}} = \sqrt{\frac{\sum_{j=1}^{N} \frac{(X_j - \overline{X})^2}{N-1}}{N}} \tag{5.2}$$

Since there is no evidence to the contrary, the distribution of the population of measurements in this study is assumed, as in ASME (2014), to be normal (Gaussian).

5.2.3 Systematic measurement uncertainty

The systematic measurement uncertainty is the estimate of the limit of the error (β) that is expected to remain constant from one measurement to the next. It is necessary to perform an analysis of the testing system to identify all possible sources of systematic uncertainty, called elemental systematic uncertainty sources.

For a single measured parameter, the true systematic error of the population (β) is unknown and is estimated by the systematic standard uncertainty of the measurement using:

$$b_{\overline{X}} = \left[\sum_{k=1}^{K} (b_{\overline{X}_k})^2\right]^{0.5} \tag{5.3}$$

where $b_{\overline{X}_k}$ is the individual elemental source uncertainty.

Elemental sources of systematic uncertainty may arise from instrumentation, data acquisition, data processing, calibration, installation or other factors. Section 5.4 provides a detailed discussion of the systematic uncertainties identified for the current test facility.

5.2.4 Result uncertainty

The effects of measurement uncertainties on result uncertainties (known as propagated uncertainties) are calculated with the equations below and is called Taylor series propagation (Coleman and Steele, 2018). The propagated random uncertainty of a result (R) is expressed by:

$$s_R = \left[\sum_{i=1}^{I} (\theta_i s_{\overline{X}_i})^2\right]^{0.5} \tag{5.4}$$

and the propagated systematic uncertainty of a result is expressed by:

$$b_R = \left[\sum_{i=1}^{I} (\theta_i b_{\overline{X}_i})^2\right]^{0.5} \tag{5.5}$$

where I is the number of measured parameters and the sensitivity index of the result (R) to the measured parameter $\overline{X}_i$ is expressed by:

$$\theta_i = \frac{\partial R}{\partial \overline{X}_i} \tag{5.6}$$

Partial differentiation here, and for the remainder of this study, are performed numerically using the forward difference method (see Appendix B.2).

If a result uses inputs that share systematic uncertainty sources, such as instruments being calibrated against the same standard or a result using multiple measurements from the same instrument, these uncertainty sources are "correlated" and the uncertainty of the result is calculated using:

$$b_R{}^2 = \sum_{i=1}^{I} (\theta_i b_{\overline{X}_i})^2 + 2 \sum_{i=1}^{I-1} \sum_{k=i+1}^{I} \theta_i \theta_k b_{ik} \tag{5.7}$$

where the "covariance" between inputs i and k is calculated using:

$$b_{ik} = \sum_{l=1}^{L} b_{i_l} b_{k_l} \tag{5.8}$$

for I measured paramaters and L correlated uncertainty sources. To ensure that units remain consistent, this is interpreted as b_{i_l} being the uncertainty in i resulting from uncertainty source l, thus:

$$b_{i_l} = \frac{\partial i}{\partial l} b_l \tag{5.9}$$

5.2.5 Degrees of freedom and confidence level

For a normally distributed population of measurements, the range $\overline{X} \pm s_{\overline{X}}$ is expected to contain the true mean of the population (μ) with a probability (or confidence level) of 68%, which is known as the standard uncertainty or 1-sigma uncertainty. Uncertainty can be expressed at other confidence levels, known as expanded uncertainties. Expanded uncertainties are calculated by multiplying the standard uncertainty by a multiplier (t) which is a function of the desired confidence level (C) and the degrees of freedom (v) of the measurement. The degrees of freedom is defined by ASME (2014) as "the number of independent observations used to calculate a statistic". ASME (2014) further provides equations to calculate the degrees of freedom of both random and systematic errors and ultimately obtain the value of t.

It is common practice in engineering to report uncertainties at the 95% confidence level. In cases where large or infinite degrees of freedom may be assumed, this translates to a multiplier of 1.960, although both ASME (2014) and Coleman and Steele (2018) generally use a value of 2. A sample size of 30 is stated by ASME (2014) to be large enough to use a value of $t = 2$.

Due to a small sample size (typically 8) of measurements taken at each test op-

erating point in the current study, it is not reasonable to assume large degrees of freedom and individual values of t need to be calculated for every measurement. This significantly complicates the calculation of expanded uncertainties for the current study.

It would be trivial to obtain sample sizes greater than 30 in future work at the same test facility or at other similar facilities, by simply increasing the sampling rate during performance tests. This would allow the simple calculation of the 95% uncertainties. For this reason it is selected to calculate and report uncertainties in this study at the standard (68%) confidence level. Only minor changes are required to the presented methods to perform future uncertainty calculations at the 95% confidence level when sufficiently large sample sizes are available.

5.2.6 Regression uncertainty

Where a regression on test results is used, as in Section 4.5, there are uncertainties associated with the measured results, as well as uncertainties in performing the regression itself. The output of a single-input regression function is expressed as:

$$\hat{Y} = f(X_{new}) \tag{5.10}$$

where f is generated using measured or calculated values $(X_1, X_2, ..., X_N)$ and $(Y_1, Y_2, ..., Y_N)$ for N regression data points.

The uncertainty in the regression output $(u_{\hat{Y}})$ at the input (X_{new}) is expressed by Equation 5.11 (combined from ASME (2014) and Coleman and Steele (2018)). This equation will be adapted for use in the current fill performance tests and to aid in explaining the adaptations, a description of each term is added:

$$
\begin{aligned}
u_{\hat{Y}}^2 = & \underbrace{\sum_{i=1}^{N}\left(\frac{\partial \hat{Y}}{\partial Y_i}\right)^2 b_{Y_i}^2}_{Y_i \text{ systematic}} + \underbrace{2\sum_{i=1}^{N-1}\sum_{k=i+1}^{N}\left(\frac{\partial \hat{Y}}{\partial Y_i}\right)\left(\frac{\partial \hat{Y}}{\partial Y_k}\right) b_{Y_i Y_k}}_{Y_i Y_k \text{ correlation}} \\
& + \underbrace{\sum_{i=1}^{N}\left(\frac{\partial \hat{Y}}{\partial X_i}\right)^2 b_{X_i}^2}_{X_i \text{ systematic}} + \underbrace{2\sum_{i=1}^{N-1}\sum_{k=i+1}^{N}\left(\frac{\partial \hat{Y}}{\partial X_i}\right)\left(\frac{\partial \hat{Y}}{\partial X_k}\right) b_{X_i X_k}}_{X_i X_k \text{ correlation}} \\
& + \underbrace{2\sum_{i=1}^{N}\sum_{k=1}^{N}\left(\frac{\partial \hat{Y}}{\partial X_i}\right)\left(\frac{\partial \hat{Y}}{\partial Y_k}\right) b_{X_i Y_k}}_{X_i Y_k \text{ correlation}} \\
& + \underbrace{\left(\frac{\partial \hat{Y}}{\partial X_{new}}\right)^2 b_{X_{new}}^2}_{X_{new} \text{ systematic}} + \underbrace{2\sum_{i=1}^{N}\left(\frac{\partial \hat{Y}}{\partial X_{new}}\right)\left(\frac{\partial \hat{Y}}{\partial X_i}\right) b_{X_{new} X_i}}_{X_{new} X_i \text{ correlation}} \\
& + \underbrace{2\sum_{i=1}^{N}\left(\frac{\partial \hat{Y}}{\partial X_{new}}\right)\left(\frac{\partial \hat{Y}}{\partial Y_i}\right) b_{X_{new} Y_i}}_{X_{new} Y_i \text{ correlation}} + \underbrace{\sum_{i=1}^{N}\left(\frac{\partial \hat{Y}}{\partial Y_i}\right)^2 s_{Y_i}^2}_{Y_i \text{ random}} \\
& + \underbrace{\sum_{i=1}^{N}\left(\frac{\partial \hat{Y}}{\partial X_i}\right)^2 s_{X_i}^2}_{X_i \text{ random}} + \underbrace{\left(\frac{\partial \hat{Y}}{\partial X_{new}}\right)^2 s_{X_{new}}^2}_{X_{new} \text{ random}}
\end{aligned}
\tag{5.11}
$$

The systematic and random uncertainties of each measured or calculated input (X_i), measured or calculated output (Y_i) and the regression function input (X_{new}), as well as correlated uncertainty between all systematic uncertainties are taken into account. Note that where correlation of similar measurements (such as Y_i and Y_k) is considered, the summations are $\sum_{i=1}^{N-1}\sum_{k=i+1}^{N}$, whereas the correlation of dissimilar measurements (such as X_i and Y_k) use $\sum_{i=1}^{N}\sum_{k=1}^{N}$. According to ASME (2014), this method accounts for both the uncertainty in measurement and the accuracy of the fit.

5.3 Uncertainty calculation of fill performance tests

The following sections present the method used to calculate the systematic equipment and measurement random uncertainties of measurements taken during a fill performance test and how these are propagated to the NDWCT performance. Figure 5.2 shows the process followed to calculate the NDWCT

performance uncertainty, with dashed lines indicating data being used to calculate correlated systematic uncertainties.

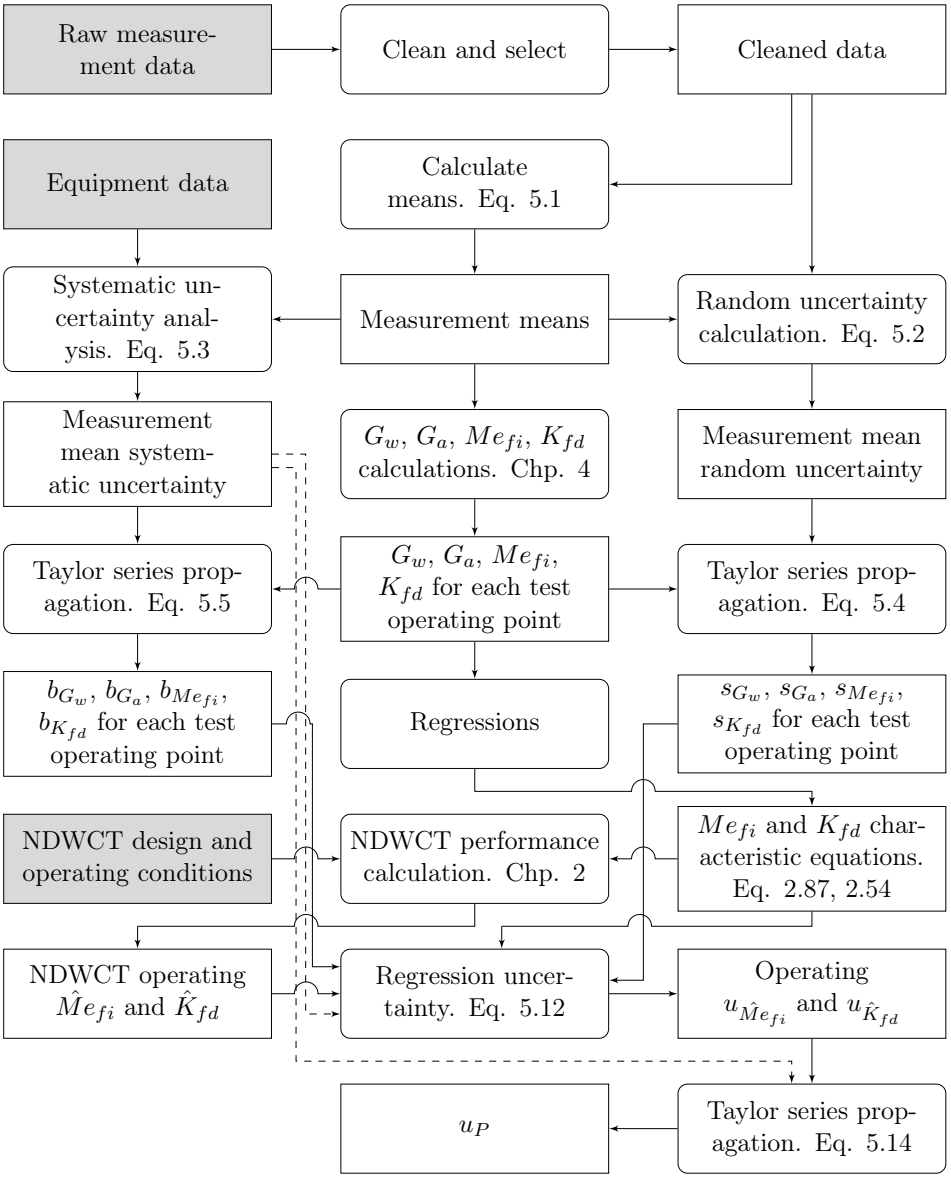

Figure 5.2: Flow diagram of NDWCT performance uncertainty calculation

5.3.1 Measurement and result uncertainties

Measurement random and systematic uncertainties are calculated for the mean of the measurements taken at each test operating point using Equations 5.2 and 5.3 respectively. The equipment elemental uncertainty sources for the current test facility are quantified in Section 4.2.3.

Result random and systematic uncertainties are calculated for all test operating point results (G_w, G_a, Me_{fi} and K_{fd}). The result random uncertainties

are calculated using Equation 5.4 and the systematic result uncertainties are calculated using either Equation 5.5 or 5.7. Due to the selection, installation and calibration of instruments at the current test facility, no correlated uncertainties between individual instruments could be identified, thus Equation 5.5 is used.

5.3.2 Regression uncertainty

The regression uncertainty calculation in Section 5.2.6 applies to regression of a single input and a single output. Since the regressions performed for the fill performance tests consist of two inputs (G_w and G_a) and one output (Me_{fi} or K_{fd}), Equation 5.11 is modified in this section to fit the current application, providing the uncertainty ($u_{\hat{Y}}$) where $\hat{Y} = f(G_{w_{new}}, G_{a_{new}})$, with $\hat{Y}$ representing either $\hat{Me}_{fi}$ or $\hat{K}_{fd}$. These regression uncertainty calculations produce the uncertainty of a specific output, at specific inputs and thus the operating point ($G_{w_{new}}$ and $G_{a_{new}}$) for the fill is obtained from the NDWCT performance prediction calculation (Chapter 2).

Adapting Equation 5.11 for the current test facility is done by firstly removing all X_{new} terms since only the uncertainty in the fill test facility is considered; $G_{a_{new}}$ and $G_{a_{new}}$ are fixed values determined by the NDWCT performance. For a wider study of NDWCT performance uncertainties, including uncertainties not propagated from fill performance uncertainties, $G_{w_{new}}$ and $G_{a_{new}}$ terms would have to be reintroduced. Secondly, the systematic, random and correlated uncertainty terms for a second measured input are added.

Note that, as in Equation 5.11, where correlation of similar measured parameters (such as Y_i with Y_k) are calculated, the summation is $\sum_{i=1}^{N-1} \sum_{k=i+1}^{N}$, whereas for the correlation of dissimilar measured parameters (such as X_i with Y_k), $\sum_{i=1}^{N} \sum_{k=1}^{N}$ is used. The two regression inputs are renamed G_w and G_a and the adaptations yield:

$$
\begin{aligned}
u_{\hat{Y}}^2 = & \sum_{i=1}^{N}\left(\frac{\partial \hat{Y}}{\partial Y_i}\right)^2 b_{Y_i}^2 + 2\sum_{i=1}^{N-1}\sum_{k=i+1}^{N}\left(\frac{\partial \hat{Y}}{\partial Y_i}\right)\left(\frac{\partial \hat{Y}}{\partial Y_k}\right) b_{Y_i Y_k} \\
& + \sum_{i=1}^{N}\left(\frac{\partial \hat{Y}}{\partial G_{w_i}}\right)^2 b_{G_{w_i}}^2 + 2\sum_{i=1}^{N-1}\sum_{k=i+1}^{N}\left(\frac{\partial \hat{Y}}{\partial G_{w_i}}\right)\left(\frac{\partial \hat{Y}}{\partial G_{w_k}}\right) b_{G_{w_i} G_{w_k}} \\
& + 2\sum_{i=1}^{N}\sum_{k=1}^{N}\left(\frac{\partial \hat{Y}}{\partial G_{w_i}}\right)\left(\frac{\partial \hat{Y}}{\partial Y_k}\right) b_{G_{w_i} Y_k} + \sum_{i=1}^{N}\left(\frac{\partial \hat{Y}}{\partial G_{a_i}}\right)^2 b_{G_{a_i}}^2 \\
& + 2\sum_{i=1}^{N-1}\sum_{k=i+1}^{N}\left(\frac{\partial \hat{Y}}{\partial G_{a_i}}\right)\left(\frac{\partial \hat{Y}}{\partial G_{a_k}}\right) b_{G_{a_i} G_{a_k}} \\
& + 2\sum_{i=1}^{N}\sum_{k=1}^{N}\left(\frac{\partial \hat{Y}}{\partial G_{a_i}}\right)\left(\frac{\partial \hat{Y}}{\partial Y_k}\right) b_{G_{a_i} Y_k} \\
& + 2\sum_{i=1}^{N}\sum_{k=1}^{N}\left(\frac{\partial \hat{Y}}{\partial G_{w_i}}\right)\left(\frac{\partial \hat{Y}}{\partial G_{a_k}}\right) b_{G_{w_i} G_{a_k}} + \sum_{i=1}^{N}\left(\frac{\partial \hat{Y}}{\partial Y_i}\right)^2 s_{Y_i}^2 \\
& + \sum_{i=1}^{N}\left(\frac{\partial \hat{Y}}{\partial G_{w_i}}\right)^2 s_{G_{w_i}}^2 + \sum_{i=1}^{N}\left(\frac{\partial \hat{Y}}{\partial G_{a_i}}\right)^2 s_{G_{a_i}}^2
\end{aligned}
\tag{5.12}
$$

where Y may be replaced by Me_{fi} and K_{fd} respectively to calculate $u_{\hat{Me}_{fi}}$ and $u_{\hat{K}_{fd}}$.

For the current test facility, measurements at different test operating points make use of the same instruments and equipment and thus these measurements' systematic uncertainties are considered fully correlated. In Equation 5.12, covariances between individual measured inputs or outputs (such as $b_{G_{a_i} G_{w_k}}$) must consider that all 11 instruments are shared, so the covariance in this example is:

$$
b_{G_{a_i} G_{w_k}} = \sum_{j}^{11} \frac{\partial G_{a_i}}{\partial \overline{X}_{i,j}} b_{\overline{X}_{i,j}} \frac{\partial G_{w_k}}{\partial \overline{X}_{k,j}} b_{\overline{X}_{k,j}} \tag{5.13}
$$

where $\overline{X}_{i,j}$ is the mean measured value of instrument j at test operating point i. The other covariances are calculated similarly.

5.3.3 NDWCT performance prediction uncertainty

The regression uncertainties calculated in Section 5.3.2, along with correlated uncertainties, are propagated to the NDWCT performance uncertainty using the Taylor series method for a NDWCT performance parameter P (such as T_{wo}) by employing Equation 5.7 in the following form:

$$
{u_P}^2 = (\theta_{\hat{Me}_{fi}} u_{\hat{Me}_{fi}})^2 + (\theta_{\hat{K}_{fd}} u_{\hat{K}_{fd}})^2 + 2\theta_{\hat{Me}_{fi}} \theta_{\hat{K}_{fd}} \sum_{l=1}^{L} b_{\hat{Me}_{fi_l} \hat{K}_{fd_l}} \tag{5.14}
$$

for L correlated uncertainty sources. The sensitivity indexes:

$$\theta_{\hat{Me}_{fi}} = \frac{\partial P}{\partial \hat{Me}_{fi}} \tag{5.15}$$

$$\theta_{\hat{K}_{fd}} = \frac{\partial P}{\partial \hat{K}_{fd}} \tag{5.16}$$

are calculated numerically using the NDWCT performance prediction calculation.

For the current test facility, the regression outputs $\hat{Me}_{fi}$ and $\hat{K}_{fd}$ share all 11 instruments at all 25 test operating points, resulting in:

$$\sum_{l=1}^{L} b_{\hat{Me}_{fi_l}\hat{K}_{fd_l}} = \sum_{i=1}^{25}\sum_{k=1}^{25}\sum_{j=1}^{11} \frac{\partial \hat{Me}_{fi}}{\partial \overline{X}_{i,j}} b_{\overline{X}_{i,j}} \frac{\partial \hat{K}_{fd}}{\partial \overline{X}_{k,j}} b_{\overline{X}_{k,j}} \tag{5.17}$$

where $\overline{X}_{i,j}$ is the measured value of instrument j at test operating point i.

5.4 Identified systematic uncertainty sources

The possible sources of systematic uncertainty in the current or similar fill test facilities are discussed in the following subsections. This includes motivations to take account or neglect each identified source in the current study. In general, sources that could not be adequately quantified are neglected for the current study.

5.4.1 Equipment uncertainty

Instruments and other supporting equipment have inherent uncertainty which is dependent on their type and quality. Depending on the installation, wiring or intermediate components may also introduce uncertainty. These uncertainty values are usually obtained from published equipment documentation.

Where uncertainties are obtained from equipment documentation, they are frequently provided with only one or two significant figures. Since they are the limits of the error these values are assumed to be absolute and calculations done with them are unaffected by the low number of significant figures.

5.4.2 Spatial uncertainty

Uncertainty is introduced when a location at a single point in a measurement space is used to represent a measured parameter. An example would be the temperature measurement of inlet air to the test section at a single point, while a temperature distribution exists across the inlet area. Where redundant measurements of a parameter are taken, the systematic uncertainty due to spatial effects can be estimated by calculations provided in ASME (2014), however, at the current test facility, only single measurements of all parameters are taken and the spacial uncertainty can not be quantified.

Engineering judgement and experience may be used in future studies to esti-

mate this spacial uncertainty in the case of only single measurements being available.

5.4.3 Calibration uncertainty

Uncertainty is introduced when a calibration curve is applied or when a specification conformance test is done. The calibration uncertainty calculation includes the uncertainty of the standard against which the equipment is calibrated. For all equipment in this study, specification conformance tests were performed before they were supplied to the test facility manufacturer. It is thus assumed that all possible uncertainties applicable during the specification conformance tests were taken into account and that the stated or certified uncertainties of the equipment include them.

5.4.4 Correction uncertainties

Since the simulation of the rain zone and spray zone for correction (see Section 4.4) are thought to be only moderately accurate approximations of the test facility rain and spray zones, the uncertainties applicable to these calculations are not considered a good estimate of their errors. For that reason, the corrections are used without taking their uncertainties, resulting from measurement uncertainties, into account. Consequently, when sensitivity indexes (θs) of the Merkel number and pressure loss factors are calculated (Equation 5.6), they are calculated for the uncorrected results.

5.4.5 Fluid properties

The air and water fluid properties used in these calculations are obtained from Kröger (2004), who in turn obtained them from a variety of sources, of which only ASHRAE (2001) was available to the candidate. Neither Kröger (2004) nor ASHRAE (2001) mention the uncertainty associated with these fluid property relations, other than ASHRAE (2001) stating that the relations are "sufficiently accurate for most engineering calculations in air-conditioning practice."

It is expected that most comparable studies of fill testing uncertainty analysis would also use the same or similar fluid properties as Kröger (2004) and since no details of the uncertainty could be obtained, the uncertainties of fluid properties are neglected.

5.5 Analysis and proposals for uncertainty analysis

It is desirable to neglect the calculation of correlated uncertainties due to the significant complication this adds to uncertainty calculation. To this end, Appendix E includes calculations of regression and NDWCT performance prediction uncertainties neglecting correlated uncertainties to analyse the effect of neglecting correlated uncertainties.

Table 5.1 summarises the results of the regression uncertainty calculations and it is observed that neglecting correlated uncertainties produces significant errors in the regression uncertainty calculation of approximately 77% and 68% compared to $u_{\hat{Me}_{fi}}$ and $u_{\hat{K}_{fd}}$ respectively. This indicates that it is vital to include correlated uncertainties when calculating regression uncertainties (Equation 5.12).

Table 5.1: Summary of calculated regression uncertainties

Description	**Eq.**	**Thermal**	**Eq.**	**Hydraulic**
Operating point	D.14	$Me_{fi} = 1.637$	D.10	$K_{fi} = 13.730$
Regression uncertainties including correlated uncertainties	E.1	$u_{\hat{Me}_{fi}} = 0.0913$	E.2	$u_{\hat{K}_{fd}} = 2.562$
Regression uncertainties with correlated uncertainties neglected	E.3	$u^*_{\hat{Me}_{fi}} = 0.0211$	E.4	$u^*_{\hat{K}_{fd}} = 0.823$

Table 5.2 summarises the results of the NDWCT performance (quantified by T_{wo}) uncertainty. It is observed that neglecting correlated uncertainties for the NDWCT T_{wo} produces a small error of only 2.4% compared to $u_{T_{wo}}$. This indicates that NDWCT T_{wo} uncertainty can be calculated reasonably accurately when neglecting correlated uncertainty (Equation 5.14).

Table 5.2: Summary of calculated NDWCT T_{wo} uncertainties

Description	**Ref.**	**Value**
NDWCT water outlet temperature	App. D.2	$T_{wo} = 21.459$ °C
NDWCT water outlet temperature uncertainty	Eq. E.5	$u_{T_{wo}} = 0.339$ °C
NDWCT water outlet temperature uncertainty with correlated uncertainties neglected	Eq. E.6	$u^*_{T_{wo}} = 0.347$ °C

This behaviour is expected to be general for all similar fill performance test facilities due to the low sensitivity of regression outputs to individual measurements. Investigation of the generality of this behaviour at other fill performance test facilities, with different instrumentation layouts, is encouraged.

A NDWCT operator comparing the performance of different fills for the purpose of making a selection for installation in their NDWCT, should include fill performance testing experimental uncertainties in their fill selection process to prevent unreported or unanticipated uncertainties leading to incorrect cooling tower performance prediction calculations and potentially a non-optimal fill selection. However, inclusion of NDWCT performance correlated uncertainties would be impossible to perform without detailed knowledge of the test facility equipment (for systematic uncertainty calculation) and testing data (for random uncertainty calculation), information the fill supplier is unlikely to provide. The small error introduced by neglecting correlated uncertainties in the NDWCT performance uncertainty calculation allows an approach to addressing this lack of information: fill suppliers provide the fill performance

characteristics (Equation 2.87 and 2.54) along with their respective uncertainties (calculated using Equation 5.12) in either tabulated or graphical (such as Figure E.1) form. The NDWCT performance uncertainty can then be approximated by neglecting the correlated uncertainties at the NDWCT performance stage:

$$u_P{}^2 \approx (\theta_{\hat{Me}_{fi}} u_{\hat{Me}_{fi}})^2 + (\theta_{\hat{K}_{fd}} u_{\hat{K}_{fd}})^2 \tag{5.18}$$

with the sensitivity indexes (θs) being calculated by the NDWCT user using Equation 5.15 and 5.16.

5.6 Conclusion

A method is presented to accurately calculate the effect of fill performance testing experimental uncertainty in NDWCT cooling tower performance prediction calculations. This method may be adapted to apply to individual fill performance test facilities; specifically, the calculation of all systematic uncertainties and correlated uncertainties will depend on each facility's specific equipment setup.

The importance of correlated uncertainty in fill thermal performance tests at the current facility is investigated. It is concluded that correlated uncertainties are vital when calculating the regression uncertainties, while relatively small errors are introduced if correlated uncertainties are neglected in the NDWCT performance uncertainty calculation. An approach is proposed for NDWCT users without detailed fill test facility information or raw test data to calculate a reasonably accurate NDWCT performance uncertainty.

Chapter 6: Fill fouling as separate thermal and hydraulic effects

6.1 Introduction

The fill fouling literature presented in Chapter 3 contains methods of fill fouling quantification, but lacks a way to perform NDWCT performance calculations or life-cycle calculations including the effects of fill fouling. While the method of rejecting fills displaying a daily mass gain above a certain threshold, reported by Monjoie *et al.* (1993), is transparent and relatively easy to implement, it may be viewed as unfair since a given mass gain may have different performance effects for different fill designs. To enable fair comparison between fills, a method is developed to utilise measured or predicted fill performance to quantify the effect of fill fouling on NDWCT performance.

6.2 Numerical investigation of fill performance degradation using Monte Carlo methods

6.2.1 Premise

The interaction between the fill Merkel number and pressure loss factor in NDWCT performance prediction calculations is complex, with changes in either of the two performance parameters affecting the air mass flow. This in turn changes the operating point on the fill performance characteristic equation. It has, however, been observed that for numerous real NDWCT performance prediction calculations, this interaction appeared negligible for moderate and even high levels of degradation applied numerically to the fills' performance parameters. This observation is termed "separability" and is expressed as:

$$\Delta T_{wo} = \Delta T_{wo,Me_{fi}} + \Delta T_{wo,K_{fd}} + \epsilon \tag{6.1}$$

where $\Delta T_{wo,Me_{fi}}$ is the change in T_{wo} due to degradation (decrease) in fill Merkel number only, $\Delta T_{wo,K_{fd}}$ is the change in T_{wo} due to degradation (increase) in the pressure loss factor only, ΔT_{wo} is the total change in T_{wo} due to simultaneous Merkel number and pressure loss factor degradation and ϵ is the error, termed the "separability error", which would remain small.

Separability is clearly expected for small amounts of degradation applied to the fill when one considers the Taylor series expansion of the effect of fill performance changes to the NDWCT T_{wo}:

$$\begin{aligned}\Delta T_{wo} = &\frac{\partial T_{wo}}{\partial Me_{fi}}(Me_{fi} - Me_{fi,0}) + \frac{\partial T_{wo}}{\partial K_{fd}}(K_{fd} - K_{fd,0}) \\ &+ \frac{1}{2}\frac{\partial^2 T_{wo}}{\partial {Me_{fi}}^2}(Me_{fi} - Me_{fi,0})^2 \\ &+ \frac{\partial^2 T_{wo}}{\partial Me_{fi}\partial K_{fd}}(Me_{fi} - Me_{fi,0})(K_{fd} - K_{fd,0}) \\ &+ \frac{1}{2}\frac{\partial^2 T_{wo}}{\partial {K_{fd}}^2}(K_{fd} - K_{fd,0})^2 + \frac{1}{6}\frac{\partial^3 T_{wo}}{\partial {Me_{fi}}^3}(Me_{fi} - Me_{fi,0})^3 \\ &+ \frac{1}{2}\frac{\partial^3 T_{wo}}{\partial {Me_{fi}}^2\partial K_{fd}}(Me_{fi} - Me_{fi,0})^2(K_{fd} - K_{fd,0}) \\ &+ \frac{1}{2}\frac{\partial^3 T_{wo}}{\partial Me_{fi}\partial {K_{fd}}^2}(Me_{fi} - Me_{fi,0})(K_{fd} - K_{fd,0})^2 \\ &+ \frac{1}{6}\frac{\partial^3 T_{wo}}{\partial {K_{fd}}^3}(K_{fd} - K_{fd,0})^3 + ...\end{aligned} \tag{6.2}$$

where all partial derivatives are taken at $(Me_{fi,0}, K_{fd,0})$ with 0 denoting the unfouled condition and:

$$\Delta T_{wo} = T_{wo,fouled}(Me_{fi}, K_{fd}) - T_{wo,0}(Me_{fi,0}, K_{fd,0}) \tag{6.3}$$

The Taylor series consist of terms which are either unmixed (functions of either Me_{fi} or K_{fd}) or mixed (functions of both Me_{fi} and K_{fd}). For small degradations, applied as $(Me_{fi} - Me_{fi,0})$ or $(K_{fd} - K_{fd,0})$, the first-order terms, which are both unmixed, should dominate compared to the higher-order terms, since the small degradations are multiplied together (or raised to powers 2 and above) in the higher order terms.

If the separability error remains small, even for very large amounts of thermal and hydraulic degradation of the fill, it would allow the treatment of thermal and hydraulic fill degradation as features which can be individually characterised and studied. The feasibility of this is studied next using Monte Carlo methods.

Monte Carlo methods are the computerised generation of random objects or processes from certain probability distributions (Kroese *et al.*, 2014). While there are many applications of Monte Carlo methods, the one utilised in this study is statistical inference of deterministic processes.

Monte Carlo methods are used to analyse the relative magnitude of ϵ across large ranges of NDWCT, atmospheric, fill and fill degradation inputs. The aim of this analysis is only to show that the expected error, when considering fill fouling as separate thermal and hydraulic effects, is small. As a result, the exact or estimated industry-wide distributions of the input variables are not important. It is only aimed to show that in the ranges deemed possible, the

error is indeed small.

6.2.2 Analysis inputs

The analysis consists of a large sample of NDWCT performance prediction calculations with all inputs being randomly varied across large ranges with uniform distributions. The criteria for the input ranges were not strictly determined; ranges of input variables are selected as values that are deemed possible. Some consideration is given to solution stability in the input range selection, with some input ranges creating a greater propensity to solution failures, e.g. a small difference between T_a and T_{wi}. No consideration is given to whether a specific layout is a practical design, or structurally sound. Figure 6.1 provides the ranges for all NDWCT, atmospheric, fill and degradation input variables. Degradation inputs scale the fill Merkel number (decrease) and pressure loss factor (increase) characteristic equations.

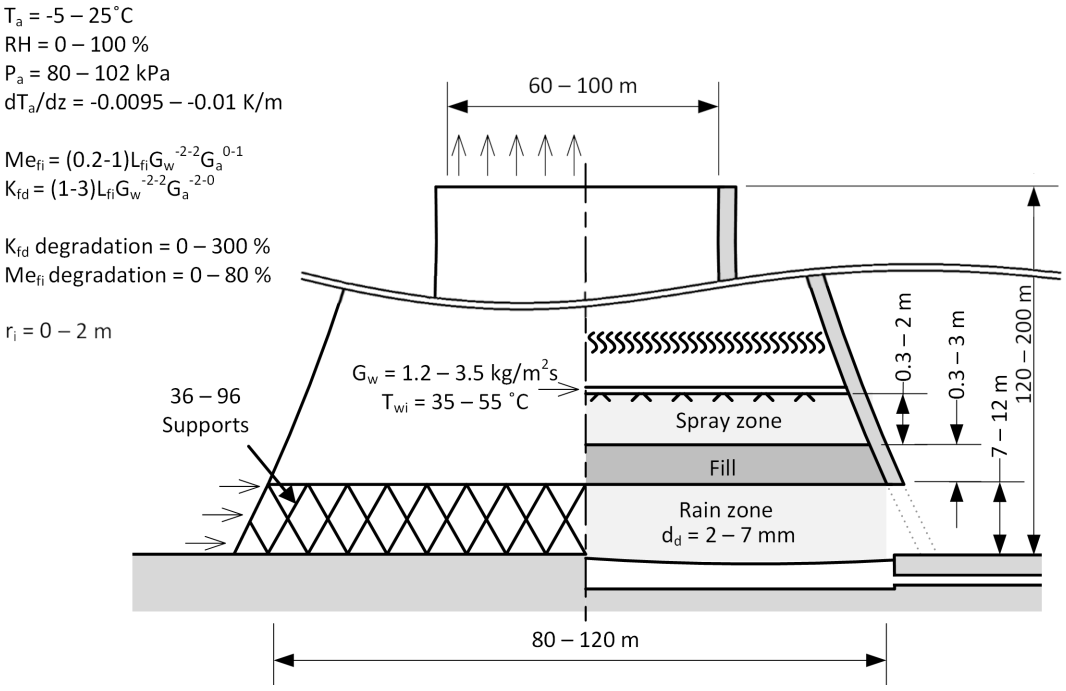

Figure 6.1: Monte Carlo analysis input ranges

Due to the wide ranges of input parameters required for the Monte Carlo analysis, applicability ranges of the NDWCT performance prediction equations, such as those in Section 2.2.1.4, could not be adhered to in all cases. This is not expected to affect the result of the analysis significantly, as it only applies to small portions of the overall NDWCT performance prediction calculations.

6.2.3 Random number generation

Computer programs can not truly generate random numbers and instead rely on algorithms generating pseudorandom numbers: numbers that appear to be

random, but are in reality deterministic. For the current study, pseudorandom numbers are generated by the Python 3.7 implementation of the popular algorithm known as the "Mersenne Twister" (see Kroese *et al.* (2011)). The period length of a random number generator is the minimum number of steps before the generator returns to a previously reached state. The period length of the Mersenne Twister is $2^{19937} - 1$, making it more than sufficiently random for the current study, which requires only approximately 2^{21} (sample size $\times$ number of input variables) random numbers.

6.2.4 Analysis results and discussion

The sample size (number of different NDWCT performance prediction calculations) analysed using this method is 50 000, including 109 (0.22%) calculation failures. Convergence is indicated, as in Gentle (2009) by the "almost sure" convergence criteria, which states that:

$$\frac{1}{N}\sum_{i=1}^{N} g(X_i) \rightarrow E(g(X)) \tag{6.4}$$

almost surely as N goes to infinity, where E denotes the "estimate" of $g(X)$. The function g is an arbitrary function of the input x. For the current analysis, g calculates the "relative separability error" ($\epsilon/\Delta T_{wo}$) using the NDWCT performance prediction calculation. X denotes the independent and identically distributed inputs of the population, while X_i denotes a specific instance of the independent and identically distributed inputs in the sample. Convergence is displayed visually in Figure 6.2, with the estimate of the relative separability error:

$$E(\epsilon/\Delta T_{wo}) = 0.00309 \tag{6.5}$$

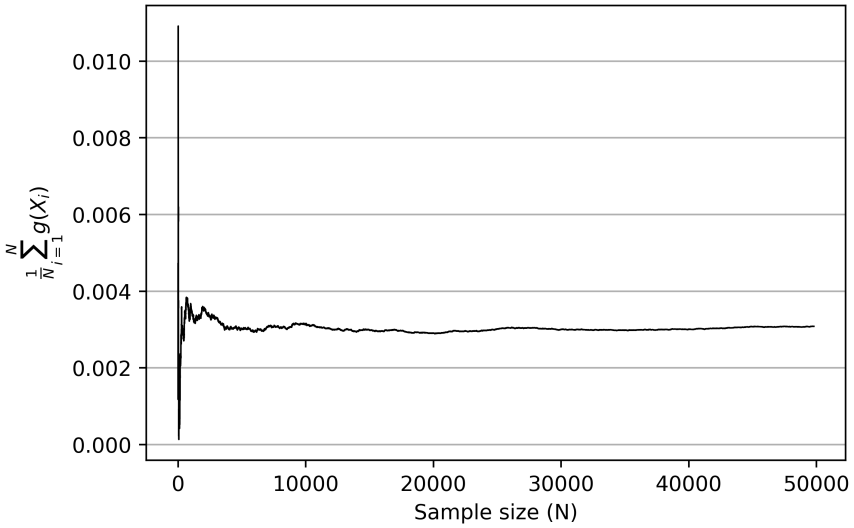

Figure 6.2: Convergence of the relative separability error

Figure 6.3a shows a normalised (scaled to have an area of 1) histogram of the relative separability error ($\epsilon/\Delta T_{wo}$), showing the majority of cases concentrated at very small relative separability errors, within approximately $\pm 2.5\%$. It is found that the probability density function (PDF) of the t-distribution (see Kroese *et al.* (2011)) provides a reasonable fit of the histogram data. Figure 6.3b shows the empirical cumulative density function (ECDF), defined by Gentle (2009) as:

$$P_N(x) = \frac{|\{x_i | x_i \leq x\}|}{N} \tag{6.6}$$

of the Monte Carlo analysis, with sample size N. Also included is the cumulative density function (CDF), defined by Kroese *et al.* (2011) for continuous functions as:

$$F_c(x) = \int_{-\infty}^{x} f(u)du \tag{6.7}$$

for a PDF f, of the t-distribution. The smoothness of the ECDF, along with the slight errors in the fit of the t-distribution, means that a distribution fit of the data is not necessary and the ECDF is thus used as is: according to Gentle (2009), the ECDF can be used as an "estimator of the corresponding population function".

From the ECDF it can be stated, for example, that $-0.0226 \leq \epsilon/\Delta T_{wo} \leq 0.0437$ for 95% of the population. The absolute relative separability error ($|\epsilon/\Delta T_{wo}|$) is also of interest, since it can be used to make simpler statements on the magnitude of the error and it is plotted in Figure 6.4. From this, it can be stated that $|\epsilon/\Delta T_{wo}| \leq 0.0342$ for 95% of population. Similarly, $|\epsilon/\Delta T_{wo}| \leq 0.05$ for 97.4% of the population. Additionally, it is observed that the value of ΔT_{wo} ranges from 0 °C to 17.36 °C, indicating that a large range of fouling performance effects are covered by this analysis. The maximum value of $|\epsilon/\Delta T_{wo}|$ is 0.226.

Scatter plots of the Me_{fi} (Figure 6.5a) and K_{fd} (Figure 6.5b) degradation against $|\epsilon/\Delta T_{wo}|$ of all cases in the Monte Carlo analysis show that there is greater likelihood for larger values of $|\epsilon/\Delta T_{wo}|$ to occur at greater values of Me_{fi} and K_{fd} degradation. There also appears to be a lower bound, sloping linearly, with the amount of Me_{fi} degradation governing the possible magnitude of the separability error for this population. This may indicate a fundamental relationship between these parameters.

In conclusion: the errors made when modelling NDWCT fill fouling as individual thermal and hydraulic degradation effects, are small in the overwhelming majority of cases. This effect is so statistically significant, for a wide range of inputs and large amounts of thermal and hydraulic degradation, that it is considered sufficient to state, with only small errors, that:

$$\Delta T_{wo} = \Delta T_{wo,Me} + \Delta T_{wo,K_{fd}} \tag{6.8}$$

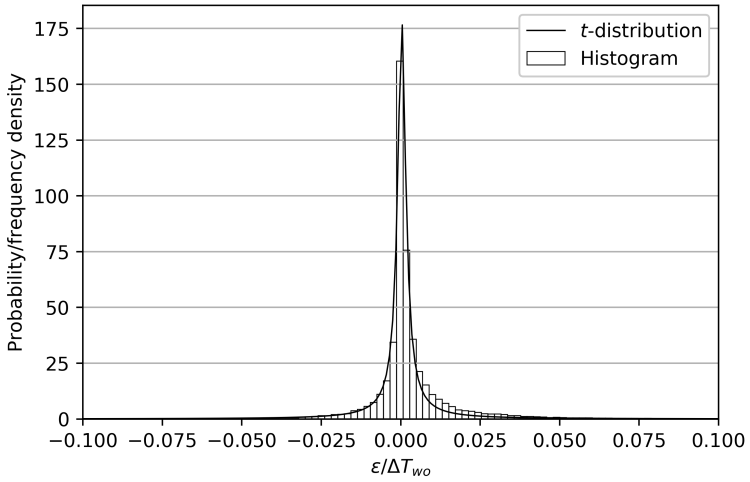

(a) Histogram of relative separability

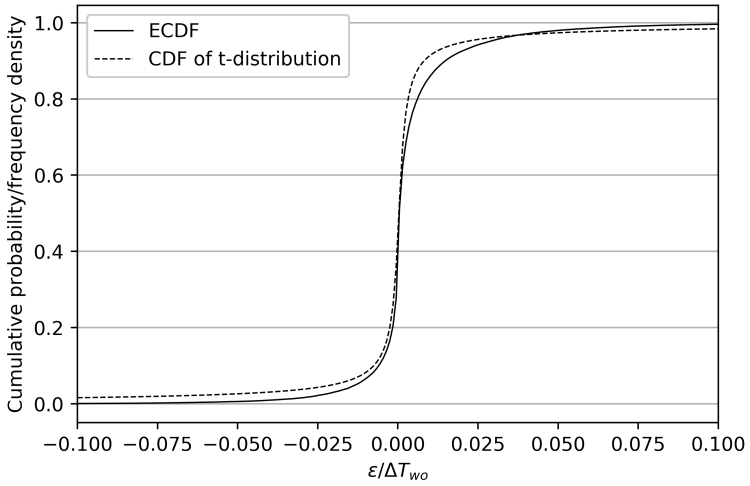

(b) ECDF of relative separability error

Figure 6.3: Separability error probability

6.3 Fill fouling factors and uncertainty analysis

Separability of thermal and hydraulic fill fouling effects leads to the individual quantification of fill thermal and hydraulic degradation effects through the use of fouling factors. It is proposed that fouling factors are applied to the fill performance characteristic equations. These fouling factors are time-dependent and change the thermal and hydraulic characteristics of the fill over time. Fouling factors, along with the unfouled fill performance characteristics can be applied to NDWCT performance prediction calculations to perform the calculations at any selected time after fill installation, thereby allowing lifecycle cost analysis of fills installed in NDWCTs. Separability is not strictly required to allow the application of fouling factors, but it does mean that error and uncertainties in measurements or predictions made for one fill performance

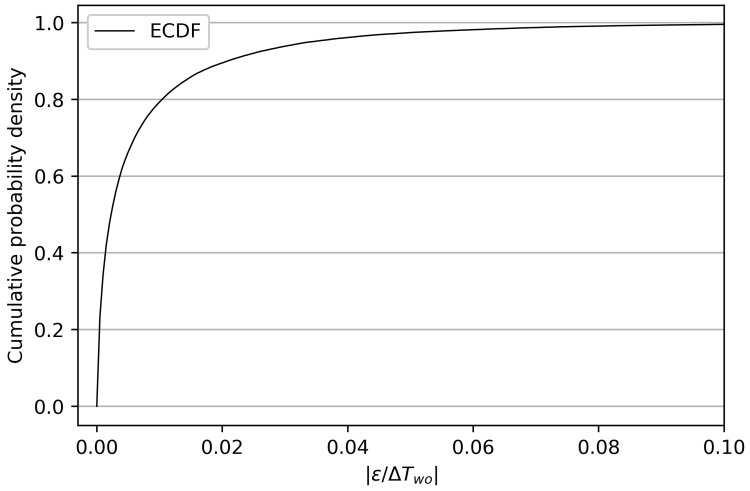

Figure 6.4: ECDF of absolute relative separability error

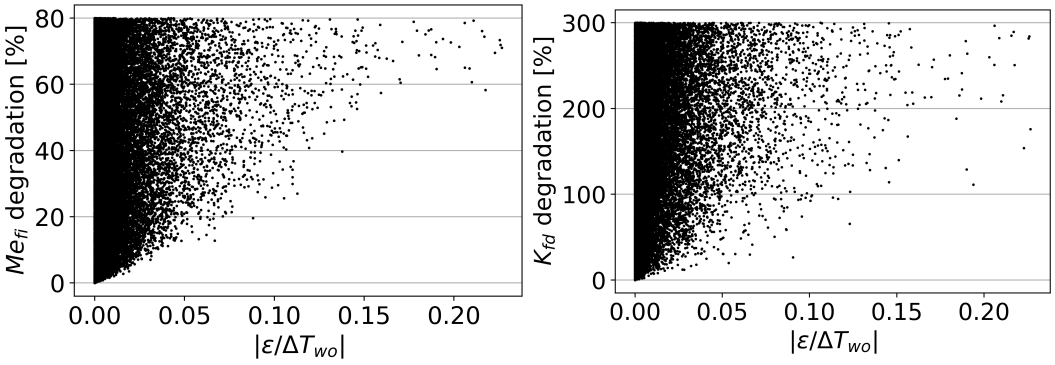

(a) Thermal degradation

(b) Hydraulic degradation

Figure 6.5: Scatter plots of degradations and absolute relative separability errors

parameter has a negligible effect on the other parameter.

The simplest form of these fouling factors scale the characteristic equations:

$$Me_{fi}(t) = (1 - f_m(t))a_m G_w^{b_m} G_a^{c_m} \tag{6.9}$$

$$K_{fd}(t) = (1 + f_k(t))a_k G_w^{b_k} G_a^{c_k} \tag{6.10}$$

where $f_m(t)$ is the thermal fouling factor, $f_k(t)$ is the hydraulic fouling factor and $f_m(0) = f_k(0) = 0$. The fill fouling factors at a specific time (t) after the initial test (0) can be determined by performing a least-squares regressions on the test data of the specific fill performance test at time t to determine $f_m(t)$ and $f_k(t)$ in Equations 6.9 and 6.10. Unlike the widely-used sensible heat transfer fouling factors, which represent the thermal resistance of a physical layer of material on the heat transfer surface (see Cengel (2006)), fill fouling factors have no physical interpretation and is based purely on empirical data.

With the fouling factor being a value obtained by regression of the performance

test results, the fill fouling factor uncertainty is calculated using Equation 5.12, with the adaptation that the regression output (Y) is replaced by the fill fouling factor (f).

$$\begin{aligned} u_f^2 = & \sum_{i=1}^{N} \left(\frac{\partial f}{\partial Y_i}\right)^2 b_{Y_i}^2 + 2\sum_{i=1}^{N-1}\sum_{k=i+1}^{N} \left(\frac{\partial f}{\partial Y_i}\right)\left(\frac{\partial f}{\partial Y_k}\right) b_{Y_i Y_k} \\ & + \sum_{i=1}^{N} \left(\frac{\partial f}{\partial G_{w_i}}\right)^2 b_{G_{w_i}}^2 + 2\sum_{i=1}^{N-1}\sum_{k=i+1}^{N} \left(\frac{\partial f}{\partial G_{w_i}}\right)\left(\frac{\partial f}{\partial G_{w_k}}\right) b_{G_{w_i} G_{w_k}} \\ & + 2\sum_{i=1}^{N}\sum_{k=1}^{N} \left(\frac{\partial f}{\partial G_{w_i}}\right)\left(\frac{\partial f}{\partial Y_k}\right) b_{G_{w_i} Y_k} + \sum_{i=1}^{N} \left(\frac{\partial f}{\partial G_{a_i}}\right)^2 b_{G_{a_i}}^2 \\ & + 2\sum_{i=1}^{N-1}\sum_{k=i+1}^{N} \left(\frac{\partial f}{\partial G_{a_i}}\right)\left(\frac{\partial f}{\partial G_{a_k}}\right) b_{G_{a_i} G_{a_k}} \\ & + 2\sum_{i=1}^{N}\sum_{k=1}^{N} \left(\frac{\partial f}{\partial G_{a_i}}\right)\left(\frac{\partial f}{\partial Y_k}\right) b_{G_{a_i} Y_k} \\ & + 2\sum_{i=1}^{N}\sum_{k=1}^{N} \left(\frac{\partial f}{\partial G_{w_i}}\right)\left(\frac{\partial f}{\partial G_{a_k}}\right) b_{G_{w_i} G_{a_k}} + \sum_{i=1}^{N} \left(\frac{\partial f}{\partial Y_i}\right)^2 s_{Y_i}^2 \\ & + \sum_{i=1}^{N} \left(\frac{\partial f}{\partial G_{w_i}}\right)^2 s_{G_{w_i}}^2 + \sum_{i=1}^{N} \left(\frac{\partial f}{\partial G_{a_i}}\right)^2 s_{G_{a_i}}^2 \end{aligned} \tag{6.11}$$

where f may be replaced by f_m and f_k and Y may be replaced by the corrected results Me_{fi} and K_{fd} respectively to calculate u_{f_m} and u_{f_k}.

The uncertainty in the NDWCT performance, when using fouling factors, is calculated as an adapted form of Equation 5.18:

$${u_P}^2 = \left(\frac{\partial P}{\partial f_m} u_{f_m}\right)^2 + \left(\frac{\partial P}{\partial f_k} u_{f_k}\right)^2 \tag{6.12}$$

where $\frac{\partial P}{\partial f_m}$ and $\frac{\partial P}{\partial f_k}$ are calculated numerically using the NDWCT performance prediction calculation. As in Section 5.5, correlated uncertainties are neglected as the fouling factors have low sensitivities to individual measurement values.

Appendix F.1 contains a sample calculation of NDWCT performance prediction, including uncertainty calculations, using fill thermal and hydraulic fouling factors. The calculation is done using the same fill test data in Appendix C and NDWCT design details in Appendix D. This allows comparison of the NDWCT performance calculations done using the traditional method of fill performance characteristic equations with fill performance quantified using fouling factors. The results of this comparison, including uncertainties, are provided in Table 6.1. The water outlet temperature for the unfouled condition is provided for reference.

Table 6.1: NDWCT T_{wo} predictions using the traditional method and fouling factors

Condition	$\mathbf{T_{wo}}$ [°C]	$\mathbf{u_{T_{wo}}}$ [°C]
Unfouled	21.929	-
Fouled (traditional method)	21.444	0.347
Fouled (fouling factors)	21.565	0.356

The predicted NDWCT water outlet temperature calculated using fill fouling factors compares reasonably well with the traditional method. The difference in the prediction is largely due to the inaccuracy introduced when calculating the fouling factors via regression, which will always have a less accurate fit than the normal regression of fill performance characteristic equations. The calculated uncertainty in the NDWCT water outlet temperature of the two cases also compare well, with the value calculated using fouling factors being slightly higher due to the less accurate fit of the fouling factors to the test data.

Although reasonable accuracy of NDWCT performance is obtained in the example calculations, the change in fill performance witnessed here is not representative of large fill fouling degradations possible in the industry and testing of the viability of these methods on moderately and heavily fouled fills is encouraged. The calculation results show an improvement (as opposed to the expected degradation) in fill performance in the fouled condition. This is not entirely unexpected, since a slight (up to 10%) Merkel number increase was also reported by Whittemore and Massey (1992) in the initial months of long-term fill fouling testing.

6.4 Fill lifecycle calculations using fill fouling factors

Fill lifecycle calculation using time dependent fouling factors may be used to financially compare the performance of fills. Tested or predicted fill fouling factors can be used to calculate the expected performance at various times over the fill's life. The exact calculation method of applying the expected performance to lifecycle cost calculations will depend on the information available for the specific power plant: a typical approach, adapted from Jestin *et al.* (2017), is presented here.

It is common for annual weather data to be available, but this reduces the resolution at which the changes in fill performance may be taken into account. Weather data at shorter intervals, such as quarterly or monthly, will lead to greater accuracy of calculation, although other information, such as the exact fill installation date and planned outage dates then become more important to take into account.

Power plants do not operate at full load for their entire lives, but are shut

down at regular intervals for maintenance, may have to operate at part load depending on the requirement of the power system within which they operate, or may have their output limited due to load losses (unrelated to the cooling system). Exact consideration of such instances in a lifecycle calculation is impossible since all of these can't be predicted with much certainty far into the future. A "load factor" is therefore introduced as:

$$f_L = \frac{\text{expected electrical energy produced [MJ]}}{\text{electrical energy produced at full load [MJ]}} \tag{6.13}$$

Not all fuel used in the boiler is converted into heat addition in the Rankine cycle, with some heat being lost through the boiler walls, and some heat remaining in the boiler exhaust air exiting to the atmosphere. The boiler efficiency (η_{boil}) therefore needs to be taken into account. The hourly fuel cost for a specific weather data entry and fouling factors combination is calculated as:

$$C_h = \frac{c_{fuel} f_L P_{full} HR}{CV\ \eta_{boil}} \tag{6.14}$$

where the fuel cost per mass (c_{fuel}) is in a unit such as South African Rand per kilogram (R/kg) and the specific energy content of the fuel (also known as calorific value, CV) has the unit kJ/kg. The heat rate (HR) for each analysis period is calculated according to Section 2.3 with fouling factors (for that specific period) applied to both the thermal and hydraulic performance characteristic equations of the fill. The fuel cost for the entire analysis period is calculated as:

$$C_t = C_h\ t \tag{6.15}$$

where t denotes the analysis period duration in hours. The total lifecycle cost of the installed fill is calculated as the sum of the fuel costs of all analysis periods:

$$C = \sum_{i=1}^{I} C_{t_i} \tag{6.16}$$

for I analysis periods. All values are calculated at a fixed fuel cost (such as the current fuel cost), providing a fair comparison between various fills. Variable cost models may be used for greater accuracy, while increasing the calculation complexity.

Since the current study includes only a relatively short testing period, Appendix F.2 shows an example lifecycle calculation using an assumed progression of fill fouling factors based on test data from Whittemore and Massey (1992). Extrapolation of the data generated in the current study to a full NDWCT lifecycle is not considered here. Appendix F.2 serves simply as an example of how this data would be applied.

6.5 Shortcomings

This method requires fill thermal and hydraulic performance testing over long periods of time over the full range of air- and water mass fluxes, requiring advanced equipment and instrumentation operating over many months or even years. Most limiting, it is generally believed that fill fouling is location-specific (see Section 3.7), meaning that the long-duration and relatively expensive testing can only be used for a single location.

The accuracy of the NDWCT performance prediction calculations is affected by the accuracy of the fill fouling factor fit. More complex fouling factors, for example scaling the performance characteristic exponents, may be employed to reduce the error caused by poor fits. Increasingly complex fouling factors will reduce the intuitive understanding of the fouling factors (that they scale the thermal and hydraulic fill performance) and increase the complexity of calculating the fouling factors' uncertainty and propagated effects.

6.6 Conclusion

It is demonstrated that NDWCT fill fouling may generally be viewed as separable thermal and hydraulic effects. A method is proposed to quantify fill fouling as scaling of the unfouled fill thermal and hydraulic fouling characteristic equations using fouling factors. This method can be used to perform fill lifecycle cost analysis using fill fouling test results (conducted over a suitably long duration), allowing fair comparison between competing fill designs in terms of fouling performance.

Chapter 7: Results

This chapter presents the results obtained from the fill fouling test facility. The measured fill performance from fill performance testing is presented first, followed by the visual inspections and mass measurements. Links are established between the visual inspections and measured mass gains, but due to problems experienced with the thermal performance measurement results, no attempt is made to link with the measured performance.

7.1 Fill performance tests

7.1.1 Introduction

The following subsections contain a summary of the fill fouling test data as measured throughout the testing period. Both the thermal and hydraulic fouling factors for the weekly fill performance tests, including uncertainty, are presented graphically. The predicted T_{wo} of a NDWCT having the same design properties and atmospheric conditions as in Appendix D, but using results of individual weekly fill performance test are also presented. To validate the use of fill fouling factors, the values of T_{wo} calculated using fill fouling factors are compared to those when using the traditional fill performance characteristic equations for the specific performance tests.

7.1.2 Test section 1

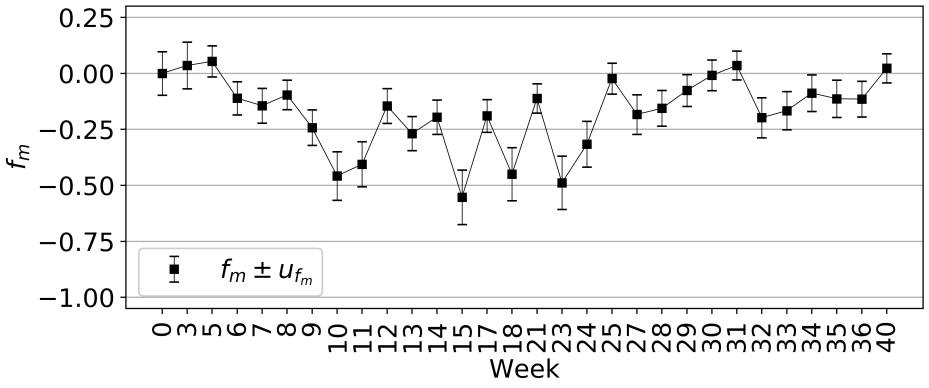

(a) Thermal fouling factor and uncertainty

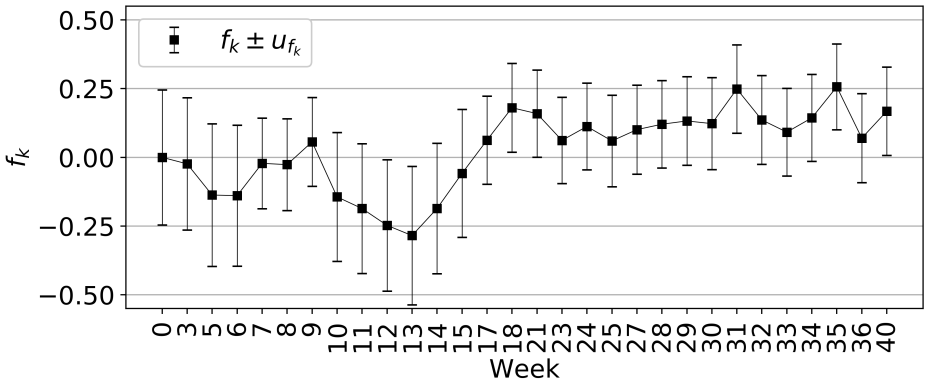

(b) Hydraulic fouling factor and uncertainty

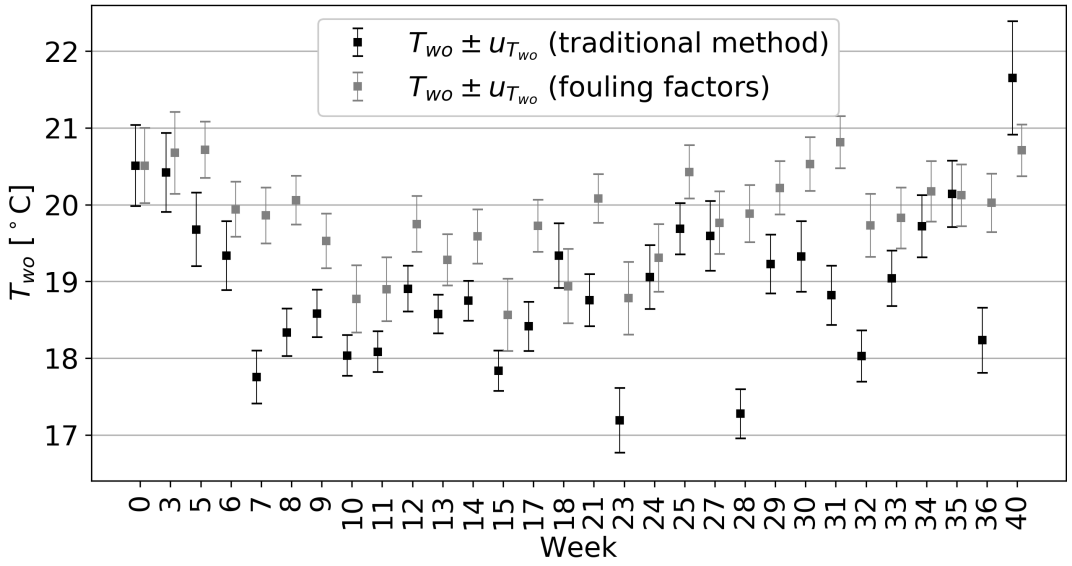

(c) NDWCT T_{wo} comparison

Figure 7.1: Performance measurements of Test section 1

7.1.3 Test section 2

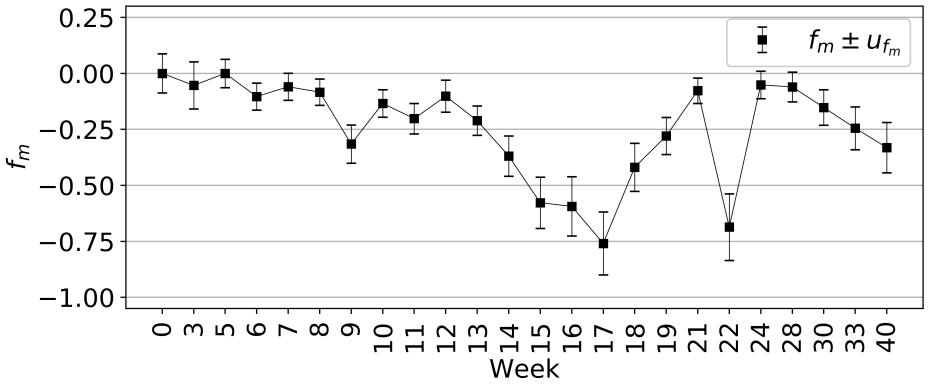

(a) Thermal fouling factor and uncertainty

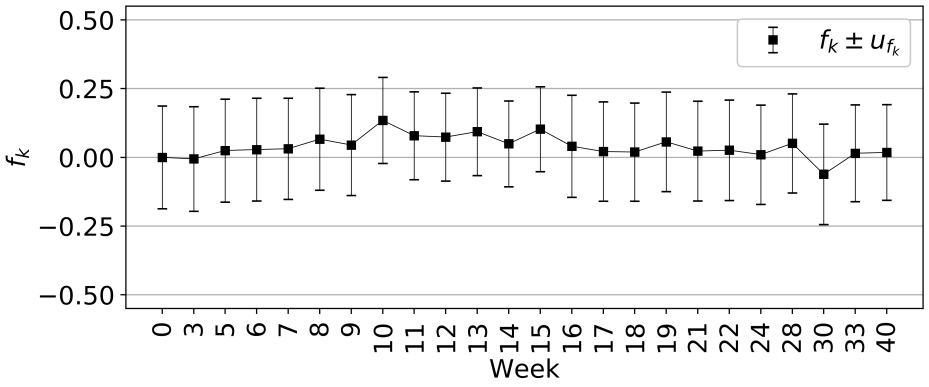

(b) Hydraulic fouling factor and uncertainty

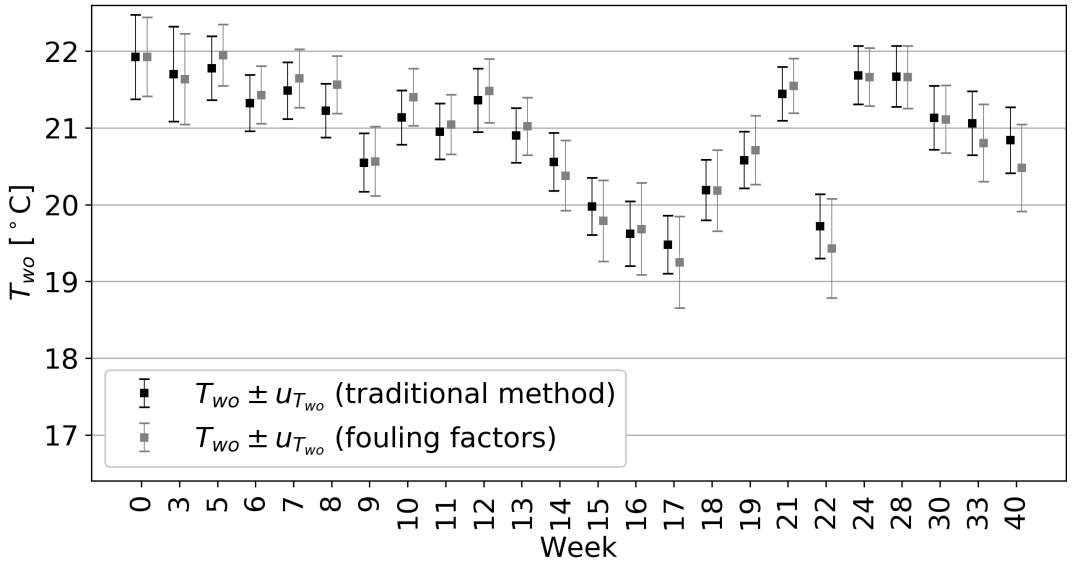

(c) NDWCT T_{wo} comparison

Figure 7.2: Performance measurements of Test section 2

7.1.4 Test section 3

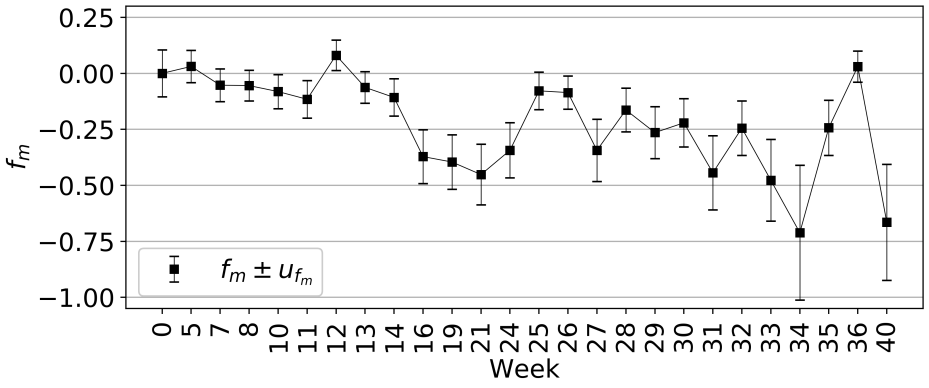

(a) Thermal fouling factor and uncertainty

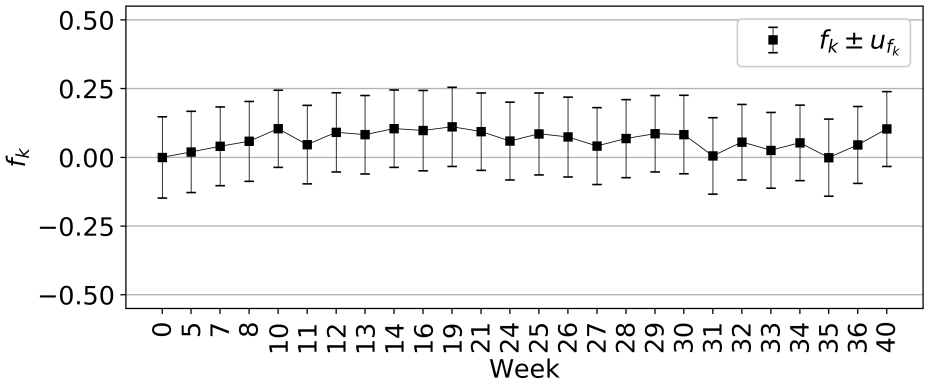

(b) Hydraulic fouling factor and uncertainty

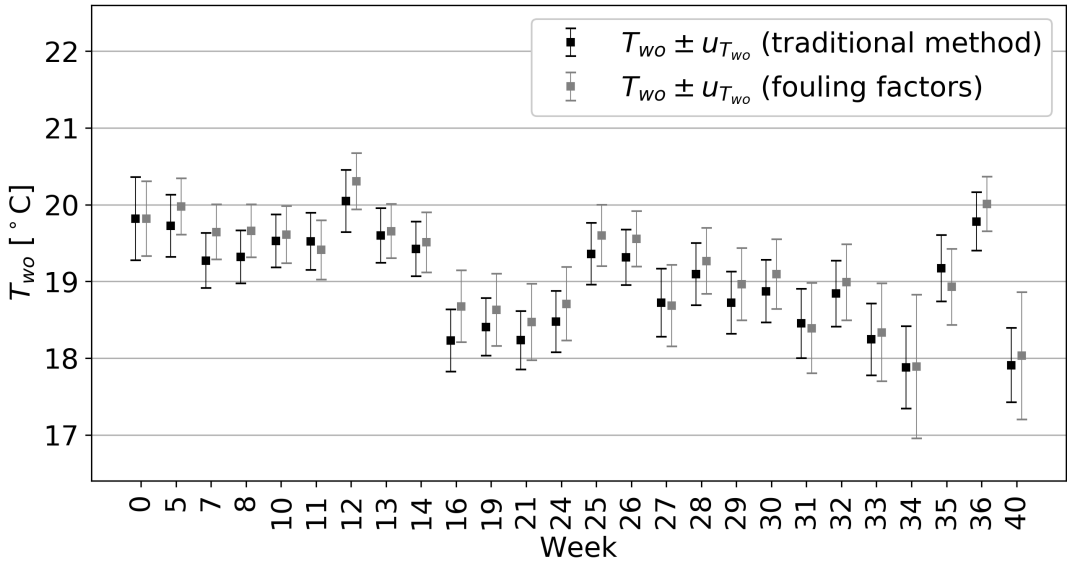

(c) NDWCT T_{wo} comparison

Figure 7.3: Performance measurements of Test section 3

7.1.5 Test section 4

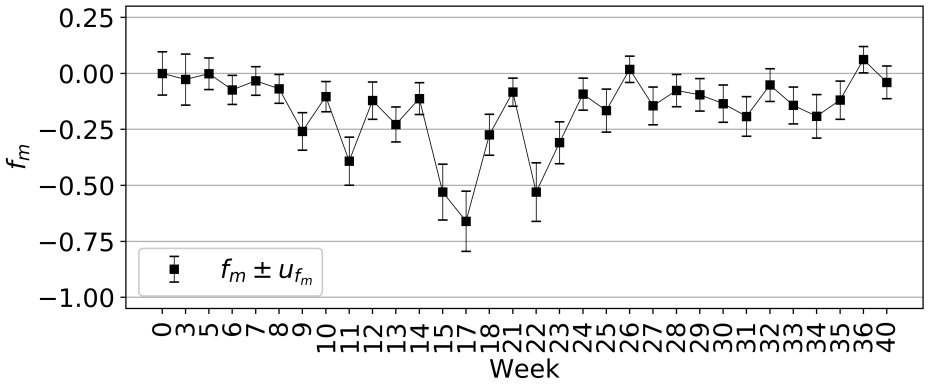

(a) Thermal fouling factor and uncertainty

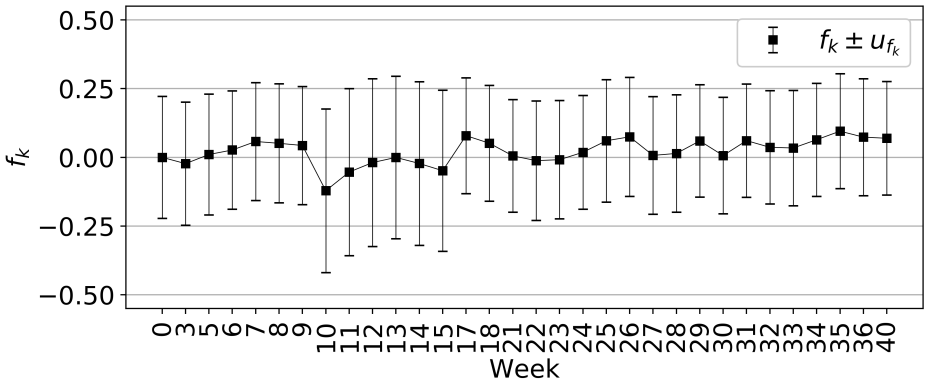

(b) Hydraulic fouling factor and uncertainty

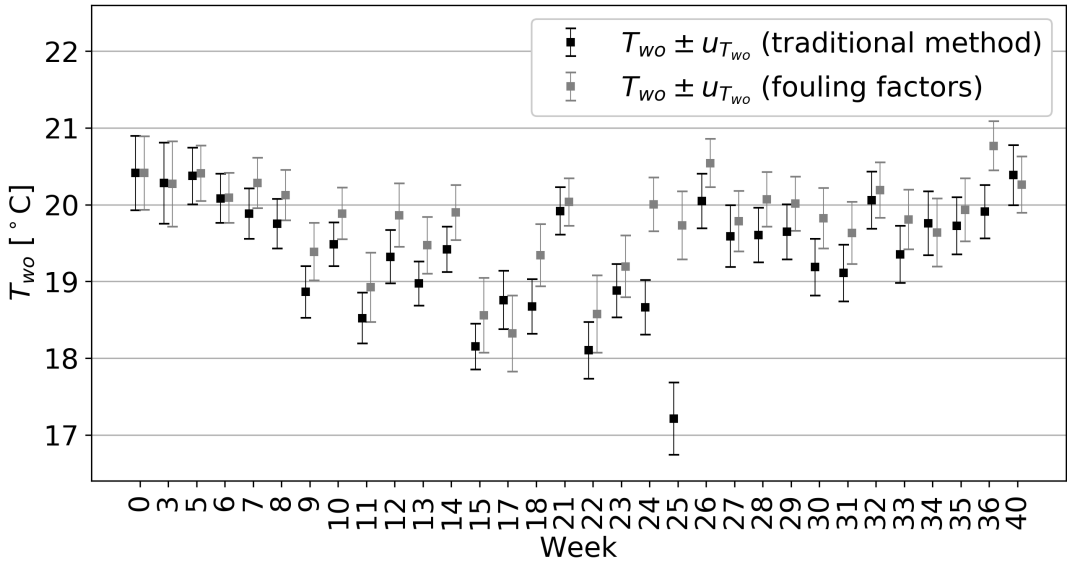

(c) NDWCT T_{wo} comparison

Figure 7.4: Performance measurements of Test section 4

7.1.6 Discussion

No clear fouling behaviour could be observed from the fouling factors of the four fill samples. This is partly due to the low-fouling behaviour (as claimed by the fill manufacturers) of the tested fill samples, combined with the relatively short testing duration, and partly due to the problems experienced with testing, which are explained in the following subsections.

7.1.6.1 Thermal performance

The fill thermal fouling performance testing was not successful. The erratic behaviour of the thermal fouling factor, as seen in Figures 7.1a through 7.4a, especially during the middle period of the testing duration, indicates testing errors. This has been investigated and attempts to link this to ambient (T_{db}, T_{wb}, relative humidity and wind velocity) and operating (T_{wi}) conditions have failed, with no link being observed.

Test section 1 performed the worst of the four test sections, with most of its performance tests showing very erratic data. This can be seen in the large differences between the NDWCT T_{wo} calculated using the traditional method and the fouling factor method, compared to the other test sections. This is suspected to be due to a greater tendency of the pre-nozzle pressure measurement tap on Test section 1 to block with water. The blockages create fluctuations in the sensed pressure, affecting both the calculation of the nozzle inlet fluid properties and the pressure difference across the nozzle (see Figure 4.2 for the layout). This in turn causes the fan speed to fluctuated as the speed is adjusted to control the value of G_a. Figure 7.5 shows the erratic behaviour of some of the measured parameters.

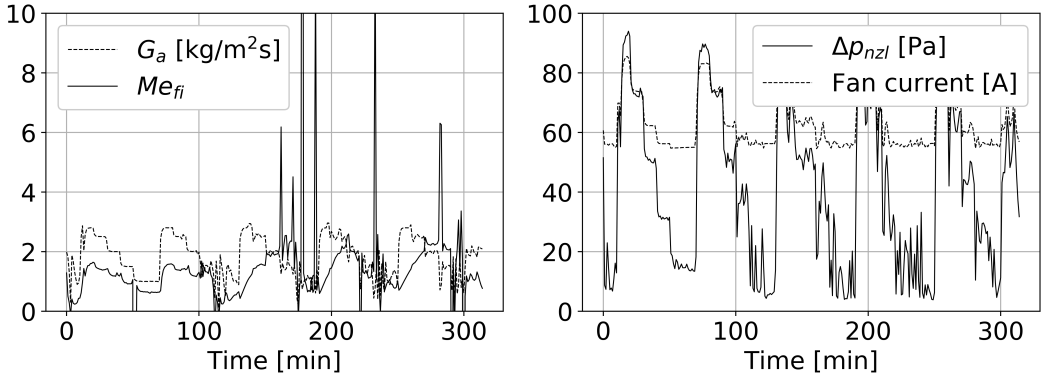

(a) (b)

Figure 7.5: Erratic behaviour of measured data during fill performance test

Test sections 2, 3 and 4 showed better behaviour than Test section 1, although not in all cases. The negative values of f_m observed, which are largest during the middle of the testing period, indicate a significant thermal performance improvement. While some of this performance improvement may be attributable

to fill aging (see Section 3.2.1), the large value of up to 70% increase indicates an error in the measurements. A possible cause of this is the poor cleanliness of the cotton wick which is used to wet the wet-bulb temperature measurement RTD, with the poor cleanliness caused by the use of cooling water in the dry-bulb/wet-bulb station. This was only observed by the contractor around week 26 of testing, after which the cotton wicks were replaced regularly, typically before performance testing. The value of f_m returned to near zero, especially for test section 4, while other test sections still had somewhat negative thermal fouling factors after this. Unfortunately, the fact that testing has been suspended (see Section 4.2.1) means that operational fault-finding to correct all thermal performance measurement errors is not possible.

7.1.6.2 Hydraulic performance

The hydraulic fouling performance testing has been successful, with f_k for all test sections trending around zero or slightly positive for the majority of the testing period (see Figures 7.1b through 7.4b). The small values of f_k indicate low amounts of fouling, which is to be expected for the low-fouling fill samples installed and the short duration of testing. Fill sample visual inspections also show low amounts of fouling, as discussed in Section 7.2. The relatively large uncertainty of the hydraulic fouling factor is mostly due to the large uncertainty associated with the fill pressure difference sensor compared to the measured value.

7.1.6.3 NDWCT performance

With the better behaved data of Test sections 2, 3 and 4 (Figures 7.2c, 7.3c and 7.4c respectively), the values of T_{wo} in each case indicate that the calculation of NDWCT performance using fill fouling factors is usually a good approach. The value of the NDWCT T_{wo} predicted using fouling factors is within 0.5 °C of that predicted by the traditional method in most cases. While this is not extremely accurate, it is expected that improvements in the testing techniques will yield increased accuracy of these predicted values.

7.1.6.4 Uncertainty analysis

The uncertainty analysis is considered a success despite the testing problems encountered. The fact that the NDWCT T_{wo} uncertainties of the initial testing (week 0) are approximately equal for the traditional and fouling factor methods indicate that the fouling factor uncertainty calculation is done correctly. The minor differences seen between these values may be due to the inherent errors in numerical differentiation or the small effects of neglecting correlated uncertainties. It is expected that this method of uncertainty analysis will yield steady and predictable results when the testing errors have been rectified.

7.2 Visual inspections

7.2.1 Introduction

A summary of visual inspections of fill samples after 4 months of operation is provided below. Note that the fills are assigned letters A through D, which do not necessarily correspond with the test section numbering 1 through 4. This is done to avoid matching of fill designs to measured fill performance and potentially infringing on fill suppliers' rights to fair assessment of their products' performance during tender evaluations.

The visual inspections did not form part of any formal inspection process (such as in Section 3.6.2). In each case it consisted of partial disassembly of the fill and photographing the fill's overall fouling state as well as areas where fouling was most prominent for the specific fill.

7.2.2 Fill sample A

Fill sample A is a trickle fill with largely straight flute-like structures. Although this fill had gained significant mass by the time of the visual inspection (day 125 in Figure 7.7a), surprisingly little fouling was observed visually, with only small amounts of what appeared to be particulate fouling. Upon disassembly of individual plastic layers of the fill, it was found that a relatively large amount of particulate matter was stuck in the areas where the different layers make contact, as seen in Figure 7.6a.

7.2.3 Fill sample B

Fill sample B is a trickle fill with flute structures sloping at an angle to the vertical. The visual inspection showed a large portion of surface area in this fill covered with a mixture of biological and particulate deposits (see Figure 7.6b). Small amounts of mud were present on the test section walls. Visually, this appears to be the worst fouling fill sample.

7.2.4 Fill sample C

Fill sample C is a modular splash fill. Very little fouling was observed on this fill, with only a thin layer of mud noticed in some areas on the main fill structure. A vertical "shaft" of particulate fouling is visible where two fill modules are in contact, as seen in Figure 7.6c. Visually, this fill sample appears to have the least amount of fouling.

7.2.5 Fill sample D

Fill sample D is a film fill with vertical flutes, manufactured using uncorrugated sheets, which are pierced across a large portion of their surface area. Figure 7.6d shows a thin deposit layer across the fill surface, which has been swabbed clean in the center, indicating that a thin fouling layer is present. A high chlorophyll A concentration in the swabbed sample indicates that this is an

algal biofilm. The collection of particulate fouling deposits near the test section door was observed, possibly where the fill had been in contact with the door.

(a) Fill sample A

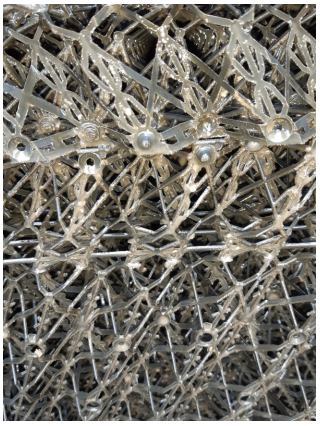

(b) Fill sample B

(c) Fill sample C

(d) Fill sample D

Figure 7.6: Fouling evident on fill samples

7.3 Measured fill mass

The results of the daily drip-dry mass measurements (see Section 4.2.3.6) are presented in Figure 7.7, using the same fill lettering as in Section 7.2. The occasional dips in the measured masses, such as Figure 7.7d around days 85 and 135 are periods when the test section was not in service and the fill dried more completely. A reduction in fill mass is observed after longer shutdowns, such as after the three-day shutdown around day 150 to replace a faulty compressor.

The initial period of testing, up to 50 days had frequent shutdowns to repair faulty equipment, resulting in more erratic mass measurement data on all four test sections. The period in Figure 7.7b after day 50 where a lower mass is consistently measured was a period where one of the three load cells had failed. The load cell was repaired around day 100. For the period between days 260

and 282 the NDWCT providing water to the test facility was out of service and the fill dried completely.

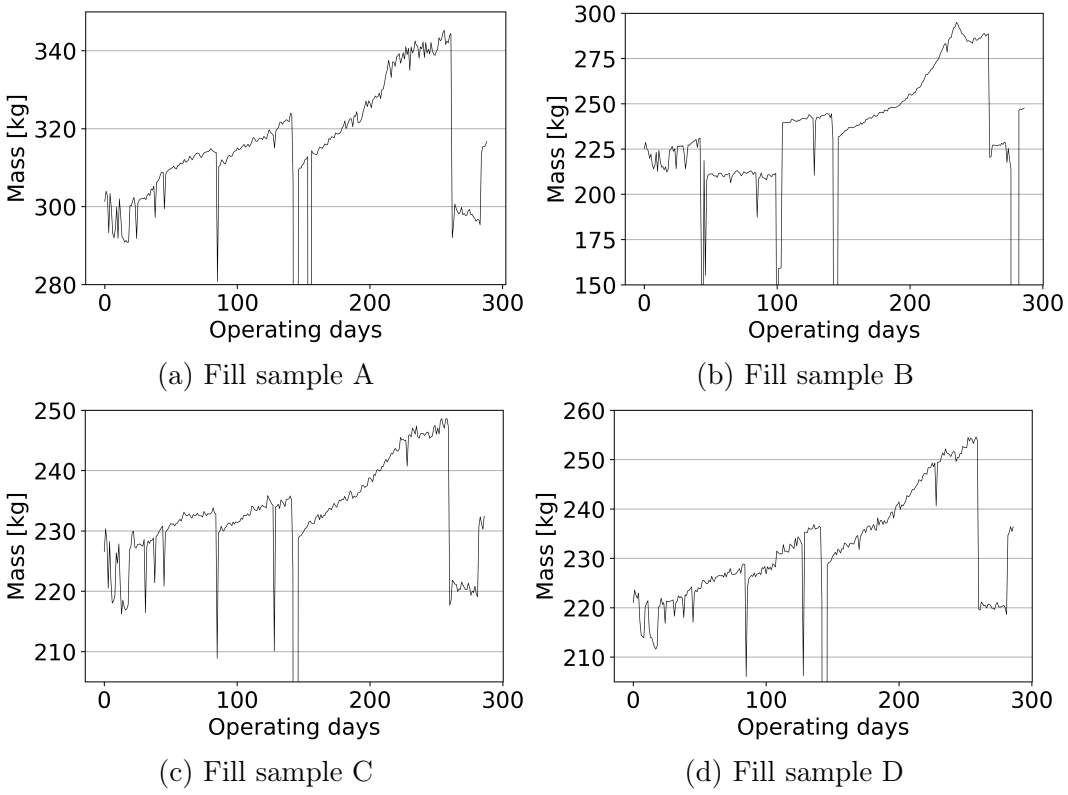

(a) Fill sample A

(b) Fill sample B

(c) Fill sample C

(d) Fill sample D

Figure 7.7: Measured drip-dry fill sample mass

The maximum mass gain for each fill during the test periods are presented in Table 7.1. These correspond with the visual observations in Section 7.2: with Fill C having the lowest amount of observed fouling and mass gain and Fill B similarly having the highest amount of observed fouling and mass gain. It is

Table 7.1: Summary of fill mass measurements

Fill	**Start mass [kg]**	**Maximum mass [kg]**	**Mass gain [kg]**
A	301.3	345.7	44.4
B	225.2	295.0	69.8
C	226.6	248.6	22.0
D	221.1	254.6	33.5

concluded that the fill mass measurements were performed successfully, given the generally smooth behaviour of the measured values and the corresponding behaviour of the mass measurements and visual inspections. Unfortunately, due to the more erratic behaviour of the fill performance measurements, it is not possible to draw conclusions on the relationship between fill mass gain and performance change from these results.

Chapter 8: Conclusion

8.1 Conclusions

This study aims to quantify the effects of NDWCT fill fouling using fair methods to enable the commercial comparison between competing fill designs. The objectives of this study, discussed below, were developed in the context of a wider study by the South African state-owned power utility, Eskom, to make better-informed fill selections for future fill replacement projects for its large fleet of operational NDWCTs. The current study uses the Eskom fill fouling test facility located at a coal-fired power station to partially demonstrate the use of the methods developed.

The first objective of this study was to determine how to quantify the fouling performance of NDWCT fills for commercial comparison. The literature study (Chapter 3) yielded various methods of quantifying fill fouling, but no methods to fairly compare the performance for the use in commercial decision-making. To this end, the interaction of the thermal and hydraulic effects of NDWCT fill fouling was investigated numerically (Chapter 6). It was determined using Monte Carlo methods that these effects can be seen as almost completely separate, when considering their effects on NDWCT performance. This led to the proposal of a novel method of fill fouling quantification: the use of individual time-dependent thermal and hydraulic fouling factors. It is demonstrated how measured and predicted fouling factors can be used in fill life-cycle calculations to obtain financial results that can be used to compare fills (Appendix F).

The second objective was to critically analyse the Eskom fill fouling test facility design and results. This was achieved by performing an uncertainty analysis on the test facility equipment and results. These uncertainties were propagated in a novel way to NDWCT performance prediction calculations by modifying existing one-dimensional regression uncertainty equations to apply to the two-variable regressions of fill thermal and hydraulic performance characteristic equations. It was also determined that it is vital to take correlated uncertainties into account when calculating the regression uncertainties. The calculated regression uncertainties were propagated to the NDWCT performance, where it was determined that correlated uncertainties may be neglected with only small errors (Chapter 5). The uncertainty analysis was also performed for the fouling factors, including the uncertainty of NDWCT performance prediction using fill fouling factors (Chapter 6). The developed methods of fill performance testing uncertainty analysis takes account of the uncertainties at all levels of the performance testing process, providing rigorous justification for performance-related commercial decisions, such as fill selection from a set of competing designs, based on fill performance testing. The data analysis pro-

cess highlighted some design and operating deficiencies and recommendations are discussed in Section 8.2.

The third objective was to apply the developed methods to the fouling testing of at least four NDWCT fill designs and to draw conclusions. This was achieved by plotting the fouling factors and predicted NDWCT water outlet temperatures for the four fills tested at the fill fouling test facility (Chapter 7). Unfortunately the test data over the testing period did not show smooth changes in the fill thermal performance, with some of the data behaving quite erratically. While no specific long-term performance-based conclusions could be drawn from the data obtained during the test period, the methods developed may be employed once these testing problems have been resolved.

8.2 Testing recommendations

The following improvements are suggested for the current test facility or for future test facilities designed for long-term testing of NDWCT fill samples:

(i) Measurement of droplet size in the rain zone, possibly in line with the method of Terblanche (2011) is suggested. This will not only increase the accuracy of the correction applied to the measured fill performance (see Section 4.4.2), but also provide the correct droplet size to be used in the cooling tower performance calculation for each fill.

(ii) A new design for the measurement of bypass and wall water is required which can accurately measure an instantaneous value over a wide range of water flow rates.

(iii) The contractor has proposed that the current fully automatic performance testing regime be amended by employing some manual intervention: an operator would determine a good time for testing to take place based on actual weather conditions. Inspection or servicing of some critical equipment is then to be performed before each test.

(iv) At typical predicted NDWCT T_{wo} standard uncertainties of 0.5 °C, the uncertainties of the measurements are relatively high, especially considering it is approximately half the typically reported 95% uncertainty. Reduction of measurement uncertainties will increase the confidence of NDWCT performance predictions as well as the comparison of competing fills. A general effort should be engaged in to reduce uncertainties at the current facility. Specific suggestions follow:

   (a) On-site calibration of equipment, including the data capture system, may remove much of the systematic uncertainty related to these equipment and also simplify the calculation of the equipment systematic uncertainties somewhat. This is especially valuable for the measurement of the pressure difference over the fill, since the

calculation of the hydraulic performance of the fill is very sensitive to this small pressure difference.

(b) Where the water flow rate is known for the NDWCT where a fill is planned to be installed, such as for fill replacement projects, performance testing at the cooling tower G_w is recommended. This better approximates the operating conditions for fouling formation and will greatly simplify the uncertainty analysis by removing the water flow input from the regressions. The removal of G_w uncertainties and a better fit of the regression to the data (being a function of one rather than two inputs) should yield reduced overall uncertainty.

(c) The sampling rate should be increased to at least 30 measurements taken at each test operating point. This will allow simple calculation of uncertainties at the commonly-used 95% confidence level.

(d) Turn-down ratios should be optimised to reduce the total uncertainty by taking the uncertainties of the sensor, supporting equipment and PLC into account.

8.3 Future work

The following possible areas of future work are foreseen:

(i) A limitation on the Eskom fill fouling test facility, and fill fouling testing in general, is the extended testing periods required, especially for low-fouling fill designs. Methods may be explored to initiate or enhance the formation of fouling to reduce the required testing time.

(ii) The location of the test facility at an operational power station and the fact that it contains multiple identical and well-equipped test sections, allow the comparative testing of the performance of technologies other than fill designs. This may include technologies such as fouling control methods.

(iii) The uncertainty analysis performed in this study is quite complex, given the various stages at which uncertainty analysis must be performed, including correlated uncertainties. The Monte Carlo method of uncertainty analysis, as presented in Coleman and Steele (2018), may provide a simpler method of uncertainty analysis, although it is expected that it will be computationally expensive to perform, possibly requiring several thousand NDWCT performance prediction calculations for the uncertainty value at a single operating point to converge.

Appendix A: Properties of fluids

All fluid properties are obtained from Kröger (2004).

Density of dry air:

$$\rho_a = p_a/(287.08\ T),\ \text{kg/m}^3 \tag{A.1}$$

Specific heat capacity of dry air at constant pressure:

$$\begin{aligned} c_{pa} &= 1.045356 \times 10^3 - 3.161783 \times 10^{-1}\ T + 7.083814 \times 10^{-4}\ T^2 \\ &\quad - 2.705209 \times 10^{-7}\ T^3,\ \text{J/kgK} \end{aligned} \tag{A.2}$$

Specific heat capacity of water vapour at constant pressure:

$$\begin{aligned} c_{pv} &= 1.3605 \times 10^3 + 2.31334\ T - 2.46784 \times 10^{-10}\ T^5 \\ &\quad + 5.91332 \times 10^{-13}\ T^6,\ \text{J/kgK} \end{aligned} \tag{A.3}$$

Dynamic viscosity of dry air:

$$\begin{aligned} \mu_a &= 2.287973 \times 10^{-6} + 6.259793 \times 10^{-8}\ T \\ &\quad - 3.131956 \times 10^{-11}\ T^2 + 8.15038 \times 10^{-15}\ T^3,\ \text{kg/ms} \end{aligned} \tag{A.4}$$

Specific heat capacity of liquid water:

$$\begin{aligned} c_{pw} &= 8155.99 - 28.0627\ T + 0.0511283\ T^2 \\ &\quad - 2.17582 \times 10^{-13}\ T^6,\ \text{J/kgK} \end{aligned} \tag{A.5}$$

Density of saturated liquid water:

$$\begin{aligned} \rho_w &= (1.49343 \times 10^{-3} - 3.7164 \times 10^{-6}\ T + 7.09782 \times 10^{-9}\ T^2 \\ &\quad - 1.90321 \times 10^{-20}\ T^6)^{-1},\ \text{kg/m}^3 \end{aligned} \tag{A.6}$$

Surface tension of saturated liquid water:

$$\begin{aligned} \sigma_w &= 5.148103 \times 10^{-2} + 3.998714 \times 10^{-4}\ T \\ &\quad - 1.4721869 \times 10^{-6}\ T^2 + 1.21405335 \times 10^{-9}\ T^3,\ \text{N/m} \end{aligned} \tag{A.7}$$

Latent heat of vaporization:

$$\begin{aligned} i_{fgw} &= 3.4831814 \times 10^6 - 5.8627703 \times 10^3\ T + 12.139568\ T^2 \\ &\quad - 1.40290431 \times 10^{-2}\ T^3,\ \text{J/kg} \end{aligned} \tag{A.8}$$

Dynamic viscosity of saturated water vapour:

$$\begin{aligned} \mu_v &= 2.562435 \times 10^{-6} + 1.816683 \times 10^{-8}\ T \\ &\quad + 2.579066 \times 10^{-11}\ T^2 - 1.067299 \times 10^{-14}\ T^3,\ \text{kg/ms} \end{aligned} \tag{A.9}$$

Density of air-vapour mixture:

$$\rho_{av} = (1+w)\left[1 - \frac{w}{w + 0.62198}\right]\ p_{abs}/(287.08\ T),\ \ \text{kg/m}^3 \tag{A.10}$$

Vapour fraction of air-vapour mixture:

$$\begin{aligned} w = & \left(\frac{2501.6 - 2.3263\ (T_{wb} - 273.15)}{2501.6 + 1.8577\ (T - 273.15) - 4.184\ (T_{wb} - 273.15)} \right) \\ & \times \left(\frac{0.62509\ p_{vwb}}{p_{abs} - 1.005\ p_{vwb}} \right) \\ & - \left(\frac{1.00416\ (T - T_{wb})}{2501.6 + 1.8577\ (T - 273.15) - 4.184\ (T_{wb} - 273.15)} \right), \\ & \text{kg/kg dry air} \end{aligned} \tag{A.11}$$

Vapour pressure in air-vapour mixture:

$$p_v = 10^z,\ \text{Pa} \tag{A.12}$$

with:

$$\begin{aligned} z = & 10.79586\ (1 - 273.16/T) + 5.02808\ \log_{10}(273.16/T) \\ & + 1.50474 \times 10^{-4}\ [1 - 10^{-8.29692\ ((T/273.16)-1)}] \\ & + 4.2873 \times 10^{-4}\ [10^{4.76955\ (1-273.16/T)} - 1] \\ & + 2.786118312 \end{aligned} \tag{A.13}$$

Enthalpy of air-vapour mixture:

$$i_{ma} = c_{pa}(T - 273.15) + w[i_{fgw0} + c_{pv}(T - 273.15)],\ \text{J/kg dry air} \tag{A.14}$$

with the latent heat of vaporization at 0 °C calculated using Equation A.8:

$$\begin{aligned} i_{fgw0} &= 3.4831814 \times 10^6 - 5.8627703 \times 10^3 \times 273.15 \\ &\quad + 12.139568 \times 273.15^2 - 1.40290431 \times 10^{-2} \times 273.15^3 \\ &= 2501598.53\ \text{J/kg} \end{aligned} \tag{A.15}$$

where c_{pa} and c_{pv} are analysed at $(T + 273.15\ \text{K})/2$.

Dynamic viscosity of air-vapour mixture:

$$\mu_{av} = (X_a \mu_a M_a^{0.5} + X_v \mu_v M_v^{0.5})/(X_a M_a^{0.5} + X_v M_v^{0.5}),\ \text{kg/ms} \tag{A.16}$$

with:

$$M_a = 28.97\ \text{kg/mol} \tag{A.17}$$

$$M_v = 18.016\ \text{kg/mol} \tag{A.18}$$

$$X_a = 1/(1 + 1.608\ w) \tag{A.19}$$

$$X_v = w/(w + 0.622) \tag{A.20}$$

Appendix B: Numerical methods

B.1 Chebychev integral for Merkel number

The Merkel number (Equation 2.31) is numerically approximated, as in Kröger (2004), using the Chebychev integral:

$$\int_{T_{wo}}^{T_{wi}} \frac{c_{pw} dT_w}{(i_{masw} - i_{ma})} \approx \frac{c_{pwm}(T_{wi} - T_{wo})}{4} \times \left(\frac{1}{\Delta i_{(1)}} + \frac{1}{\Delta i_{(2)}} + \frac{1}{\Delta i_{(3)}} + \frac{1}{\Delta i_{(4)}} \right) \tag{B.1}$$

The subscripts (1) through (4) denote properties calculated at intermediate temperatures $T_{w(1)}$ through $T_{w(4)}$ with:

$$T_{w(1)} = T_{wo} + 0.1\ (T_{wi} - T_{wo}) \tag{B.2}$$

$$T_{w(2)} = T_{wo} + 0.4\ (T_{wi} - T_{wo}) \tag{B.3}$$

$$T_{w(3)} = T_{wo} + 0.6\ (T_{wi} - T_{wo}) \tag{B.4}$$

$$T_{w(4)} = T_{wo} + 0.9\ (T_{wi} - T_{wo}) \tag{B.5}$$

and

$$\Delta i_{(n)} = i_{masw(n)} - i_{ma(n)} \tag{B.6}$$

for each n from 1 to 4. Each $i_{masw(n)}$ is calculated using Equation A.14 with both the wet-bulb and dry-bulb temperatures being the intermediate temperature ($T_{w(n)}$). Each $i_{ma(n)}$ for intermediate temperature $T_{w(n)}$ is calculated using the following equation:

$$i_{ma(n)} = m_w c_{pwm}(T_{w(n)} - T_{wo})/m_a + i_{ma1} \tag{B.7}$$

where i_{ma1} is the inlet air enthalpy.

B.2 Forward difference method

Partial differentials are calculated using the forward difference method, which is presented by Burden and Faires (2011) as:

$$f'(x) \approx \frac{f(x_0 + h) - f(x_0)}{h} \text{ with } h > 0 \tag{B.8}$$

Appendix C: Sample fill performance test results calculation

This sample calculation demonstrates how to obtain fill performance results (G_w, G_a, Me_{fi} and K_{fd}) at a single test operating point. The results of all 25 test operating points in the performance test are then used in a non-linear regression to obtain the fill performance characteristic equations.

C.1 Calculation inputs

The inputs to the calculation are the test data presented in Table C.1, obtained during a fill performance test, and additional information in the list below.

Table C.1: Example calculation input data

Time	$\mathbf{V_{wi}}$	$\mathbf{\Delta p_{pnz}}$	$\mathbf{\Delta p_{nzl}}$	$\mathbf{\Delta p_{fi}}$	$\mathbf{T_{wi}}$	$\mathbf{T_{wo}}$	$\mathbf{T_{db}}$	$\mathbf{T_{wb}}$	$\mathbf{V_{byp}}$	$\mathbf{V_{wall}}$	$\mathbf{p_a}$
[hh:mm]	**[m^3/hr]**	**[Pa]**	**[Pa]**	**[Pa]**	**[°C]**	**[°C]**	**[°C]**	**[°C]**	**[L/s]**	**[L/s]**	**[kPa]**
22:13	21.58	105.43	412.83	54.93	49.77	21.65	18.01	9.87	0.00987	0.064	84.120
22:14	21.58	108.44	425.00	57.57	49.77	20.74	17.99	9.86	0.00987	0.064	84.120
22:15	21.59	109.44	429.54	56.77	49.85	20.38	17.96	9.83	0.00987	0.068	84.117
22:16	21.55	109.98	430.90	57.31	49.77	20.25	17.95	9.81	0.00987	0.068	84.117
22:17	21.50	110.07	430.77	57.44	49.69	20.16	17.93	9.80	0.02896	0.070	84.115
22:18	21.58	110.07	431.45	57.81	49.64	20.10	17.91	9.78	0.02896	0.070	84.120
22:19	21.56	110.20	431.55	56.92	49.48	20.08	17.89	9.77	0.02896	0.071	84.120
22:20	21.55	110.50	431.23	57.01	49.54	20.07	17.94	9.75	0.02896	0.071	84.117

Additional information:

(i) The wind was from a westerly direction and was steady at approximately 2.3 m/s.

(ii) The fill height (L_{fi}) is 2 m. The height of the spray zone (L_{sp}) is 0.474 m and of the rain zone (H_{rz}) is 1.02 m.

Rounding of values in Table C.1 and these calculations are for formatting or readability reasons. Calculations are done to 15 decimal place accuracy. Errors due to rounding in these calculations are considered negligible given the general reporting of 3 to 5 significant figures.

C.2 Measurement means

The mean ($\overline{X}$) of each measurement, calculated using Equation 5.1, is presented in Table C.2.

Table C.2: Measurement means

$\overline{\mathbf{V}}_{\mathbf{wi}}$	$\overline{\mathbf{\Delta p}}_{\mathbf{pnz}}$	$\overline{\mathbf{\Delta p}}_{\mathbf{nzl}}$	$\overline{\mathbf{\Delta p}}_{\mathbf{fi}}$	$\overline{\mathbf{T}}_{\mathbf{wi}}$	$\overline{\mathbf{T}}_{\mathbf{wo}}$	$\overline{\mathbf{T}}_{\mathbf{db}}$	$\overline{\mathbf{T}}_{\mathbf{wb}}$	$\overline{\mathbf{V}}_{\mathbf{byp}}$	$\overline{\mathbf{V}}_{\mathbf{wall}}$	$\overline{\mathbf{p}}_{\mathbf{a}}$
[m³/hr]	**[Pa]**	**[Pa]**	**[Pa]**	**[°C]**	**[°C]**	**[°C]**	**[°C]**	**[L/s]**	**[L/s]**	**[kPa]**
21.56	109.27	427.91	56.97	49.69	20.43	17.95	9.81	0.01941	0.068	84.119

C.3 Test operating point results

C.3.1 Fill water mass flux

The water mass flux through the fill is calculated by subtracting the bypass and wall water mass flow rates from the inlet water mass flow rate. These flows are provided in m³/hr or L/s units and are converted to mass flow rates using the water inlet density at the water inlet temperature $\overline{T}_{wi} = 322.84$ K using Equation A.6:

$$\begin{aligned}\rho_{wi} &= (1.49343 \times 10^{-3} - 3.7164 \times 10^{-6} \times 322.84 \\ &\quad + 7.09782 \times 10^{-9} \times 322.84^2 - 1.90321 \times 10^{-20} \times 322.84^6)^{-1} \\ &= 988.28 \text{ kg/m}^3\end{aligned}$$

The water inlet mass flow rate in kg/s is calculated from the volume flow $\overline{V}_{wi}$ by:

$$\begin{aligned}m_{wi} &= \overline{V}_{wi}\rho_{wi} \times \frac{1 \text{ hr}}{3600 \text{ s}} = 21.56 \text{ m}^3\text{/hr } 988.28 \text{ kg/m}^3 \times \frac{1 \text{ hr}}{3600 \text{ s}} \\ &= 5.919 \text{ kg/s}\end{aligned} \tag{C.1}$$

The bypass and wall mass flow rates are calculated with:

$$m_{byp} = \frac{\overline{V}_{byp}\rho_{wi}}{1000 \text{ L/m}^3} = \frac{0.0194 \text{ L/s } 988.28 \text{ kg/m}^3}{1000 \text{ L/m}^3} = 0.0192 \text{ kg/s} \tag{C.2}$$

and

$$m_{wall} = \frac{\overline{V}_{wall}\rho_{wi}}{1000 \text{ L/m}^3} = \frac{0.0681 \text{ L/s } 988.28 \text{ kg/m}^3}{1000 \text{ L/m}^3} = 0.0673 \text{ kg/s} \tag{C.3}$$

Subtracting the bypass and wall water mass flow rates from the inlet water mass flow rate, as in Equation 4.12:

$$m_w = 5.919 - 0.0192 - 0.0673 = 5.833 \text{ kg/s}$$

Dividing by the fill frontal area to obtain the fill water mass flux, as in Equation 4.13, yields:

$$G_w = 5.833/2.25 = 2.592 \text{ kg/m}^2\text{s}$$

C.3.2 Dry air mass flux

The air pressure before the air-flow measurement nozzle is calculated using Equation 4.15:

$$p_{pnz} = 84.119 \text{ kPa} - 109.26 \text{ Pa} = 84009 \text{ Pa}$$

The air at the fill outlet is assumed to be saturated and is calculated iteratively to be $T_{ao} = 34.45\ ^{\circ}\text{C} = 307.60\ \text{K}$.

From Equation A.13 find:

$$\begin{aligned} z &= 10.79586\ (1 - 273.16/307.60) + 5.02808\ \log_{10}(273.16/307.60) \\ &\quad + 1.50474 \times 10^{-4}\ \left[1 - 10^{-8.29692\ (307.60/273.16)-1}\right] \\ &\quad + 4.2873 \times 10^{-4}\ [104.76955\ (1 - 273.16/307.60) - 1] \\ &\quad + 2.786118312 \\ &= 3.737 \end{aligned}$$

The vapour pressure at T_{ao} is now calculated using Equation A.12:

$$p_v = 10^{3.737} = 5455.70\ \text{Pa}$$

The vapour fraction at the fill outlet is calculated using Equation A.11:

$$\begin{aligned} w_{avo} &= \left(\frac{2501.6 - 2.3263\ (307.60 - 273.15)}{2501.6 + 1.8577\ (307.60 - 273.15) - 4.184\ (307.60 - 273.15)}\right) \\ &\quad \times \left(\frac{0.62509 \times 5455.70}{84009 - 1.005 \times 5455.70}\right) \\ &\quad - \left(\frac{1.00416\ (307.60 - 307.60)}{2501.6 + 1.8577\ (307.60 - 273.15) - 4.184\ (307.60 - 273.15)}\right) \\ &= 0.0434\ \text{kg/kg dry air} \end{aligned}$$

The fill outlet air-vapour density is calculated using Equation A.10:

$$\begin{aligned} \rho_{avo} &= (1 + 0.0434)\left[1 - \frac{0.0434}{0.0434 + 0.62198}\right] 84009/(287.08 \times 307.60) \\ &= 0.9278\ \text{kg/m}^3 \end{aligned}$$

The mass flow of the outlet air-vapour mixture is calculated with Equation 4.14:

$$m_{avo} = \frac{0.98 \times \pi \times 0.550^2\sqrt{2 \times 0.9278 \times 427.91}}{4} = 6.561\ \text{kg/s}$$

The dry air mass flow is calculated using Equation 4.17:

$$m_a = 6.561/(1 + 0.0434) = 6.288\ \text{kg/s}$$

The dry air mass flux is calculated using Equation 4.18:

$$G_a = 6.288/2.25 = 2.795\ \text{kg/m}^2\text{s}$$

The remaining equations in this section are performed to confirm the iterative solution for T_{ao}.

The mean water temperature is calculated:

$$T_{wm} = \frac{\overline{T}_{wi} + \overline{T}_{wo}}{2} = \frac{49.69 + 20.43}{2} = 35.06\ ^{\circ}\text{C} = 308.21\ \text{K}$$

The specific heat capacity of liquid water at the mean water temperature is

calculated using Equation A.5:

$$\begin{aligned} c_{pw} &= 8155.99 - 28.0627 \times 308.21 + 0.0511283 \times 308.21^2 \\ &\quad - 2.17582 \times 10^{-13} \times 308.21^6 \\ &= 4177.13 \text{ J/kgK} \end{aligned}$$

The air inlet properties are calculated with $\overline{T}_{db} = 291.10$ K, $\overline{T}_{wb} = 282.96$ K and $\overline{p}_a = 84119$ Pa. Using Equation A.13 at $\overline{T}_{wb}$:

$$\begin{aligned} z &= 10.79586\ (1 - 273.16/282.96) + 5.02808\ \log_{10}(273.16/282.96) \\ &\quad + 1.50474 \times 10^{-4}\ [1 - 10^{-8.29692\ (282.96/273.16)-1}] \\ &\quad + 4.2873 \times 10^{-4}\ [104.76955\ (1 - 273.16/282.96) - 1] + 2.786118312 \\ &= 3.083 \end{aligned}$$

The vapour pressure is calculated using Equation A.12:

$$p_v = 10^{3.083} = 1211.17 \text{ Pa}$$

The air inlet vapour fraction is calculated using Equation A.11:

$$\begin{aligned} w_{ai} &= \left(\frac{2501.6 - 2.3263\ (282.96 - 273.15)}{2501.6 + 1.8577\ (291.10 - 273.15) - 4.184\ (282.96 - 273.15)} \right) \\ &\quad \times \left(\frac{0.62509 \times 1211.17}{84538 - 1.005 \times 1211.17} \right) \\ &\quad - \left(\frac{1.00416\ (291.10 - 282.96)}{2501.6 + 1.8577\ (291.10 - 273.15) - 4.184\ (282.96 - 273.15)} \right) \\ &= 0.00580 \text{ kg/kg dry air} \end{aligned}$$

The dry air specific heat capacity of the inlet air is calculated using Equation A.2 at $(\overline{T}_{db} + 273.15)/2 = 282.12$ K:

$$\begin{aligned} c_{pai} &= 1.045356 \times 10^3 - 3.161783 \times 10^{-1} \times 282.12 + 7.083814 \times 10^{-4} \\ &\quad \times 282.12^2 - 2.705209 \times 10^{-7} \times 282.12^3 \\ &= 1006.46 \text{ J/kgK} \end{aligned}$$

The specific heat capacity of water vapour is calculated using Equation A.3, also at 282.12 K:

$$\begin{aligned} c_{pvi} &= 1.3605 \times 10^3 + 2.31334 \times 282.12 - 2.46784 \times 10^{-10} \times 282.12^5 \\ &\quad + 5.91332 \times 10^{-13} \times 282.12^6 \\ &= 1870.24 \text{ J/kgK} \end{aligned}$$

The enthalpy of the inlet air is calculated using Equation A.14:

$$\begin{aligned} i_{mai} &= 1006.46\ (291.10 - 273.15) + 0.00580 \times [2501598.53 \\ &\quad + 1870.24 \times (291.10 - 273.15)] \\ &= 32764.58 \text{ J/kg dry air} \end{aligned}$$

The remaining outlet air properties are calculated, with the air assumed to be saturated with vapour at $T_{db} = T_{wb} = T_{ao} = 307.60$ K and $p_{pnz} = 84009$ Pa.

The dry air specific heat capacity is calculated using Equation A.2 at $(307.60\ \text{K} + 273.15)/2 = 290.38\ \text{K}$:

$$\begin{aligned} c_{pao} &= 1.045356 \times 10^{3} - 3.161783 \times 10^{-1} \times 290.38 \\ &\quad + 7.083814 \times 10^{-4} \times 290.38^{2} - 2.705209 \times 10^{-7} \times 290.38^{3} \\ &= 1006.65\ \text{J/kgK} \end{aligned}$$

The specific heat capacity of water vapour is calculated using Equation A.3, also at 290.39 K:

$$\begin{aligned} c_{pvo} &= 1.3605 \times 10^{3} + 2.31334 \times 290.38 - 2.46784 \times 10^{-10} \times 290.38^{5} \\ &\quad + 5.91332 \times 10^{-13} \times 290.38^{6} \\ &= 1877.24\ \text{J/kgK} \end{aligned}$$

The outlet air enthalpy is calculated using Equation A.14:

$$\begin{aligned} i_{mao} &= 1006.65\ (307.60 - 273.15) + 0.0434 \\ &\quad \times [2501598.53 + 1877.24\ (307.60 - 273.15)] \\ &= 146136.14\ \text{J/kg dry air} \end{aligned}$$

The energy balance is performed across the water and air-flows using Equation 4.16:

$$5.83 \times 4177.13\ (49.69 - 20.43) = 6.288\ (146136.14 - 32764.58)$$
$$712875\ \text{J/s} = 712875\ \text{J/s}$$

This confirms that the iteratively calculated value of T_{ao} is correct.

C.3.3 Merkel number

The Merkel number is calculated using the Chebychev integral in Appendix B.1. The intermediate temperatures are calculated using Equations B.2 through B.5:

$$\begin{aligned} T_{w(1)} &= 293.58 + 0.1\ (322.84 - 293.58) = 296.51\ \text{K} \\ T_{w(2)} &= 293.58 + 0.4\ (322.84 - 293.58) = 305.28\ \text{K} \\ T_{w(3)} &= 293.58 + 0.6\ (322.84 - 293.58) = 311.14\ \text{K} \\ T_{w(4)} &= 293.58 + 0.9\ (322.84 - 293.58) = 319.91\ \text{K} \end{aligned}$$

The values of $i_{masw(1)}$ through $i_{masw(4)}$ are calculated using Equation A.14 at $T_{w(1)}$ through $T_{w(4)}$, with the values for both T_{db} and T_{wb} being the respective intermediate temperatures and the pressure at which the calculations are performed at the estimated pressure $\overline{p}_a - 0.5\ \overline{\Delta p}_{fi} = 84090.08$ Pa at the centre of the fill:

$$\begin{aligned} i_{masw(1)} &= 1006.52\ (296.51 - 273.15) \\ &\quad + 0.0221\ [2501598.53 + 1872.51\ (296.51 - 273.15)] \\ &= 79723.00\ \text{J/kg} \\ i_{masw(2)} &= 1006.62\ (305.28 - 273.15) \\ &\quad + 0.0378\ [2501598.53 + 1876.24\ (305.28 - 273.15)] \\ &= 129118.51\ \text{J/kg} \\ i_{masw(3)} &= 1006.70\ (311.14 - 273.15) \\ &\quad + 0.0534\ [2501598.53 + 1878.78\ (311.14 - 273.15)] \\ &= 175747.43\ \text{J/kg} \\ i_{masw(4)} &= 1006.83\ (319.91 - 273.15) \\ &\quad + 0.0891\ [2501598.53 + 1882.69\ (319.91 - 273.15)] \\ &= 277925.16\ \text{J/kg} \end{aligned}$$

The values of $i_{ma(1)}$ through $i_{ma(4)}$ are calculated using Equation B.7:

$$\begin{aligned} i_{ma(1)} &= 5.832 \times 4177.13\ (296.51 - 293.58)/6.288 + 32764.58 \\ &= 44101.73\ \text{J/kg} \\ i_{ma(2)} &= 5.832 \times 4177.13\ (305.28 - 293.58)/6.288 + 32764.58 \\ &= 78113.20\ \text{J/kg} \\ i_{ma(3)} &= 5.832 \times 4177.13\ (311.14 - 293.58)/6.288 + 32764.58 \\ &= 100787.51\ \text{J/kg} \\ i_{ma(4)} &= 5.832 \times 4177.13\ (319.91 - 293.58)/6.288 + 32764.58 \\ &= 134798.98\ \text{J/kg} \end{aligned}$$

The values of $\Delta i_{(1)}$ through $\Delta i_{(4)}$ are calculated using Equation B.6:

$$\begin{aligned} \Delta i_{(1)} &= 79723.00 - 44101.73 = 35621.27\ \text{J/kg} \\ \Delta i_{(2)} &= 129118.51 - 78113.20 = 51005.31\ \text{J/kg} \\ \Delta i_{(3)} &= 175747.43 - 100787.51 = 74959.92\ \text{J/kg} \\ \Delta i_{(4)} &= 277925.16 - 134798.98 = 143126.18\ \text{J/kg} \end{aligned}$$

The measured Merkel number is calculated using Equation B.1:

$$\begin{aligned} Me_{meas} &= \frac{4177.13\ (322.84 - 293.58)}{4} \\ &\quad \times \left(\frac{1}{35621.27} + \frac{1}{51005.31} + \frac{1}{74959.92} + \frac{1}{143126.18} \right) = 2.078 \end{aligned}$$

The corrected Merkel number (Me_{corr}) is calculated by subtracting the rain and spray zone Merkel numbers from the measured Merkel number. The

Merkel number for the spray zone is calculated using Equation 2.89:

$$Me_{sp} = 0.2 \times 0.474 \left(\frac{2.795}{2.592}\right)^{0.5} = 0.0984$$

Additional properties are calculated for the rain zone Merkel number calculation. The density of water at $\overline{T}_{wo} = 293.58\ K$ is calculated using Equation A.6:

$$\begin{aligned}\rho_w &= (1.49343 \times 10^{-3} - 3.7164 \times 10^{-6} \times 293.58 \\ &\quad + 7.09782 \times 10^{-9} \times 293.58^2 - 1.90321 \times 10^{-20} \times 293.58^6)^{-1} \\ &= 998.06\ \text{kg/m}^3\end{aligned}$$

The vapour fraction of air saturated at the dry-bulb temperature is calculated using Equation A.11, with both input temperatures taken as $\overline{T}_{db}$ at $\overline{p}_a$:

$$w_s = 0.0157\ \text{kg/kg dry air}$$

The dynamic viscosity of saturated water vapour is calculated using Equation A.9 at the dry-bulb temperature $\overline{T}_{db} = 291.10$ K:

$$\begin{aligned}\mu_v &= 2.562435 \times 10^{-6} + 1.816683 \times 10^{-8} \times 291.10 \\ &\quad + 2.579066 \times 10^{-11} \times 291.10^2 - 1.067299 \times 10^{-14} \times 291.10^3 \\ &= 9.773 \times 10^{-6}\ \text{kg/ms}\end{aligned}$$

The dynamic viscosity of dry air is calculated using Equation A.4 at the dry-bulb temperature $\overline{T}_{db} = 291.10$ K:

$$\begin{aligned}\mu_a &= 2.287973 \times 10^{-6} + 6.259793 \times 10^{-8} \times 291.10 \\ &\quad - 3.131956 \times 10^{-11} \times 291.10^2 + 8.15038 \times 10^{-15} \times 291.10^3 \\ &= 1.806 \times 10^{-5}\ \text{kg/ms}\end{aligned}$$

Coefficients for Equation A.16 are calculated using Equations A.19 and A.20 respectively:

$$\begin{aligned}X_a &= 1/(1 + 1.608 \times 0.00580) = 0.991 \\ X_v &= 0.00580/(0.00580 + 0.622) = 0.00923\end{aligned}$$

The dynamic viscosity of air-vapour mixture is calculated using Equation A.16:

$$\begin{aligned}\mu_{av} &= (0.991 \times 1.806 \times 10^{-5} \times 28.97^{0.5} + 0.00923 \times 9.773 \times 10^{-6} \\ &\quad \times 18.016^{0.5})/(0.991 \times 28.97^{0.5} + 0.00923 \times 18.016^{0.5}) \\ &= 1.800 \times 10^{-5}\ \text{kg/ms}\end{aligned}$$

The surface tension of water at the outlet water temperature is calculated using Equation A.7:

$$\begin{aligned}\sigma_{wo} &= 5.148103 \times 10^{-2} + 3.998714 \times 10^{-4} \times 293.58 \\ &\quad - 1.4721869 \times 10^{-6} \times 293.58^2 + 1.21405335 \times 10^{-9} \times 293.58^3 \\ &= 0.0727\ \text{N/m}\end{aligned}$$

Coefficients are calculated using Equation 2.48 through 2.51:

$$a_\mu = 3.061 \times 10^{-6} \left[998.06^4 \times 9.81^9 / 0.0727\right]^{0.25} = 1.0020$$
$$a_\rho = 998.0/998.06 = 0.9999$$
$$a_v = 73.298 \left[9.81^5 \times 0.0727^3 / 998.06^3\right]^{0.25} = 1.0035$$
$$a_L = 6.122 \left[9.81 \times 0.0727/998.06\right]^{0.25} = 1.00096$$

The dry air density is calculated using Equation A.1:

$$\rho_a = 84119/(287.08 \times 291.10) \quad = 1.0066 \text{ kg/m}^3$$

The diffusion coefficient is calculated using Equation 2.86:

$$D = \left[0.04357 \times 291.10^{1.5} \left(\frac{1}{28.97} + \frac{1}{18.016}\right)^{0.5}\right] / \left[84119 \ \left(29.9^{0.333} + 18.8^{0.333}\right)^2\right] = 2.329 \times 10^{-5} \text{ m}^2/\text{s}$$

The Schmidt number is calculated using Equation 2.85:

$$Sc = 1.814 \times 10^{-5}/(1.0031 \times 2.329 \times 10^{-5}) = 0.770$$

The dry air velocity at the top of the rain zone is calculated using Equation 2.47:

$$v_{azo} = 6.288/(1.0066 \times 2.25) = 2.776 \text{ m/s}$$

The Merkel number of the rain zone is calculated using Equation 4.24:

$$\begin{aligned} Me_{rz} = 3.6 &\times \left(\frac{84119}{461.52 \times 291.10 \times 998.06}\right) \times \left(\frac{2.329 \times 10^{-5}}{2.776 \times 0.005}\right) \\ &\times \left(\frac{1.02002}{0.005}\right) \times 0.770^{0.33} \\ &\times \left[\ln\left(\frac{0.0157 + 0.622}{0.00580 + 0.622}\right) / (0.0157 - 0.00580)\right] \\ &\times [5.01134 \times 0.9999 \times 1.0066 - 192121.7 \times 1.0020 \times 1.806 \times 10^{-5} \\ &- 2.57724 + 23.61842 \left(0.2539 \left(1.0035 \times 2.776\right)^{1.67} + 0.18\right) \\ &\times \left(0.83666 \left(1.00096 \times 1.02002\right)^{-0.5299} + 0.42\right) \\ &\times \left(43.0696 \left(1.00096 \times 0.005\right)^{0.7947} + 0.52\right)] \\ &= 0.0596 \end{aligned}$$

The corrected Merkel number is calculated using Equation 4.22:

$$Me_{fi} = 2.078 - 0.0984 - 0.0596 = 1.920$$

C.3.4 Pressure loss factor

The pressure loss factor is calculated according to Section 4.3.5. The inlet air mass flow is calculated using:

$$m_{avi} = m_a(1 + w_{ai}) = 6.288\ (1 + 0.00580) = 6.324\ \text{kg/s} \tag{C.4}$$

The outlet air mass flow is calculated using:

$$m_{avo} = m_a(1 + w_{avo}) = 6.288\ (1 + 0.0434) = 6.561\ \text{kg/s} \tag{C.5}$$

The mean air-vapour mass flow is then calculated using Equation 4.19:

$$m_{avm} = (6.324 + 6.561)/2 = 6.443\ \text{kg/s}$$

The inlet air density is calculated using Equation A.10:

$$\begin{aligned}\rho_{avi} &= (1 + 0.00580) \times \left[1 - \frac{0.00580}{0.00580 + 0.62198}\right] \\ &\quad \times 84119/(287.08 \times 291.10) \\ &= 1.0031\ \text{kg/m}^3\end{aligned}$$

The harmonic mean density is calculated using Equation 4.20:

$$\rho_{avm} = 2\ \left(\frac{1}{1.0031} + \frac{1}{0.9278}\right)^{-1} = 0.964\ \text{kg/m}^3$$

The inlet and outlet air-vapour flow velocities are calculated:

$$v_{avi} = \frac{m_{avi}}{\rho_{avi} A_{fr}} = \frac{6.324}{1.0031 \times 2.25} = 2.802\ \text{m/s} \tag{C.6}$$

and

$$v_{avo} = \frac{m_{avo}}{\rho_{avo} A_{fr}} = \frac{6.561}{0.9278 \times 2.25} = 3.143\ \text{m/s} \tag{C.7}$$

The measured pressure loss factor is calculated using Equation 4.21:

$$\begin{aligned}K_{meas} &= \Big[2\ [56.97 - (0.9278 \times 3.143^2 - 1.0031 \times 2.802^2) \\ &\quad + (1.0031 - 0.964) \times 9.81 \times 2.0] \times 0.964 \times 2.25^2\Big]/6.443^2 \\ &= 13.274\end{aligned}$$

The corrected pressure loss factor is found by subtracting the spray zone pressure loss factor, which is calculated using Equation 2.62:

$$K_{sp} = 0.474\ \left[0.4\ \left(\frac{5.833}{6.288}\right) + 1\right] = 0.650$$

The corrected pressure loss factor is calculated using Equation 4.23:

$$K_{fd} = 13.274 - 0.650 = 12.624$$

C.4 Fill performance characteristic equations

The calculations above are repeated for all 25 test operating points in the performance test. An extract of the results are provided in Table C.3.

Table C.3: Calculation output

	$\mathbf{G_w}$ [kg/m^{2}s]	$\mathbf{G_a}$ [kg/m^{2}s]	$\mathbf{Me_{fi}}$	$\mathbf{K_{fd}}$
1	2.592	2.795	1.920	12.624
2	2.586	2.508	1.826	13.132
...	...	...	...	...
24	0.975	1.502	1.580	13.185
25	1.015	1.002	1.146	14.620

By least squares regression of the data in Table C.3, the following fill performance characteristic equations are obtained:

$$\hat{M}e_{fi} = 0.589\ L_{fi}\ G_w^{-0.277}\ G_a^{0.830} \tag{C.8}$$

$$\hat{K}_{fd} = 7.580\ L_{fi}\ G_w^{0.231}\ G_a^{-0.376} \tag{C.9}$$

Figure C.1 shows the corrected fill Merkel number and pressure loss factors at the $G_w = 2.000$ kg/m^{2}s setpoint in this fill performance test along with the regression curves representing Equations C.8 and C.9 respectively.

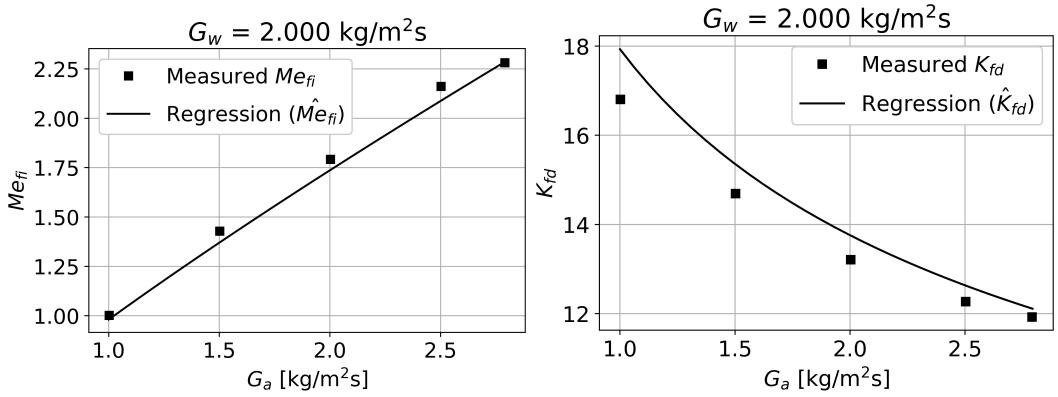

Figure C.1: Corrected Me_{fi} and K_{fd} values and regressions

Appendix D: Sample NDWCT performance prediction calculation

D.1 Calculation inputs

D.1.1 Atmospheric inputs

The atmospheric conditions during this NDWCT performance prediction calculation are taken from a single entry of the annual weather data provided for the power plant in Table F.3.

Ground-level dry-bulb temperature	T_{a1}	$= 20\ ^\circ\text{C} = 293.15$ K
Ground-level wet-bulb temperature	T_{wb}	$= 14.3\ ^\circ\text{C} = 287.45$ K
Atmospheric pressure	p_a	$= 84000$ Pa
Atmospheric temperature lapse rate	dT_a/dz	$= -0.00975$ K/m

D.1.2 NDWCT inputs

Outlet height	H_6	$= 147$ m
Outlet diameter	d_6	$= 60.85$ m
Inlet height	H_3	$= 10$ m
Inlet diameter	d_3	$= 104.5$ m
Number of supports	n_{ts}	$= 72$
Support length	L_{ts}	$= 11.6$ m
Support diameter	d_{ts}	$= 0.8$ m
Support drag coefficient	C_{Dts}	$= 1$
Inlet radius	r_i	$= 2.09$ m
Kinetic energy coefficient at outlet	α_{e6}	$= 1.01$
Water mass flow	m_w	$= 12500$ kg/s
Fill frontal area	A_{fr}	$= 8300$ m^2
Spray zone height	L_{sp}	$= 0.5$
Mean droplet diameter in the rain zone	d_d	$= 0.0050$ m
Support and contraction loss coefficient	$K_{fs} + K_{ctc}$	$= 0.5$
Water distribution system loss coefficient	K_{wd}	$= 0.5$
Fill height	L_{fi}	$= 2$ m
Drift eliminator loss coefficient	K_{de}	$= 27.4892\ Ry_{de}^{-0.14247}$

D.1.3 Fill performance inputs

The trickle fill installed in the NDWCT has the performance characteristic equations presented in Equation C.8 ($\hat{Me}_{fi}$) and C.9 ($\hat{K}_{fd}$).

D.1.4 Power plant inputs

The power plant turbine's full load is $P = 750$ MW. At an SSC water inlet temperature of 24 °C, the base heat rate is $HR_B = 8390.5$ kJ/kWh. The

percentage increase in heat rate, as a function of T_{wo} [°C] for this power plant is obtained from the 100% load curve in Figure 2.3 with a polynomial approximation of this curve being:

$$C_{HR}(T_{wo}) = -5.467 \times 10^{-6}\ T_{wo}^4 + 4.274 \times 10^{-4}\ T_{wo}^3 - 5.314 \times 10^{-4}\ T_{wo}^2 - 2.051 \times 10^{-1}\ T_{wo} + 1.152\ \% \tag{D.1}$$

D.2 Calculation results

The following results are obtained iteratively:

Water inlet temperature	T_{wi}	$= 40.425$ °C $= 313.575$ K
Water outlet temperature	T_{wo}	$= 21.459$ °C $= 294.609$ K
Air temperature above drift eliminator	T_{a5}	$= 30.023$ °C $= 303.173$ K
Mean air-flow through fill	m_{av15}	$= 14444.108$ kg/s
Air pressure above drift eliminator	p_{a5}	$= 83840.541$ Pa
Air pressure at shell outlet	p_{a6}	$= 82576.386$ Pa

D.3 Solution

D.3.1 Draught equation

D.3.1.1 Fluid and flow properties at ground level

The following air properties are calculated at ground level (point 1 in Figure 2.2) with $T_{a1} = 293.15$ K, $T_{wb1} = 287.45$ K and $p_{a1} = 84000$ Pa.

Using Equation A.13, calculate:

$$\begin{aligned} z_1 &= 10.79586\ (1 - 273.16/287.45) + 5.02808\ \log_{10}(273.16/287.45) \\ &\quad + 1.50474 \times 10^{-4}\ [1 - 10^{-8.29692\ ((287.45/273.16)-1)}] \\ &\quad + 4.2873 \times 10^{-4}\ [10^{4.76955\ (1-273.16/287.45)} - 1] + 2.786118312 \\ &= 3.212 \end{aligned}$$

Using Equation A.12 find the vapour pressure at the wet-bulb temperature:

$$p_{vwb1} = 10^{z1} = 10^{3.212} = 1628.814 \text{ Pa}$$

The ambient vapour fraction is calculated using Equation A.11:

$$\begin{aligned} w_1 &= \left(\frac{2501.6 - 2.3263\ (287.45 - 273.15)}{2501.6 + 1.8577\ (293.15 - 273.15) - 4.184\ (287.45 - 273.15)}\right) \\ &\quad \times \left(\frac{0.62509 \times 1628.814}{84000 - 1.005 \times 1628.814}\right) \\ &\quad - \left(\frac{1.00416\ (293.15 - 287.45)}{2501.6 + 1.8577\ (293.15 - 273.15) - 4.184\ (287.45 - 273.15)}\right) \\ &= 0.0100 \text{ kg/kg dry air} \end{aligned}$$

Using Equation A.10, find the density of the inlet air-vapour mixture:

$$\begin{aligned}\rho_{av1} &= (1 + 0.0100) \times \left[1 - \frac{0.0100}{0.0100 + 0.62198}\right] \times 84000/(287.08 \times 293.15) \\ &= 0.992 \text{ kg air-vapour/m}^3\end{aligned}$$

Equation A.4 is used to calculate the dynamic viscosity of dry air:

$$\begin{aligned}\mu_{a1} &= 2.287973 \times 10^{-6} + 6.259793 \times 10^{-8} \times 293.15 \\ &\quad - 3.131956 \times 10^{-11} \times 293.15^2 + 8.15038 \times 10^{-15} \times 293.15^3 \\ &= 1.815 \times 10^{-5} \text{ kg/ms}\end{aligned}$$

Equation A.9 is used to calculate the dynamic viscosity of saturated water vapour at T_{a1}:

$$\begin{aligned}\mu_{v1} &= 2.562435 \times 10^{-6} + 1.816683 \times 10^{-8} \times 293.15 \\ &\quad + 2.579066 \times 10^{-11} \times 293.15^2 - 1.067299 \times 10^{-14} \times 293.15^3 \\ &= 9.836 \times 10^{-6} \text{ kg/ms}\end{aligned}$$

Equations A.19 and A.20 are used to calculate:

$$\begin{aligned}X_{a1} &= 1/(1 + 1.608 \times 0.0100) = 0.984 \\ X_{v1} &= 0.0100/(0.0100 + 0.622) = 0.0158\end{aligned}$$

The dynamic viscosity of the air-vapour mixture is calculated using Equation A.16:

$$\begin{aligned}\mu_{av1} &= (0.984 \times 1.815 \times 10^{-5} \times 28.97^{0.5} + 0.0158 \times 9.836 \times 10^{-6} \\ &\quad \times 18.016^{0.5})/(0.984 \times 28.97^{0.5} + 0.0158 \times 18.016^{0.5}) \\ &= 1.805 \times 10^{-5} \text{ kg/ms}\end{aligned}$$

Specific heat capacities are evaluated at $(293.15+273.15)/2 = 283.15$ K. Using Equation A.2, calculate:

$$\begin{aligned}c_{pa1} &= 1.045356 \times 10^3 - 3.161783 \times 10^{-1} \times 283.15 \\ &\quad + 7.083814 \times 10^{-4} \times 283.15^2 - 2.705209 \times 10^{-7} \times 283.15^3 \\ &= 1006.483 \text{ J/kgK}\end{aligned}$$

Using Equation A.3 calculate:

$$\begin{aligned}c_{pv1} &= 1.3605 \times 10^3 + 2.31334 \times 283.15 - 2.46784 \times 10^{-10} \times 283.15^5 \\ &\quad + 5.91332 \times 10^{-13} \times 283.15^6 \\ &= 1871.099 \text{ J/kgK}\end{aligned}$$

The enthalpy of the air-vapour mixture is calculated using Equation A.14:

$$\begin{aligned}i_{ma1} &= 1006.483\ (293.15 - 273.15) + 0.0100\ [2501598.533 \\ &\quad + 1871.099\ (293.15 - 273.15)] \\ &= 45519.962 \text{ J/kg dry air}\end{aligned}$$

D.3.1.2 Fluid and flow properties above the drift eliminators

The properties above the drift eliminators (point 5 in Figure 2.2) are calculated using $T_{a5} = T_{wb5} = 303.173$ K (air-flow assumed to be saturated) and $p_{a5} = 83840.541$ Pa.

Using Equation A.13, calculate:

$$\begin{aligned} z_5 &= 10.79586\ (1 - 273.16/303.173) + 5.02808\ \log_{10}(273.16/303.173) \\ &\quad + 1.50474 \times 10^{-4}\ [1 - 10^{-8.29692\ ((303.173/273.16)-1)}] \\ &\quad + 4.2873 \times 10^{-4}\ [10^{4.76955\ (1-273.16/303.173)} - 1] + 2.786118312 \\ &= 3.628 \end{aligned}$$

Using Equation A.12 find the vapour pressure at the wet-bulb temperature:

$$p_{vwb5} = p_{v5} = 10^{z5} = 10^{3.628} = 4248.085 \text{ Pa}$$

Find the vapour fraction using Equation A.11:

$$\begin{aligned} w_5 &= \left(\frac{2501.6 - 2.3263\ (303.173 - 273.15)}{2501.6 + 1.8577\ (303.173 - 273.15) - 4.184\ (303.173 - 273.15)}\right) \\ &\quad \times \left(\frac{0.62509 \times 4248.085}{83840.541 - 1.005 \times 4248.085}\right) \\ &\quad - \left(\frac{1.00416\ (303.173 - 303.173)}{2501.6 + 1.8577\ (303.173 - 273.15) - 4.184\ (303.173 - 273.15)}\right) \\ &= 0.0334 \text{ kg/kg dry air} \end{aligned}$$

Using Equation A.10, find the density of the air-vapour mixture:

$$\begin{aligned} \rho_{av5} &= (1 + 0.0334) \times \left[1 - \frac{0.0334}{0.0334 + 0.62198}\right] 83840.541 \\ &\quad /(287.08 \times 303.173) \\ &\quad = 0.945 \text{ kg air-vapour/m}^3 \end{aligned}$$

Equation A.4 is used to calculate the dynamic viscosity of dry air:

$$\begin{aligned} \mu_{a5} &= 2.287973 \times 10^{-6} + 6.259793 \times 10^{-8} \times 303.173 \\ &\quad - 3.131956 \times 10^{-11} \times 303.173^2 + 8.15038 \times 10^{-15}\ \times 303.173^3 \\ &\quad = 1.861 \times 10^{-5} \text{ kg/ms} \end{aligned}$$

Equation A.9 is used to calculate the dynamic viscosity of saturated water vapour at T_{a5}:

$$\begin{aligned} \mu_{v5} &= 2.562435 \times 10^{-6} + 1.816683 \times 10^{-8} \times 303.173 \\ &\quad + 2.579066 \times 10^{-10} \times 303.173^2 - 1.067299 \times 10^{-14} \times 303.173^3 \\ &\quad = 1.014 \times 10^{-5} \text{ kg/ms} \end{aligned}$$

Using Equations A.19 and A.20, calculate:

$$\begin{aligned} X_{a5} &= 1/(1 + 1.608 \times 0.0334) = 0.949 \\ X_{v5} &= 0.0334/(0.0334 + 0.622) = 0.0509 \end{aligned}$$

Then calculate the dynamic viscosity of the air-vapour mixture using Equation A.16:

$$\begin{aligned}\mu_{av5} &= (0.949 \times 1.861 \times 10^{-5} \times 28.97^{0.5} + 0.0509 \times 1.014 \times 10^{-5} \\ &\quad \times 18.016^{0.5})/(0.949 \times 28.97^{0.5} + 0.0509 \times 18.016^{0.5}) \\ &= 1.827 \times 10^{-5}\text{kg/ms}\end{aligned}$$

Specific heat capacities are evaluated at $(303.173 + 273.15)/2 = 288.162$ K. Using Equation A.2, calculate:

$$\begin{aligned}c_{pa5} &= 1.045356 \times 10^{3} - 3.161783 \times 10^{-1} \times 288.162 \\ &\quad + 7.083814 \times 10^{-4} \times 288.162^{2} - 2.705209 \times 10^{-7} \times 288.162^{3} \\ &= 1006.594 \text{ J/kgK}\end{aligned}$$

Using Equation A.3, calculate:

$$\begin{aligned}c_{pv5} &= 1.3605 \times 10^{3} + 2.31334 \times 288.162 - 2.46784 \times 10^{-10} \times 288.162^{5} \\ &\quad + 5.91332 \times 10^{-13} \times 288.162^{6} \\ &= 1875.339 \text{ J/kgK}\end{aligned}$$

The enthalpy of the air-vapour mixture is calculated using Equation A.14:

$$\begin{aligned}i_{ma5} &= 1006.594\ (303.173 - 273.15) + 0.0334\ [2501598.533 \\ &\quad + 1875.339\ (303.173 - 273.15)] \\ &= 115582.307 \text{ J/kg dry air}\end{aligned}$$

D.3.1.3 Additional properties

The air-vapour mixture density at the fill is calculated as the harmonic mean between the inlet and above the drift eliminators using Equation 2.58:

$$\begin{aligned}\rho_{av15} &= 2/(1/\rho_{av1} + 1/\rho_{av5}) = 2/(1/0.992 + 1/0.945) \\ &= 0.968 \text{ kg/m}^3\end{aligned}$$

The dry-air mass flow rate is calculated using:

$$\begin{aligned}m_a &= 2 \times m_{av15}/(2 + w_1 + w_5) \\ &= 2 \times 14444.108/(2 + 0.0100 + 0.0334) \\ &= 14137.523 \text{ kg/s}\end{aligned} \tag{D.2}$$

and the air-vapour mass flow rates at points 1 and 5 are calculated using:

$$m_{av1} = m_a(1 + w_1) = 14137.523\ (1 + 0.0100) = 14278.899 \text{ kg/s} \tag{D.3}$$

$$m_{av5} = m_a(1 + w_5) = 14137.523\ (1 + 0.0334) = 14609.318 \text{ kg/s} \tag{D.4}$$

The fill water and air mass fluxes are calculated using Equation 4.13 and 4.18, respectively:

$$G_w = m_w/A_{fr} = 12500/8300 = 1.506 \text{ kg/m}^2\text{s} \tag{D.5}$$

$$G_a = m_a/A_{fr} = 14137.523/8300 = 1.703 \text{ kg/m}^2\text{s} \tag{D.6}$$

D.3.1.4 Shell supports

The fill referred shell support pressure loss factors is calculated using Equation 2.35:

$$\begin{aligned} K_{tsfi} &= [1 \times 11.6 \times 0.8 \times 72 \times 8300^2/(\pi \times 104.5 \times 10)^3] \\ &\quad \times (0.968/0.992) \times (14278.899/14444.108)^2 \\ &= 1.240 \end{aligned}$$

D.3.1.5 Shell inlet

The inlet pressure loss coefficient is calculated using Equation 2.38[1]:

$$\begin{aligned} K_{ct(norz)} &= 0.011266 \times e^{0.093 \times 104.5/10} \times 13.730^2 - 0.3105 \\ &\quad \times e^{0.1085 \times 104.5/10} \times 13.730 - 1.7522 + 4.5614 \times e^{0.131 \times 104.5/10} \\ &\quad + \sinh^{-1}\Big[\{(10970.2 \times e^{-0.2442 \times 13.730} + 1391.3) \\ &\quad /(104.5/10 - 15.7258) + 1205.54 \times e^{-0.23 \times 13.730} + 109.31\} \\ &\quad \times \{2 \times 2.09/104.5 - 0.01942/(104.5/10 - 27.929) - 0.016866\}\Big] \\ &\quad = 6.388 \end{aligned}$$

The loss coefficient is referred to the fill using Equation 2.39:

$$\begin{aligned} K_{ctfi(norz)} &= 6.388 \times (0.968/0.992) \times (14278.899/14444.108)^2 \\ &\quad \times \left(4 \times 8300/(\pi \times 104.5^2)\right)^2 \\ &\quad = 5.703 \end{aligned}$$

The fill referred loss coefficient is corrected with the rain zone correction factor, calculated using Equation 2.40:

$$\begin{aligned} C_{rz} &= \big[0.2394 + 80.1\ (0.0954/(104.5/10) + 0.0050) \times e^{0.395 \times 1.506/1.703} \\ &\quad - 0.3195\ (1.506/1.703) - 966\ (0.0050/(104.5/10)) \times e^{0.686 \times 1.506/1.703}\big] \\ &\quad \times (1 - 0.06825 \times 1.506) \times 13.775^{0.09667} \times e^{8.7434\ (1/104.5 - 0.01)} \\ &\quad = 0.822 \end{aligned}$$

The corrected fill referred inlet pressure loss coefficient is calculated using Equation 2.42:

$$K_{ctfi} = 0.822 \times 5.703 = 4.689$$

[1]The value $K_{fi} = 13.730$, used here, is obtained from Equation D.10 on page 111. Although it is calculated after $K_{ct(norz)}$, the order of calculations presented here is maintained for clarity.

D.3.1.6 Rain zone

The density of the outlet water is calculated using Equation A.6:

$$\begin{aligned}\rho_{wo} &= (1.49343 \times 10^{-3} - 3.7164 \times 10^{-6} \times 294.609 + 7.09782 \times 10^{-9} \\ &\quad \times 294.609^2 - 1.90321 \times 10^{-20} \times 294.609^6)^{-1} \\ &= 997.852 \text{ kg/m}^3\end{aligned}$$

Surface tension of saturated liquid water using Equation A.7:

$$\begin{aligned}\sigma_{wo} &= 5.148103 \times 10^{-2} + 3.998714 \times 10^{-4} \times 294.609 \\ &\quad - 1.4721869 \times 10^{-6} \times 294.609^2 + 1.21405335 \times 10^{-9} \times 294.609^3 \\ &= 0.0726 \text{ N/m}\end{aligned}$$

Coefficients are calculated using Equations 2.48 through 2.51:

$$a_\mu = 3.061 \times 10^{-6} \left[997.852^4 \times 9.81^9 / 0.0726\right]^{0.25} = 1.00235$$
$$a_\rho = 998.0/997.852 = 1.00015$$
$$a_v = 73.298 \left[9.81^5 \times 0.0726^3 / 997.852^3\right]^{0.25} = 1.00203$$
$$a_L = 6.122 \left[9.81 \times 0.0726/997.852\right]^{0.25} = 1.00048$$

Flow velocities using Equations 2.45, 2.46 and 2.47:

$$v_{w3} = 1.506/997.852 = 0.00151 \text{ m/s}$$
$$v_{av3} = 14278.899/(0.992 \times 8300) = 1.734 \text{ m/s}$$
$$v_{azo} = 14137.523/(0.992 \times 8300) = 1.717 \text{ m/s}$$

The coefficient k is calculated using Equation 2.44:

$$\begin{aligned}k &= (0.8449 \ln(1.00048 \times 104.5/2) - 2.312) \\ &\quad \times (0.3724 \ln(1.00200 \times 1.734) + 0.7263) \\ &\quad \times \ln(206.757 \ (1.00048 \times 10)^{-2.8344} + 0.43) \\ &= -0.299\end{aligned}$$

The rain zone pressure loss factor is calculated using Equation 2.43:

$$\begin{aligned}K_{rz} &= 3 \times 1.00200 \times 0.00151 \ (10/0.0050) \times \Big[0.2246 - 0.31467 \\ &\quad \times 1.00015 \times 0.992 + 5263.04 \times 1.00235 \times 1.805 \times 10^{-5} \\ &\quad + 0.775526 \times (1.4824163 \times e^{71.52 \times 1.00048 \times 0.0050} - 0.91) \\ &\quad \times (0.39064 \times e^{0.010912 \times 1.00048 \times 104.5} - 0.17) \\ &\quad \times (2.0892 \ (1.00200 \times 1.734)^{-1.3944} + 0.14) \times e^{-0.299}\Big] \\ &= 7.424\end{aligned}$$

The fill referred rain zone pressure loss coefficient is calculated using Equation 2.52:

$$\begin{aligned} K_{rzfi} &= 7.427\ (0.968/0.992) \times (4 \times 8300/(\pi\ 104.5^2))^2 \\ &\quad \times (14278.899/14444.108)^2 \\ &= 6.628 \end{aligned}$$

D.3.1.7 Fill supports and contraction

The fill referred pressure loss coefficient for the fill supports and contraction is calculated using Equation 2.53:

$$(K_{fs} + K_{ctc})_{fi} = 0.5\ (0.968/0.992) \times (14278.899/14444.108)^2 = 0.477$$

D.3.1.8 Fill loss coefficient

The fill loss coefficient is calculated using Equation C.9:

$$K_{fd} = 7.580 \times 2 \times 1.506^{0.231} \times 1.703^{-0.376} = 13.635$$

Air-vapour mass fluxes are calculated using:

$$G_{av1} = m_{av1}/A_{fr} = 14278.899/8300 = 1.720\ \text{kg/m}^2\text{s} \tag{D.7}$$

$$G_{av5} = m_{av5}/A_{fr} = 14609.318/8300 = 1.760\ \text{kg/m}^2\text{s} \tag{D.8}$$

$$G_{av15} = m_{av15}/A_{fr} = 14444.108/8300 = 1.740\ \text{kg/m}^2\text{s} \tag{D.9}$$

The fill static pressure loss coefficient is calculated using Equation 2.56:

$$\begin{aligned} K_{fi} &= 13.635 + (1.760^2/0.945 - 1.720^2/0.992)/(1.740^2/0.968) \\ &= 13.730 \end{aligned} \tag{D.10}$$

D.3.1.9 Expansion loss coefficient

The expansion loss coefficient is calculated using Equation 2.60:

$$K_{cte} = \left(1 - \frac{8300}{\pi \times 104.5^2/4}\right)^2 = 0.00104$$

This is referred to the fill using Equation 2.61:

$$K_{ctefi} = 0.00104 \times (0.968/0.945) \times (14609.318/14444.108)^2 = 0.00109$$

D.3.1.10 Spray zone loss coefficient

The spray zone loss coefficient is calculated using Equation 2.62:

$$K_{sp} = 0.5\ [0.4\ (1.506/1.703) + 1] = 0.677$$

This is referred to the fill using Equation 2.63:

$$K_{spfi} = 0.677\ (0.968/0.945) \times (14609.318/14444.108)^2 = 0.709$$

D.3.1.11 Water distribution system loss coefficient

The fill referred water distribution pressure loss coefficient is calculated using Equation 2.64:

$$K_{wdfi} = 0.5\ (0.968/0.945) \times (14609.318/14444.108)^2 = 0.524$$

D.3.1.12 Drift eliminators loss coefficient

The characteristic flow parameter of the drift eliminators is calculated using Equation 2.66:

$$Ry_{de} = 14609.318/(1.827 \times 10^{-5} \times 8300) = 96338.84\ \text{m}^{-1}$$

The drift eliminator loss coefficient is calculated using the equation supplied in Section D.1.2:

$$K_{de} = 27.4892 \times 96338.84^{-0.14247} = 5.359$$

This is referred to the fill using Equation 2.67:

$$K_{defi} = 5.359\ (0.968/0.945) \times (14609.318/14444.108)^2 = 5.617$$

D.3.1.13 Shell outlet parameters

The following parameters are calculated with specific heat capacities evaluated at $(303.173 + 273.15\ \text{K})/2 = 288.162\ \text{K}$. The specific heat capacity of the air-vapour mixture above the drift eliminators, using Equation 2.70:

$$c_{pma5} = 1006.594 + 0.0334 \times 1875.339 = 1069.178\ \text{kJ/kgK}$$

The specific heat capacity of water, using Equation A.5:

$$\begin{aligned} c_{pw5} &= 8155.99 - 28.0627 \times 288.162 + 0.0511283 \times 288.162^2 \\ &\quad - 2.17582 \times 10^{-13} \times 288.162^6 \\ &= 4190.367\ \text{J/kgK} \end{aligned}$$

Calculate using Equation 2.71:

$$\begin{aligned} i_e &= 2501598.533 - (4190.367 - 1875.339) \times (303.173 - 273.15) \\ &= 2432095.547\ \text{kJ/kg} \end{aligned}$$

The temperature lapse rate in the column of air above the drift eliminators is calculated using Equation 2.69:

$$\begin{aligned} \xi_{Ta5} = &\Big[-(1 + 0.0334) \times 9.81 \Big] / \Big[1069.178 + 3.6693 \times 10^{-8} \times 0.0334^2 \\ &\times 83840.541 \times e^{5406.1915/303.173} \times 2432087.652/303.173^2 \Big] \\ &\times \Big[1 + 0.42216 \times 10^{-11} \times 0.0334^2 \times 83840.541 \times e^{5406.1915/303.173} \\ &\times 2432095.547/((0.0334 + 0.622) \times 287.08\ 303.173) \Big] \\ &= -0.00321\ \text{K/m} \end{aligned}$$

The temperature at the shell outlet is calculated using this lapse rate:

$$\begin{aligned} T_{a6} &= T_{a5} + \xi_{Ta5}(H_6 - H_3 - L_{fi} - L_{sp}) \\ &= 303.173 + (-0.00321) \times (147 - 10 - 2 - 0.5) \\ &= 302.741 \text{ K} \end{aligned} \tag{D.11}$$

The density at the cooling tower outlet is calculated using Equation A.10:

$$\begin{aligned} \rho_{av6} &= (1 + 0.0334) \times \left[1 - \frac{0.0334}{0.0334 + 0.62198}\right] \\ &\quad \times 82576.385/(287.08 \times 302.744) \\ &= 0.932 \text{ kg/m}^3 \end{aligned}$$

The temperature at the outlet elevation outside the shell is calculated using the atmospheric temperature lapse rate:

$$\begin{aligned} T_{a7} &= T_{a1} + dT_a/dz \; H_6 = 293.15 + (-0.00975) \times 147 \\ &= 291.717 \text{ K} \end{aligned} \tag{D.12}$$

The air pressure at the outlet elevation outside the shell is calculated using Equation 2.77:

$$\begin{aligned} p_{a7} &= 84000 \; [1 - 0.00975 \times 147/293.15]^{3.5 \; (1+0.0100) \times \left(1 - \frac{0.0100}{0.0100 + 0.62198}\right)} \\ &= 82579.830 \text{ Pa} \end{aligned}$$

The density at the outlet elevation outside the shell is calculated using Equation A.10, with the vapour fraction being the same as at ground level:

$$\begin{aligned} \rho_{av7} &= (1 + 0.0100) \times \left[1 - \frac{0.0100}{0.0100 + 0.62198}\right] \times 82579.830 \\ &\quad /(287.08 \times 291.717) \\ &= 0.980 \text{ kg air-vapour/m}^3 \end{aligned}$$

The densimetric Froude number is calculated using Equation 2.73:

$$Fr_D = \frac{(14609.318/(\pi \times 60.85^2/4))^2}{0.932 \; (0.980 - 0.932) \times 9.81 \times 60.85} = 0.939$$

The shell outlet pressure is calculated using Equation 2.74:

$$\begin{aligned} p_{a6} &= 82579.830 + (0.02 \times 0.939^{-1.5} - 0.14/0.939) \\ &\quad \times (14609.318/(\pi \; 60.85^2/4))^2/0.932 \\ &= 82576.386 \text{ Pa} \end{aligned}$$

This confirms the correct iterative solution for p_{a6}.

D.3.1.14 Draught equation solution

The sum of pressure loss coefficients is calculated as:

$$\begin{aligned}\sum K_{fi} &= (K_{ts} + K_{ct} + K_{rz} + K_{fs} + K_{ctc} + K_{fi} + K_{cte} + K_{sp} \\ &\quad + K_{wd} + K_{de})_{fi} \\ &= 1.240 + 4.688 + 6.628 + 0.477 + 13.730 + 0.00109 \\ &\quad + 0.709 + 0.524 + 5.617 \\ &= 33.615\end{aligned} \tag{D.13}$$

The air pressure above the drift eliminators is calculated using Equation 2.81:

$$\begin{aligned}p_{a5} &= 84000 \left[1 - 0.00975 \times \frac{10 + 2/2}{293.15}\right]^{3.5\ (1+0.0100)\times\left(1-\frac{0.0100}{0.0100+0.62198}\right)} \\ &\quad - 33.615\ (14444.108/8300)^2/(2 \times 0.968) \\ &= 83840.541\ \text{Pa}\end{aligned}$$

This confirms that the iterative solution of p_{a5} is correct.

The draught equation, Equation 2.82, is calculated as:

$$\begin{aligned}&84000 \left[\left(1 - 0.00975\ \left(10 + \frac{2}{2}\right)/293.15\right)^{3.5\ (1+0.0100)\times\left(1-\frac{0.0100}{0.0100+0.62198}\right)}\right. \\ &\times \left(1 + (-0.00321) \times \left(147 - 10 - \frac{2}{2}\right)\right. \\ &\left./303.173\right)^{-0.021233\ (1+0.0334)/(-0.00321\ (0.0334+0.622))} \\ &\left. - (1 - 0.00975 \times 147/293.15)^{3.5\ (1+0.0100)\times\left(1-\frac{0.0100}{0.0100+0.62198}\right)}\right] \\ &- (0.02 \times 0.938^{-1.5} - 0.14/0.938) \times \left(14609.318/(\pi\ 60.85^2/4)\right)^2/0.932 \\ &= \left[33.661\ (14444.108/8300)^2/(2 \times 0.968)\right] \\ &\times \left(1 + (-0.00321) \times \left(147 - 10 - \frac{2}{2}\right)\right. \\ &\left./303.173\right)^{-0.021233\ (1+0.0334)/(-0.00321\ (0.0334+0.622))} \\ &+ 1.01 \times (14609.318/(\pi \times 60.85^2/4))^2/(2 \times 0.932) \\ &65.483\ \text{Pa} = 65.483\ \text{Pa}\end{aligned}$$

Which confirms that the iterative solution of m_{av15} is correct.

D.3.2 Transfer equation

D.3.2.1 Rain zone Merkel number

The water vapour diffusion coefficient is calculated using Equation 2.86:

$$D_1 = \left[0.04357 \times 293.15^{1.5} \left(\frac{1}{28.97} + \frac{1}{18.016}\right)^{0.5}\right] / \left[84000 \left(29.9^{0.333} + 18.8^{0.333}\right)^2\right] = 2.357 \times 10^{-5} \text{ m}^2/\text{s}$$

The Schmidt number is calculated with Equation 2.85:

$$Sc_1 = 1.805 \times 10^{-5}/(0.992 \times 2.357 \times 10^{-5}) = 0.772$$

The vapour fraction of the saturated air at T_{wo} is calculated using Equation A.11 at $T_{db} = T_{wb} = T_{wo} = 294.609$ K and $p_{a1} = 84000$ Pa:

$$w_{s1} = 0.0196 \text{ kg/kg dry air}$$

The Merkel number for the rain zone is calculated using Equation 2.84:

$$\begin{aligned} Me_{rz} = 12 &\times \left(\frac{2.357 \times 10^{-5}}{1.734 \times 0.0050}\right) \times \left(\frac{10}{0.0050}\right) \\ &\times \left(\frac{84000}{461.52 \times 293.15 \times 997.855}\right) \times 0.772^{0.33} \\ &\times \left[\ln\left(\frac{0.0196 + 0.622}{0.0100 + 0.622}\right) / (0.0196 - 0.0100)\right] \times \Bigg[0.90757 \\ &\times 1.00015 \times 0.992 - 30341.04 \times 1.00235 \times 1.805 \times 10^{-5} \\ &- 0.37564 + 4.04016 \left[\left(0.55 + 41.7215 \left(1.00048 \times 0.0050\right)^{0.80043}\right)\right. \\ &\times \left(0.713 + 3.741 \left(1.00048 \times 10\right)^{-1.23456}\right) \\ &\times \left(3.11 \times e^{0.15 \times 1.00200 \times 1.734} - 3.13\right) \\ &\times \left.\left(e^{(5.3759 \times e^{-0.2092 \times 1.00048 \times 10}) \times \ln(0.3719 \times e^{0.0019055 \times 1.00048 \times 104.5} + 0.55)}\right)\right]\Bigg] \\ &= 0.229 \end{aligned}$$

D.3.2.2 Fill Merkel number

The fill Merkel number is calculated using Equation C.8:

$$Me_{fi} = 0.589 \times 2 \times 1.506^{-0.277} \times 1.703^{0.830} = 1.637 \tag{D.14}$$

D.3.2.3 Spray zone Merkel number

The spray zone Merkel number is calculated using Equation 2.89:

$$Me_{sp} = 0.2 \times 0.5 \times \left(\frac{1.703}{1.506}\right)^{0.5} = 0.106$$

D.3.2.4 NDWCT Merkel number

The NDWCT Merkel number is calculated using the Chebychev integral in Appendix B.1. The method is the same as in Appendix C.3.3 and the calculated value is:

$$Me_{NDWCT} = 1.973$$

The transfer equation, Equation 2.83 is calculated as:

$$1.973 = 0.229 + 1.637 + 0.106$$

which confirms that the iterative solution of T_{wo} is correct:

D.3.3 Energy equation

The energy equation, Equation 2.90, is calculated as:

$$14137.523\ (115582.307 - 45519.962) = 12500 \times 4178.231 \times (313.75 - 294.609)$$

which confirms that the iterative solution of T_{a5} is correct, with $Q_{NDWCT} = 990.508$ MW.

D.3.4 Heat rate correction equation

The percentage heat rate correction is calculated using Equation D.1:

$$\begin{aligned} C_{HR}(21.459) &= -5.467 \times 10^{-6} \times 21.459^4 + 4.274 \times 10^{-4} \times 21.459^3 \\ &\quad - 5.314 \times 10^{-4} \times 21.459^2 - 2.051 \times 10^{-1} \times 21.459 + 1.152 \\ &= -0.430\ \% \end{aligned}$$

The heat rate is calculated using Equation 2.91:

$$HR(21.459) = 8390.5\ (100 - 0.430)/100 = 8354.42\ \text{kJ/kWh}$$

The rate of heat rejection by the NDWCT is calculated using Equation 2.92

$$Q_{NDWCT} = 750\ \ (8354.42/3600 - 1) = 990.508\ \text{MW}$$

Which is the same as the value obtained in Appendix D.3.3, confirming that the iterative solution of T_{wi} is correct.

Appendix E: Example of fill and NDWCT performance uncertainty calculation

This uncertainty calculation is performed for the fill performance test and the NDWCT performance prediction calculation presented in Appendix C and D respectively. Note that the units of uncertainties are the same as the measurement or result. The units of sensitivity indexes are neglected for formatting purposes.

E.1 Measurement uncertainties

The uncertainties of individual measurements are calculated for the measured values at the test operating point in Appendix C.

E.1.1 Calculation inputs

The inputs to the measurement random uncertainty calculation is the measured data in Table C.1. The inputs to the measurement systematic uncertainty calculation are the equipment uncertainty equations in Section 4.2.3 and the measurement means at the specific test operating point in Table C.2.

E.1.2 Random uncertainties

The measurement random uncertainty for each measured parameter at this test operating point is calculated using Equation 5.2 and presented in Table E.1.

Table E.1: Measurement random uncertainty

	$\overline{\mathbf{V}}_{\mathbf{wi}}$	$\overline{\mathbf{\Delta p}}_{\mathbf{pnz}}$	$\overline{\mathbf{\Delta p}}_{\mathbf{nzl}}$	$\overline{\mathbf{\Delta p}}_{\mathbf{fi}}$	$\overline{\mathbf{T}}_{\mathbf{wi}}$	$\overline{\mathbf{T}}_{\mathbf{wo}}$	$\overline{\mathbf{T}}_{\mathbf{db}}$	$\overline{\mathbf{T}}_{\mathbf{wb}}$	$\overline{\mathbf{V}}_{\mathbf{byp}}$	$\overline{\mathbf{V}}_{\mathbf{wall}}$	$\overline{\mathbf{p}}_{\mathbf{a}}$
	[m³/hr]	**[Pa]**	**[Pa]**	**[Pa]**	**[°C]**	**[°C]**	**[°C]**	**[°C]**	**[L/s]**	**[L/s]**	**[kPa]**
$s_{\overline{X}}$	0.00952	0.593	2.286	0.317	0.0461	0.191	0.0138	0.0146	0[1]	0[1]	0.000761

E.1.3 Systematic measurement uncertainties

E.1.3.1 Water inflow systematic uncertainty

The instrument systematic uncertainty is calculated using Equation 4.4:

$$b_{\overline{V}_{wi_{instr}}} = [0.005 \times 21.56 + 0.0416]/2 = 0.0747 \text{ m}^3/\text{hr}$$

The instrument current output uncertainty is supplied by Equation 4.5 as $b_{\overline{V}_{wi_{curr}}} = 0.00703$ m^3/hr. The uncertainty of the I/O system is calculated

[1] See Section 4.2.3.5

using Equation 4.1:

$$b_{\overline{V}_{wi_{IO}}} = [0.005\ (45 - 0)]\ /2 = 0.113\ \text{m}^3/\text{hr}$$

Uncertainty due to digitization is calculated using Equation 4.2:

$$b_{\overline{V}_{wi_{digi}}} = \frac{45 - 0}{27648} = 0.00163\ \text{m}^3/\text{hr}$$

These values are combined using Equation 5.3

$$b_{\overline{V}_{wi}} = \left[0.0747^2 + 0.00703^2 + 0.113^2 + 0.00163^2\right]^{0.5} = 0.135\ \text{m}^3/\text{hr}$$

E.1.3.2 Pressure difference uncertainty

The uncertainty values for all pressure difference measurements are same and are independent of the measured value. The instrument uncertainty is supplied by Equation 4.6 as $b_{\overline{\Delta p}_{instr}} = 2.967$ Pa and the instrument current output uncertainty is provided by Equation 4.7 as $b_{\overline{\Delta p}_{curr}} = 0.0188$ Pa.

The uncertainty of the I/O system is calculated using Equation 4.1:

$$b_{\overline{\Delta p}_{IO}} = [0.005\ (100 - (-500))]\ /2 = 1.5\ \text{Pa}$$

The uncertainty due to digitization is calculated using Equation 4.2:

$$b_{\overline{\Delta p}_{digi}} = \frac{500 - (-100)}{27648} = 0.0217\ \text{Pa}$$

These values are combined using Equation 5.3:

$$b_{\overline{\Delta p}} = \left[2.967^2 + 0.0188^2 + 1.5^2 + 0.0217^2\right]^{0.5} = 3.325\ \text{Pa}$$

E.1.3.3 Temperature measurement uncertainty

The temperature measurement systematic uncertainty calculations are all calculated using the same equations, with only the measured values resulting in differences in the RTD calculated uncertainty ($b_{\overline{T}_{RTD}}$). The RTD uncertainty calculation and the resulting temperature measurement uncertainty is shown for the water inlet temperature (T_{wi}) only, with all temperature measurement uncertainties summarised in Table E.2.

The RTD uncertainty is calculated using Equation 4.8:

$$b_{\overline{T}_{wi_{RTD}}} = [0.15 + 0.002 \times |49.69|]\ /2 = 0.125\ ^\circ\text{C}$$

The RTD converters' uncertainty for all measurements is provided by Equation 4.9 as $b_{\overline{T}_{converter}} = 0.05\ ^\circ$C.

The uncertainty of the I/O system is calculated using Equation 4.1:

$$b_{\overline{T}_{IO}} = [0.005\ (100 - (-10))]\ /2 = 0.275\ ^\circ\text{C}$$

The uncertainty due to digitization is calculated using Equation 4.2:

$$b_{\overline{T}_{digi}} = \frac{100 - (-10)}{27648} = 0.00398\ ^\circ\text{C}$$

These values are combined using Equation 5.3:

$$b_{\overline{T}_{wi}} = \left[0.125^2 + 0.05^2 + 0.275^2 + 0.00398^2\right]^{0.5} = 0.306\ ^\circ\text{C}$$

Table E.2: Temperature measurement systematic uncertainties

		$\mathbf{T_{wi}}$	$\mathbf{T_{wo}}$	$\mathbf{T_{db}}$	$\mathbf{T_{wb}}$
		[°C]	**[°C]**	**[°C]**	**[°C]**
$b_{\overline{T}_{RTD}}$	Eq. 4.8	0.125	0.0954	0.0929	0.0848
$b_{\overline{T}}$	Eq. 5.3	0.306	0.295	0.295	0.292

E.1.3.4 Ambient air pressure

The ambient air pressure instrument systematic uncertainty is provided by Equation 4.10 as $b_{\overline{p}_{a_{instr}}} = 0.722$ kPa. The uncertainty of the current provided by the instrument is provided by Equation 4.11 as $b_{\overline{p}_{a_{curr}}} = 0.0025$ kPa.

The uncertainty of the analogue input to the central PLC is calculated using Equation 4.3:

$$b_{\overline{p}_{a_{PLC}}} = \left[0.003\ (140 - 60)\right]/2 = 0.12\ \text{kPa}$$

The uncertainty due to digitization is calculated using Equation 4.2:

$$b_{\overline{p}_{a_{digi}}} = \frac{140 - 60}{27648} = 0.00289\ \text{kPa}$$

These values are combined using Equation 5.3:

$$b_{\overline{p}_a} = \left[0.722^2 + 0.0025^2 + 0.12^2 + 0.00289^2\right]^{0.5} = 0.732\ \text{kPa}$$

E.2 Test operating point result uncertainties

The random and systematic result uncertainties are calculated similarly for all results. The sensitivity indexes are calculated numerically for all results, even in the cases where the sensitivity to the measurement is zero. This greatly simplifies the programming of the required numerical differentiation functions. Table E.3 provides a summary of both the sensitivity indexes and random and systematic measurement uncertainties used to calculate the results uncertainties.

The random and systematic result uncertainties at this test operating point are calculated using Equations 5.4 and 5.5 and are displayed in Table E.4. The calculation of the measurement and result random and systematic uncertainties is repeated for every test operating point in the fill performance test.

E.3 Regression uncertainties

The NDWCT operating point for which the regression uncertainties are calculated are obtained from the NDWCT performance prediction calculation:

Table E.3: Summary of the sensitivity indexes and random and systematic uncertainties used in the result uncertainty calculation

$\overline{\mathbf{X}}$	$\frac{\partial \mathbf{G_w}}{\partial \overline{\mathbf{X}}}$	$\frac{\partial \mathbf{G_a}}{\partial \overline{\mathbf{X}}}$	$\frac{\partial \mathbf{Me_{fi}}}{\partial \overline{\mathbf{X}}}$	$\frac{\partial \mathbf{K_{fd}}}{\partial \overline{\mathbf{X}}}$	$\mathbf{b}_{\overline{\mathbf{X}}}$	$\mathbf{s}_{\overline{\mathbf{X}}}$
$\overline{V}_{wi}$	0.122	-0.00999	0.0672	0.0408	0.135	0.010
$\overline{\Delta p}_{pnz}$	0	-1.853×10^{-5}	8.806×10^{-6}	9.491×10^{-5}	3.325	0.593
$\overline{\Delta p}_{nzl}$	0	0.00352	-0.001673	-0.0328	3.325	2.286
$\overline{\Delta p}_{fi}$	0	0	-2.267×10^{-5}	0.235	3.325	0.317
$\overline{T}_{wi}$	-0.00119	-0.00714	0.0263	0.0292	0.306	0.0461
$\overline{T}_{wo}$	0	0.00725	-0.289	-0.0297	0.295	0.191
$\overline{T}_{db}$	0	2.841×10^{-5}	-0.000621	-0.0187	0.295	0.0138
$\overline{T}_{wb}$	0	-0.00484	0.113	0.00602	0.292	0.0146
$\overline{V}_{byp}$	-0.439	0.0360	-0.242	-0.147	0	0
$\overline{V}_{wall}$	-0.439	0.0360	-0.242	-0.147	0	0
$\overline{p}_a$	0	0.0178	0.0250	-0.000553	0.732	0.000761

Table E.4: Test operating point result random and systematic uncertainties

	$\mathbf{G_w}$ [$\mathbf{kg/m^2s}$]	$\mathbf{G_a}$ [$\mathbf{kg/m^2s}$]	$\mathbf{Me_{fi}}$ [–]	$\mathbf{K_{fd}}$ [–]
s_R	0.00116	0.00817	0.0555	0.106
b_R	0.0165	0.0197	0.110	0.797

from Equations D.5 and D.6 respectively obtain $G_w = 1.506$ kg/m^{2}s and $G_a = 1.703$ kg/m^{2}s. The operating Merkel number and pressure loss factor regression uncertainties are calculated using Equation 5.12. Due to the large number of summation terms , it is impractical to show full examples and only the calculated terms of Equation 5.12 are displayed:

$$\begin{aligned} u_{\hat{Me}_{fi}} = \Big[& 3.724 \times 10^{-4} + 6.610 \times 10^{-3} + 2.059 \times 10^{-6} \\ & + 2.206 \times 10^{-5} + 1.065 \times 10^{-4} + 3.096 \times 10^{-5} \\ & + 3.850 \times 10^{-4} + 7.751 \times 10^{-4} + 9.408 \times 10^{-6} \\ & + 6.419 \times 10^{-9} + 3.087 \times 10^{-7} + 3.878 \times 10^{-5} \Big]^{0.5} \\ & = 0.0913 \end{aligned} \tag{E.1}$$

$$\begin{aligned} u_{\hat{K}_{fd}} = \Big[& 6.767 \times 10^{-1} + 5.941 + 8.723 \times 10^{-5} + 1.066 \times 10^{-3} \\ & - 8.911 \times 10^{-4} + 6.965 \times 10^{-4} + 5.870 \times 10^{-3} \\ & - 6.359 \times 10^{-2} + 2.479 \times 10^{-4} + 3.447 \times 10^{-7} \\ & + 5.168 \times 10^{-6} + 3.575 \times 10^{-4} \Big]^{0.5} \\ & = 2.562 \end{aligned} \tag{E.2}$$

The regression uncertainty calculations may be repeated for multiple instances over a range of G_a values to generate a visual representation of the regression uncertainty as seen in Figure E.1 (typically 20-30 instances provide a smooth set of regression uncertainty bounds). Also visible in Figure E.1 are the corrected Me_{fi} and K_{fd} values and uncertainties which are close to the calculation G_w of 1.506 kg/m^{2}s: the values and uncertainties at the test setpoint of $G_w = 1.5$ kg/m^{2}s are shown.

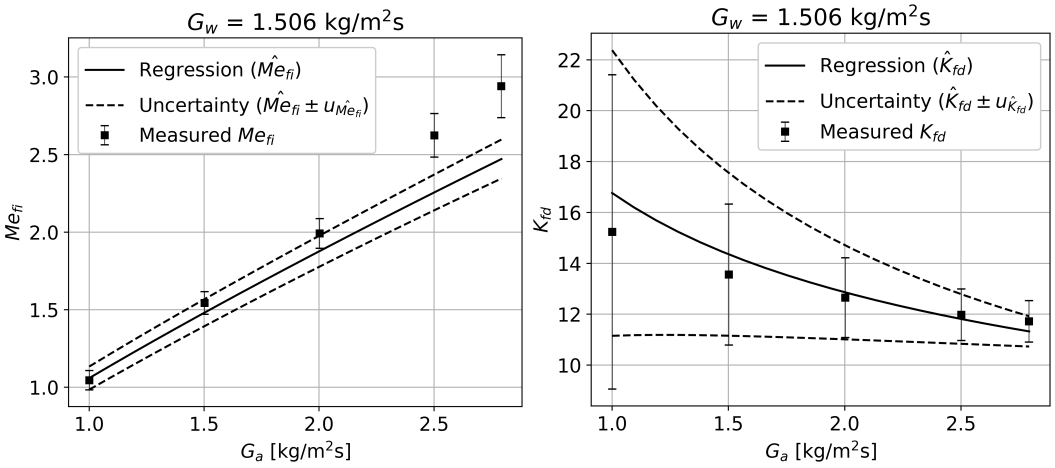

(a) Merkel number regression and uncertainties

(b) Pressure loss factor regression and uncertainties

Figure E.1: Measured values, regressions and their uncertainties

If the correlated uncertainty terms in Equation 5.12 are neglected, the regression uncertainties are calculated as:

$$u^*_{\hat{Me}_{fi}} = 0.0211 \tag{E.3}$$

$$u^*_{\hat{K}_{fd}} = 0.823 \tag{E.4}$$

The implication of these values is discussed in Section 5.5. **From here 28/10**

E.4 NDWCT performance prediction uncertainty

The sensitivity indexes are calculated numerically using Equations 5.15 and 5.16:

$$\theta_{\hat{Me}_{fi}} = \frac{\partial T_{wo}}{\partial \hat{Me}_{fi}} = -3.202$$

$$\theta_{\hat{K}_{fd}} = \frac{\partial T_{wo}}{\partial \hat{K}_{fd}} = 0.0732$$

The covariance between $\hat{M}e_{fi}$ and $\hat{K}_{fd}$ is calculated using Equation 5.17. The large number of summed terns again prevent the display of a full calculation and only the result is shown:

$$\sum_{l=1}^{L} b_{\hat{M}e_{fi_l}\hat{K}_{fd_l}} = 0.0127$$

The NDWCT water outlet temperature uncertainty is calculated using Equation 5.14:

$$\begin{aligned} u_{T_{wo}} &= \left[(-3.202 \times 0.0913)^2 + (0.0732 \times 2.562)^2 \right. \\ &\quad \left. + 2\,(-3.202) \times 0.0732 \times 0.0127\right]^{0.5} \\ &= 0.339\ ^\circ\text{C} \end{aligned} \tag{E.5}$$

If the correlated uncertainties are neglected in this equation, the resulting NDWCT performance uncertainty, at the 68% confidence level, is:

$$\begin{aligned} u^*_{T_{wo}} &= \left[(\theta_{\hat{M}e_{fi}} u_{\hat{M}e_{fi}})^2 + (\theta_{\hat{K}_{fd}} u_{\hat{K}_{fd}})^2\right]^{0.5} \\ &= \left[(-3.202 \times 0.0913)^2 + (0.0732 \times 2.562)^2\right]^{0.5} \\ &= 0.347\ ^\circ\text{C} \end{aligned} \tag{E.6}$$

Appendix F: Sample calculation using fouling factors

F.1 Sample calculation of NDWCT performance prediction using fill fouling factors

In this example, the fouling factors for the fouled condition of a fill, the NDWCT performance prediction using these fouling factors and the fouling factor and NDWCT performance uncertainties are calculated. The fouled condition performance test of the fill is the same performance test analysed in Appendix C. The initial performance test is designated as time $t = 0$ and an extract of the results of the initial performance test's operating points is provided in Table F.1.

Table F.1: Initial fill performance test results

	$\mathbf{G_w}$ [kg/m^{2}s]	$\mathbf{G_a}$ [kg/m^{2}s]	$\mathbf{Me_{corr}}$	$\mathbf{K_{corr}}$
1	2.610	2.831	1.913	12.937
2	2.598	2.507	1.732	13.569
...	...	...	...	...
24	1.022	1.507	1.369	13.044
25	0.990	1.007	1.007	14.059

Performing a least squares regression to obtain the fill performance characteristic equations for the initial test yields:

$$\hat{Me}_{fi}(0) = 0.528\ L_{fi}\ G_w^{-0.281}\ G_a^{0.878} \tag{F.1}$$

$$\hat{K}_{fd}(0) = 7.481\ L_{fi}\ G_w^{0.288}\ G_a^{-0.373} \tag{F.2}$$

Using these fill performance characteristic equations to calculated the NDWCT water outlet temperature, using the same method and inputs (other than fill performance characteristics) as in Appendix D, yields $T_{wo} = 21.923$ °C.

The fouled condition of the fill (analysed in Appendix C) was performed 21 weeks after the initial test and is designated as time $t = 21$. The fill fouling factors ($f_m(21)$ and $f_k(21)$) are then found by performing least squares regressions of the following equations (in the form of Equations 6.9 and 6.10) to best fit the data in Table C.3:

$$\hat{Me}_{fi}(21) = (1 - f_m(21))\ 0.528\ L_{fi}\ G_w^{-0.281} G_a^{0.878} \tag{F.3}$$

$$\hat{K}_{fd}(21) = (1 + f_k(21))\ 7.481\ L_{fi}\ G_w^{0.288} G_a^{-0.373} \tag{F.4}$$

This regression yields $f_m(21) = -0.0757$ and $f_k(21) = 0.0258$.

The uncertainties of these fouling factors are calculated using Equation 6.11:

$$\begin{aligned} u_{f_m}(21) = \Big[&1.579 \times 10^{-4} + 2.763 \times 10^{-3} + 6.389 \times 10^{-7} \\ &+ 8.207 \times 10^{-6} + 3.619 \times 10^{-5} + 3.560 \times 10^{-6} \\ &+ 7.427 \times 10^{-5} + 1.037 \times 10^{-4} + 3.355 \times 10^{-6} \\ &+ 2.311 \times 10^{-9} + 1.558 \times 10^{-7} + 3.553 \times 10^{-5}\Big]^{0.5} \\ &= 0.0565 \end{aligned}$$

$$\begin{aligned} u_{f_k}(21) = \Big[&2.494 \times 10^{-3} + 3.042 \times 10^{-2} + 2.497 \times 10^{-7} \\ &+ 5.401 \times 10^{-6} - 4.090 \times 10^{-6} + 2.900 \times 10^{-6} \\ &+ 3.203 \times 10^{-5} - 3.575 \times 10^{-4} + 1.151 \times 10^{-6} \\ &+ 1.705 \times 10^{-9} + 2.703 \times 10^{-8} + 1.469 \times 10^{-6}\Big]^{0.5} \\ &= 0.181 \end{aligned}$$

The sensitivity indexes of the NDWCT performance to the fouling factors are calculated numerically using the NDWCT performance prediction calculation:

$$\frac{\partial T_{wo}(21)}{\partial f_m(21)} = -5.277$$

$$\frac{\partial T_{wo}(21)}{\partial f_k(21)} = 1.084$$

The NDWCT water outlet temperature uncertainty is calculated using Equation 6.12:

$$u_{T_{wo}}(21) = \left[(-5.277 \times 0.0565)^2 + (1.084 \times 0.181)^2\right]^{0.5} = 0.356\ ^\circ\text{C}$$

F.2 Sample fill lifecycle cost calculation

The fill lifecycle fuel cost calculation is performed for an estimated fill life of 15 years. The NDWCT inputs are the same as those provided in Appendix D.1.2.

F.2.1 Calculation inputs

F.2.1.1 Atmospheric inputs

The atmospheric inputs to the lifecycle calculation is the dry-bulb temperatures, wet-bulb temperatures and annual durations published for the power plant (see the first columns of Table F.3). Additionally the annual average atmospheric pressure is 84000 Pa and the atmospheric lapse rate is -0.00975 K/m.

F.2.1.2 Power plant inputs

The power plant details are the same as those presented in Appendix D.1.4, with the following additional information. The boiler efficiency is $\eta_{boil} = 0.90$, the fuel (coal) cost is $c_{fuel} = 0.50$ R/kg and the coal calorific value is

$CV = 22000$ kJ/kg.

F.2.1.3 Fill performance inputs

The calculation is performed on an annual basis due to the atmospheric data being presented annually. Representative fouling factors for each year of analysis are presented in Table F.2. These corresponds with the changes in fill performance measured by Whittemore and Massey (1992) for "Pack C" in that study (see Figure 3.7). The fill performance data and mass gain data was combined to find the fill thermal and hydraulic performance changes for each data-point. These performance changes are averaged for each 12-month period in the 50-month long test, resulting in 4 full years of data. The fouling is assumed to stabilise after 4 years, as is indicated by the mass gain behaviour in Figure 3.7.

Table F.2: Fill fouling factors by year

Year	$\mathbf{f_m}$	$\mathbf{f_k}$
1	0.0145	0.00443
2	0.0369	0.0140
3	0.0901	0.0580
4-15	0.195	0.317

F.2.2 Calculation method and results

The calculation is performed by repeating the NDWCT performance prediction calculation, including heat rate correction and both thermal and hydraulic fill fouling factors applied, for each entry in the annual weather calculation and for each calculated fill fouling factor (Table F.2). As an example, the results for Year 4 are presented in Table F.3, with C_h and C_t calculated using Equations 6.14 and 6.15 respectively.

Table F.3: Year 4 annual calculation results

No.	$\mathbf{T_{db}}$	$\mathbf{T_{wb}}$	**Time**	$\mathbf{T_{wi}}$	$\mathbf{T_{wo}}$	$\mathbf{Q_{NDWCT}}$	**HR**	$\mathbf{C_h}$	$\mathbf{C_t}$
	[°C]	**[°C]**	**[hrs]**	**[°C]**	**[°C]**	**[MW]**	**[kJ/kWh]**	**[R]**	**[R]**
1	-8	-8.7	2	27.37	8.43	991.27	8358.11	126638.02	253276.04
2	-6	-6.8	6	28.46	9.57	988.74	8345.97	126454.16	758724.97
3	-4	-4.9	37	29.57	10.71	986.61	8335.74	126299.10	4673066.65
4	-2	-3	87	30.69	11.86	984.91	8327.56	126175.08	10977231.69
5	0	-1.1	163	31.82	13.01	983.66	8321.56	126084.29	20551739.09
6	2	0.6	263	32.89	14.09	982.93	8318.06	126031.23	33146214.03
7	4	2.4	404	34.02	15.22	982.65	8316.73	126011.02	50908451.07
8	6	4.2	545	35.16	16.35	982.88	8317.83	126027.68	68685086.87
9	8	5.8	706	36.24	17.42	983.57	8321.15	126078.10	89011141.04
10	10	7.4	852	37.34	18.49	984.75	8326.78	126163.40	107491214.32
11	12	9.2	983	38.53	19.65	986.55	8335.45	126294.75	124147740.43
12	14	10.6	1111	39.58	20.66	988.59	8345.22	126442.71	140477848.29
13	16	11.9	981	40.61	21.63	990.96	8356.60	126615.15	124209460.48
14	18	13.2	814	41.64	22.61	993.74	8369.95	126817.48	103229428.09
15	20	14.3	660	42.61	23.52	996.66	8383.96	127029.67	83839581.97
16	22	15.1	473	43.45	24.31	999.47	8397.47	127234.38	60181863.48
17	24	15.8	323	44.27	25.07	1002.40	8411.52	127447.21	41165449.87
18	26	16.3	200	45.01	25.76	1005.25	8425.18	127654.30	25530859.42
19	28	16.8	103	45.76	26.45	1008.32	8439.92	127877.50	13171382.59
20	30	17.3	36	46.53	27.16	1011.61	8455.71	128116.85	4612206.64
21	32	17.7	9	47.28	27.84	1014.94	8471.72	128359.38	1155234.39
22	34	18.3	2	48.11	28.60	1018.85	8490.46	128643.28	257286.57

The total fuel cost for each year is calculated by summing its period costs and is provided in Table F.4. The annual fuel cost of the unfouled condition (calculated using Equation 6.16) is provided, along with a column containing the annual fuel cost increase caused by fouling. All costs are in Rand.

Table F.4: Annual fuel cost results

Year	**Fuel cost [R/year]**	**Fouling cost [R/year]**
Unfouled	1 106 715 521.28	
1	1 106 786 667.37	71 146.09
2	1 106 906 495.50	190 974.22
3	1 107 255 090.15	539 568.87
4-15	1 108 434 488.00	1 718 966.72

The total lifecycle fuel cost, calculated as the sum of the fuel cost of the 15 year life of the fill is calculated as R16 622 162 109.06. This is R21 429 289.84, or approximately 0.13% greater than total lifecycle cost for the unfouled case of total of R16 600 732 819.22.

List of References

ASHRAE (2001). 2001 ASHRAE handbook: Fundamentals. American society of heating, refrigerating and air-conditioning engineers, Atlanta, Georgia.

ASME (2014). Performance test code 19.1: Test uncertainty. American society of mechanical engineers. New York.

Augustyn, O. (2017). Cooling water system health care guideline. Tech. Rep. 240-56030508, Eskom Holdings SOC Ltd.

Augustyn, O. (2018). Cooling tower fill replacement strategy report. Tech. Rep. 474-11061, Eskom Holdings SOC Ltd.

Augustyn, O. (2019). Position paper on cooling towers performance and vacuum related load losses. Tech. Rep. 474-11899, Eskom Holdings SOC Ltd.

Augustyn, O., Preez, F.D., Kohrs, C., Plessis, J.D. and Roux, D. (2018). Experimental investigation of the thermal performance of cooling tower fills - results. In: PowerGen Africa 2018.

Aull, R. (2013). Cooling tower fills to optimize CT performance. Presentation. NTPC IPS 2013 O&M Conference.

Bertrand, T.P. (2011). Evaluation of a 1.5×1.5 m^2 counter-flow fill performance test facility with a view to contributing to a fill performance standard. Master's thesis, Mechanical and Mechatronic Engineering, Stellenbosch University, Stellenbosch, South Africa.

Bosman, P.B. (1985). Review and feedback of experience gained over the last fifty years in design and construction of natural-draught cooling towers. Engineering structures, vol. 7, no. 4, pp. 268–272. ISSN 0141-0296.

Bott, T.R. (1995). Fouling of heat exchangers. Elsevier, Amsterdam. ISBN 0-444-82186-4.

Burden, R.L. and Faires, J.D. (2011). Numerical analysis. 9th edn. Brooks/Cole, Boston. ISBN 0-538-73351-9.

Cale, S. (1982). Development of evaporative cooling packing. Tech. Rep. EUR 7709 EN, Commission of European communities, Luxembourg.

Cengel, Y.A. (2006). Heat and mass transfer: A practical approach. 3rd edn. McGraw-Hill, New York. ISBN 007-125739-X.

Cengel, Y.A. and Boles, M.A. (2006). Thermodynamics: An engineering approach. 5th edn. McGraw-Hill, New York.

Characklis, W.G. and Marshall, K.C. (eds.) (1990). Biofilms. John Wiley & Sons,

Hoboken, New Jersey. ISBN 0471826634.

Cleaver, J.W. and Yates, B. (1973). Mechanism of detachment of colloidal particles from a flat substrate in a turbulent flow. Journal of colloid and interface science, vol. 44, no. 3, pp. 464–474. ISSN 00219797.

Coleman, H.W. and Steele, W.G. (2018). Experimentation, validation, and uncertainty analysis for engineers. 4th edn. John Wiley & Sons, Hoboken, New Jersey. ISBN 9781119417668.

Dahm, M., McLaughlin, M. and Woicke, N. (2015). Modular splash fills. Cooling technology institute technical paper TP15-03.

De Villiers, E. and Kröger, D.G. (2001). Inlet losses in counterflow wet-cooling towers. Journal of engineering for gas turbines and power, vol. 123, no. 2, pp. 460–464. ISSN 0742-4795.

Department Of water affairs and forestry (1996). South African water quality guidelines - Volume 1: Domestic use. 2nd edn. Pretoria. ISBN 0-7988-5339-5.

DiFilippo, M. and Maulbetsch, J. (2003). Use of degraded water sources as cooling water in power plants. Tech. Rep. 1005359, California energy commission and the Electric power research institute.

Du Preez, A. and Kröger, D. (1994). The influence of a buoyant plume on the performance of a natural draft cooling tower. In: 9th International association for hydraulics research cooling tower and spraying pond symposium. Brussels, Belgium.

Du Preez, F. (2018). Tutuka cooling tower fill replacement position paper. Tech. Rep. 474-11888, Eskom Holdings SOC Ltd.

Endress + Hauser (2019a). Technical information: Cerabar M PMC51, PMP51, PMP55. TI00436P/00/EN/28.19.

Endress + Hauser (2019b). Technical information: Deltabar S PMD75, FMD77, FMD78. TI00382P/00/EN/30.19.

Endress + Hauser (undated a). Technical information: Proline Promag 10D. TI00081D/06/EN/14.16.

Endress + Hauser (undated b). Technical information: TLSR1 RTD measuring sensor. TI00158R/09/EN/03.14.

Geldenhuys, J. and Kröger, D. (1986). Aerodynamic inlet losses in natural draft cooling towers. In: Proceedings of 5th IAHR cooling tower workshop. Monterey.

Gentle, J.E. (2009). Statistics and computing. Springer, New York. ISBN 978-0-387-98144-4.

Gill, J., Donlan, R. and Gibbon, D. (1994). Fouling of film forming cooling tower fills - a mechanistic approach. CTI journal, vol. 16, no. 1, pp. 10–19. ISSN 0273-3250.

Gilliland, E.R. (1934). Diffusion coefficients in gaseous systems. Industrial and engineering chemistry, vol. 26, no. 6, pp. 681–685. ISSN 0019-7866.

Govender, R. (2017). Chemistry standard for auxiliary cooling water. Tech. Rep. 240-106192541, Eskom Holdings SOC Ltd.

Jestin, L., Van Coller, J. and Gwebu, E. (2017). Overview of the power industry. Eskom power plant engineering institute course reader.

Kloppers, J.C. (2003). A critical evaluation and refinement of the performance prediction of wet-cooling towers. Ph.D. thesis, Mechanical and Mechatronic Engineering, Stellenbosch University, Stellenbosch, South Africa.

Kloppers, J.C. and Kröger, D.G. (2004). Cooling tower performance: A critical evaluation of the Merkel assumptions. R & D Journal, vol. 20, no. 1, pp. 24–29. ISSN 2309-8988.

Kotze, J. (2019). A fouling and thermal performance test rig for cooling tower fill selection. Cooling technology institute technical paper TP19-05.

Kroese, D.P., Brereton, T., Taimre, T. and Botev, Z.I. (2014). Why the Monte Carlo method is so important today. Wiley interdisciplinary reviews: Computational statistics, vol. 6, pp. 386–392. ISSN 1939-0068.

Kroese, D.P., Taimre, T. and Botev, Z.I. (2011). Handbook of Monte Carlo methods. John Wiley & Sons, Hoboken, New Jersey. ISBN 978-0-470-17793-8.

Kröger, D. (2004). Air-cooled heat exchangers and cooling towers. PennWell, Tulsa. ISBN 0-87814-896-5 (Vol. 1), 1-59370-019-9 (Vol. 2).

Lowe, H.J. and Christie, D.G. (1961). Heat transfer and pressure drop data on cooling tower packings and model studies of the resistance of natural draft towers to airflow. In: Proceedings of the international heat transfer conference, Part V. Colorado.

McCloskey, T., Dooley, R. and McNaughton, W. (2011). Report TR-108943, Turbine steam path damage: theory and practice, Volume 2. Tech. Rep. TR-108943, Electric power research institute, Palo Alto.

Merkel, F. (1926). Verdunstungskühling. VDI-Zeitschrift, vol. 70, no. 4, pp. 123–127.

Michaels, A.J. (2015). Investigation of the effect of a new splash grid on natural draught wet cooling tower (NDWCT) performance. Master's thesis, Mechanical and Mechatronic Engineering, Stellenbosch University, Stellenbosch, South Africa.

Mirsky, G. and Monjoie, M. (1991). Film fill recent research and application data. CTI journal, vol. 12, no. 1, pp. 31–46. ISSN 0273-3250.

Monjoie, M. (2009). Cooling tower fill technology for fouling-scaling resistance. Presentation. 14th IAHR cooling tower and heat exchanger conference, Stellenbosch, South Africa.

Monjoie, M., Noble, R. and Mirsky, G.R. (1993). Research of fouling film fill. Cooling technology institute technical paper TP93-06.

Mortensen, K. and Michell, F. (2013). Film fill fouling: Updated methods, results and predictions. CTI journal, vol. 34, no. 1, pp. 18–31. ISSN 0273-3250.

Mortensen, K.P. and Conley, S.N. (1994). Film fill fouling in counterflow cooling towers: Research results. Cooling technology institute technical paper TP94-05.

PR Electronics (undated). Product manual: 3000 series: 6 mm series of temperature converters. 3000V103-UK.

Puckorius, P.R. (2013). Selecting the optimal cooling tower fill. Chemical engineering progress, vol. 109, no. 8, pp. 31–34. ISSN 0360-7275.

Republic of South Africa. Department of environmental affairs and tourism (2008). Environmental conservation act, 1989: Regulations for the prohibition of the use,

manufacturing, import and export of asbestos and asbestos containing materials. Government gazette no. 30904.

Ruszkowski, M. (2016). Cooling tower equipment guidelines. Tech. Rep. 30020008693, Electric power research institute, Palo Alto.

Siemens AG (2012). Simatic S7-1200 Programmable controller system manual. A5E02486680-06.

Siemens AG (2015). Simatic ET 200SP distributed I/O system system manual. A5E03576849-AF.

Terblanche, R. (2008). Investigation of performance enhancing devices for the rain zones of wet-cooling towers. Master's thesis, Mechanical and Mechatronic Engineering, Stellenbosch University, Stellenbosch, South Africa.

Terblanche, R. (2011). Evaluation of drop break-up after impingement on horizontal slat grids and the effect of drop size of cooling tower rain zone performance. Ph.D. thesis, Mechanical and Mechatronic Engineering, Stellenbosch University, Stellenbosch, South Africa.

Troncin, H. (2012). Fill testing in cooling tower in case of fouling issues. CTI journal, vol. 33, no. 2, pp. 62–66. ISSN 0273-3250.

Van der Merwe, D. (2007). Evaluation of natural draught wet-cooling tower performance uncertainties. Master's thesis, Mechanical and Mechatronic Engineering, Stellenbosch University, Stellenbosch, South Africa.

White, F. (2005). Fluid mechanics. 5th edn. McGraw-Hill, New York. ISBN 007-124343-7.

Whittemore, M.R. and Massey, T. (1992). Current Fouling Problems of PVC Film Fills and Research into New Designs to Eliminate Fouling. In: Proceedings of the American Power Conference, vol. 54. Chicago. ISSN 0097-2126.

Zaorski, A. and Miller, W.C. (2017). A study on bio-fouling characteristics of contemporary trickle and modular splash fills. CTI journal, vol. 38, no. 1, pp. 60–67. ISSN 0273-3250.